



**MATEMATICKO-FYZIKÁLNÍ  
FAKULTA**  
Univerzita Karlova

## **MASTER THESIS**

Bc. Monika Spasovová

### **Vibrational spectroscopy of pharmacologically important molecules: Study of L-DOPA and its deuterated derivatives**

Institute of Physics of Charles University

Supervisor of the master thesis: RNDr. Václav Profant, Ph.D.

Study programme: Physics

Study branch: Biophysics and chemical physics

Prague 2020

I wish to express my deepest gratitude to my supervisor RNDr. Václav Profant, Ph. D., without whose guidance and support this thesis would not be created.

My sincere thanks goes also to RNDr. Vladimír Kopecký Jr., Ph.D. for the help with the IR and VCD measurement, RNDr. Josef Kapitán, Ph.D. for the help with the measurement of Raman and ROA, RNDr. Eva Kočíšová, Ph.D. for the help with the DCDR measurement, and Mgr. Jakub Klener for performing the MD simulations.

I also wish to thank the UNCE/SCI/-010 (Centre for nano- and biophotonics for the financial support for the purchase of the samples), and Metacentrum VO for providing the computational power for the quantum mechanical simulations.

I am also extremely grateful to my family for the unconditional love and support.

I declare that I carried out this master thesis independently, and only with the cited sources, literature and other professional sources.

I understand that my work relates to the rights and obligations under the Act No. 121/2000 Sb., the Copyright Act, as amended, in particular the fact that the Charles University has the right to conclude a license agreement on the use of this work as a school work pursuant to Section 60 subsection 1 of the Copyright Act.

In ..... date.....

signature of the author

Title: Vibrational spectroscopy of pharmacologically important molecules: Study of L-DOPA and its deuterated derivatives

Author: Bc. Monika Spasovová

Department: Institute of Physics of Charles University in Prague

Supervisor: RNDr. Václav Profant, Ph.D.

Abstract: L-3,4-dihydroxyphenylalanine (L-DOPA, levodopa) is a gold standard treatment of Parkinson's disease. Lately, it has been found that some of its deuterated analogues exhibit higher potency in the treatment; thus, they could replace L-DOPA. The subject of this thesis was a study of L-DOPA and its deuterated derivatives by the means of vibrational spectroscopy (Raman, ROA, IR, and VCD) and a comparison of the experimental results to a quantum mechanical simulations of the spectra. ROA and VCD are chiroptical methods, thus they are suitable for measurement of chiral molecules amongst which L-DOPA indeed belongs. Thanks to the quantum chemistry calculations, which yielded spectra with a very good agreement with the experiment, we were able to assign experimental spectral features to individual vibrational modes of the L-DOPA. The use of chiroptical techniques (mainly ROA) enabled an assignment of an absolute configuration of double deuterated derivative of L-DOPA,  $\alpha,\beta$ -D<sub>2</sub>-L-DOPA. It revealed that it occurs in a (*S*- $\alpha$ ,*S*- $\beta$ )-enantiomeric form.

Keywords: Parkinson's disease, L-DOPA, vibrational spectroscopy, DFT spectral simulations, ROA, chirality



# Table of Contents

<b>PREFACE</b> .....	<b>3</b>
<b>AIMS OF THE THESIS</b> .....	<b>4</b>
<b>1 LEVODOPA</b> .....	<b>5</b>
1.1 PARKINSON'S DISEASE.....	5
1.2 PHARMACOKINETICS OF LEVODOPA.....	7
1.3 DEUTERATED FORMS OF L-DOPA IN PD TREATMENT.....	10
1.3.1 Stereospecificity of L-DOPA metabolism.....	11
1.3.2 Studies in rodent model of PD disease.....	12
1.3.3 Studies in healthy subjects.....	13
1.4 SOLUBILITY.....	13
1.5 L-DOPA AS A MODEL SYSTEM.....	16
<b>2 FUNDAMENTALS OF VIBRATIONAL SPECTROSCOPY</b> .....	<b>18</b>
2.1 BORN-OPPENHEIMER APPROXIMATION.....	18
2.2 VIBRATIONS OF DIATOMIC MOLECULES.....	20
2.2.1. Harmonic approximation.....	20
2.2.2. Vibrational selection rules.....	20
2.2.3. Selection Rules for Raman transition.....	21
2.2.4. Polyatomic molecules.....	22
<b>3 METHODS OF VIBRATIONAL SPECTROSCOPY</b> .....	<b>24</b>
3.1 INFRARED ABSORPTION SPECTROSCOPY (IR).....	25
3.1.1. Process of absorption.....	25
3.1.2. IR spectrometers.....	25
3.2 RAMAN SPECTROSCOPY.....	27
3.2.1 Raman effect.....	27
3.2.2 Raman spectrometer.....	29
3.3 VIBRATIONAL OPTICAL ACTIVITY (VOA).....	30
3.3.1 Chirality.....	30
3.3.2 Vibrational circular dichroism (VCD).....	32
3.3.3 Raman optical activity (ROA).....	33
3.4 COMPARISON OF IR AND RAMAN SPECTROSCOPY.....	35
<b>4 QUANTUM MECHANICAL SIMULATIONS</b> .....	<b>36</b>
4.1 AB-INITIO METHODS.....	36
4.1.1 Hartree-Fock theory (HF).....	36
4.1.2 Density functional theory (DFT).....	37
4.1.3 Basis sets.....	38
4.2 SPECTRAL SIMULATIONS.....	38
4.2.1 Geometry optimization.....	38
4.2.2 Vibrational frequencies and intensities.....	39
4.2.3 Solvent models.....	40
<b>5 EXPERIMENTAL DETAILS</b> .....	<b>42</b>
5.1 SAMPLES.....	42
5.2 ABSORPTION METHODS.....	43
5.2.1 ChiralIR-2X™.....	43
5.2.1 Beta Cell.....	44
5.2.2 ChiralIR-2X™ measurement and data treatment.....	44
5.3 SCATTERING METHODS.....	45
5.3.1 Spectrometer SPEX.....	46
5.3.2 Measurement using SPEX and data treatment.....	46
5.3.3 Raman confocal microscope Alpha300 RSA.....	48

5.3.4	Sample preparation and measurement using Alpha300 RSA .....	50
5.3.5	ROA spectrometer .....	52
5.3.6	Sample preparation and measurement using ROA spectrometer .....	52
5.4	PARAMETERS OF SPECTRAL SIMULATION .....	53
<b>6</b>	<b>RESULTS AND DISCUSSION .....</b>	<b>54</b>
6.1	SOLUBILITY.....	54
6.1.1	Solubility based on pH.....	54
6.1.2	Solubility in various solvents .....	56
6.2	RAMAN SPECTRA OF DIFFERENT PHASES .....	59
6.3	COMPARISON OF DIFFERENT NON-DEUTERATED DOPA SAMPLES .....	64
6.4	COMPARISON OF RAMAN AND IR SPECTRA OF DIFFERENTLY DEUTERATED SAMPLES.....	66
6.5	VOA SPECTRA OF L-DOPA.....	69
6.5.1	VCD spectra of DOPA .....	71
6.6	AB INITIO CALCULATIONS OF L-DOPA.....	74
6.6.1	Conformational analysis.....	74
6.6.2	Spectral markers of different L-DOPA conformations.....	79
6.6.3	Vibrational assignment of L-DOPA spectra.....	92
6.7	VOA OF DEUTERATED L-DOPA ANALOGUES .....	97
6.7.1	Triple deuterated 2',5',6'-D3-L-DOPA (VI).....	97
6.7.2	Triple deuterated biologically active $\alpha,\beta,\beta$ -D3-L-DOPA (V) .....	98
6.7.3	Double deuterated biologically active $\alpha,\beta$ -D2-L-DOPA (IV).....	100
	<b>CONCLUSIONS.....</b>	<b>105</b>
	<b>REFERENCES.....</b>	<b>108</b>
	<b>LIST OF FIGURES.....</b>	<b>115</b>
	<b>LIST OF TABLES.....</b>	<b>119</b>
	<b>LIST OF ABBREVIATIONS.....</b>	<b>120</b>
	<b>ATTACHMENTS.....</b>	<b>121</b>
A.1.	IR SPECTRA OF L-DOPA DEUTERATED ANALOGUES IN A LIQUID STATE .....	121
A.2.	IR SPECTRA OF L-DOPA DEUTERATED ANALOGUES IN A SOLID STATE .....	122

## Preface

Levodopa is an  $\alpha$ -amino acid which serves in the human organism as a direct precursor to a neurotransmitter dopamine and it is used as a treatment for the second most common neurodegenerative disease caused by age, the Parkinson's disease. However, the inevitable need for gradual increase of L-DOPA dosage entails a deterioration in the side effects of the treatment. Hence, it is desirable to find ways of decreasing the necessary dosage while preserving the effect of the treatment. Until recently, this had been done mainly by concomitant treatment with inhibitors of enzymatic activity which is responsible for the undesirable extensive metabolism of L-DOPA. Relatively recently discovered option is the use of specifically deuterated derivatives of L-DOPA which, thanks to their less extensive undesirable metabolism, provide increased dopamine output in comparison with non-deuterated L-DOPA.

The specificity of L-DOPA deuteration plays a crucial role in the treatment improvement and so does the enantiomeric purity of the drug. Levodopa is a chiral molecule which means that it is not identical to its mirror image. Only its L-enantiomer is biologically active, which is the case for all amino acids taking part in biological processes. Different enantiomers of chiral molecules have different optical properties which makes them suitable objects of study using vibrational optical activity techniques (including vibrational circular dichroism and Raman optical activity). Moreover, general vibrational spectroscopy (VS) techniques also provide a good characterisation of differently deuterated forms of a molecule. The main objective of this thesis is vibrational analysis of L-DOPA and three of its differently deuterated derivatives. Two of them have shown an increased potency in dopamine production, thus, they have the potency to replace L-DOPA and become a new gold standard for the Parkinson's treatment.

The thesis is divided into 7 chapters. The first one describes the metabolism and the role of L-DOPA in the treatment of Parkinson's. The second and third chapters give the bases of the theory and methods of VS, respectively. The fourth chapter outlines the basics of quantum mechanical simulations. In the fifth chapter the description of experimental techniques is given. The sixth chapter presents the results of the experiments and simulations along with their discussion and finally, the last chapter sums up the results, evaluates meeting the objectives and shows a perspective for further research.

## Aims of the thesis

Main goal of this thesis is to perform an overall characterization of L-DOPA molecule by different vibrational and chiroptical spectroscopy methods and to specify the experimental method suitable for differentiation of differently deuterated L-DOPA analogues. The individual aims of this thesis can be summarized in as follows:

1. Elaboration of a review of current employment of L-DOPA in Parkinson's disease treatment.
2. Familiarization with different methods of vibrational and chiroptical spectroscopy and mastering measurements on Raman spectrometer and micro-spectrometer, and VCD spectrometer.
3. Obtaining IR, Raman, and VCD spectra of solid L-DOPA and its deuterated analogues
4. Finding suitable measurement conditions enabling liquid phase measurement of Raman and ROA spectra of L-DOPA, characterization of differences between L-DOPA samples at different pH
5. Obtaining high quality Raman, ROA, IR, and VCD spectra of L-DOPA and its deuterated derivatives and addressing spectral changes connected with each specific deuteration
6. Performing simulations of vibrational spectra of L-DOPA and its deuterated derivatives with respect to the dynamical aspects of their geometry in solution, evaluation of the contribution of the different conformers to final simulated spectra
7. Carrying out a vibrational analysis of experimental spectral features based on simulated spectral profiles, identification of characteristic spectral features linked with the different deuterations
8. Comparison of experimental and simulated spectra and evaluating whether it is possible to distinguish between different epimers of  $\alpha,\beta$ -D<sub>2</sub>-L-DOPA based on VOA

# 1 Levodopa

L-DOPA, also known as levodopa or L-3,4-dihydroxyphenylalanine is a small amino acid which occurs naturally in various animal and plant species including humans. In human body it serves as a precursor to a class of neurotransmitters called catecholamines: dopamine, noradrenaline, and adrenaline. More precisely, it is a direct precursor to dopamine from which noradrenaline and adrenaline, respectively, are derived. Neurons which synthesize dopamine are affected in patients with Parkinson's disease (PD) leading to a dopamine deficiency which is responsible for the symptoms of the disease. Blood-brain barrier (BBB) (a selective semipermeable border between blood vessels and extracellular fluid of the central nervous system that prevents non-selective crossing of solutes in blood into the brain) is impervious for dopamine molecule but it is permeable for a direct precursor of dopamine — levodopa. Thus, levodopa is used to increase dopamine levels in the brain as a treatment of PD.

Dopamine is synthesized either indirectly from phenylalanine or directly from tyrosine, both of which are received from the food. The mechanism of synthesis is shown in the Figure 1.1. L-Phenylalanine is converted into L-tyrosine by the enzyme phenylalanine hydroxylase, further L-tyrosine is converted by the enzyme tyrosine hydroxylase into L-DOPA, and finally L-DOPA is converted into dopamine by DOPA decarboxylase. For the cofactors participating in these reactions see e.g. (Musacchio, 1975).

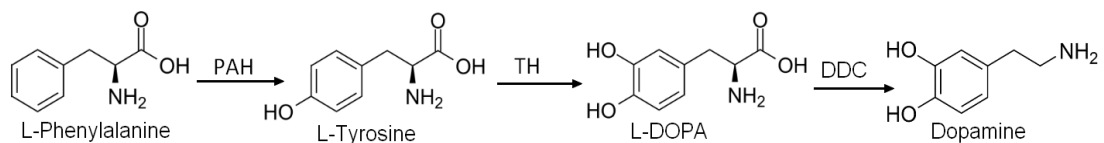


Figure 1.1: Mechanism of the dopamine synthesis. (PAH, phenylalanine hydroxylase; TH, tyrosine hydroxylase; DDC, DOPA decarboxylase)

## 1.1 Parkinson's disease

Parkinson's disease (PD) is the second most common progressively disabling neurodegenerative disorder that affects 2-3% of the population over 65 years of age (Poewe et al., 2017). It manifests by movement disorders: bradykinesia, tremor, rigidity, flexed posture, postural instability, and freezing of gait; but also by non-motor symptoms as mood changes, anxiety, cognitive changes and sensory problems. It was

described by James Parkinson in the 19<sup>th</sup> century. (Marsden et al.,1976; Fahn et al., 2004). The time progression of the clinical symptoms of PD is shown in the Figure 1.2.

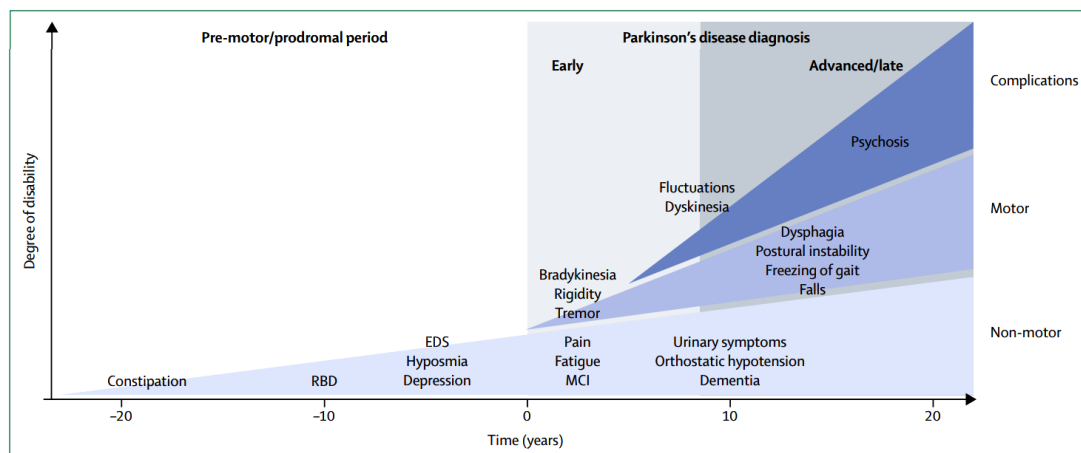


Figure 1.2: Clinical symptoms and time course of Parkinson's disease progression. Adopted from (Kalia and Lang, 2015).

The cause of PD is unknown, but it seems to result from a combination of genetic and environmental factors affecting numerous fundamental cellular processes. (Kalia and Lang, 2015) It causes a degeneration of dopaminergic neurons in one of the basal ganglia in midbrain called substantia nigra. These neurons normally produce dopamine and transfer it to another basal ganglion, striatum. The dopamine deficiency in striatal neurons leads to the motor and non-motor symptoms. Treatment of PD is thus mainly based on substituting dopamine loss. This is achieved for more than 50 years with levodopa, which is up to these days widely recognized as the most effective PD therapy. (Hornykiewicz, 2010; LeWitt and Fahn, 2016)

Nevertheless, treatment with levodopa is accompanied by numerous side effects, including nausea, vomiting, and levodopa-induced dyskinesia (LID) which particularly deteriorates as the treatment proceeds. After several years of levodopa treatment patients start to develop motor response fluctuations called the “wearing off” phenomenon. That means that the symptoms of PD worsen before the next dose of medication is due. The condition when the medication is working and no or little symptoms are perceptible is referred to as an “on-state” and the state when the symptoms are returning is called “off-state”. Many patients experience on and off fluctuations several times a day. While wearing off symptoms are associated with the lowest plasma levels of L-DOPA and disappear when the next dose is administered, LID occurs at the peak plasma level of L-DOPA and alleviates with the dose reduction.

(Rajput et al., 2004) The biological cause of both is unknown; however, research suggests that wearing off and dyskinesia are caused by different pathophysiological mechanisms. (Rascol et al., 2000; Rajput et al., 2002, 2004; Watanabe et al. 2003) None of these side effects were observed in patients who were erroneously diagnosed with PD and received levodopa treatment for many years. (Rajput et al., 2015)

Current strategies of minimalizing the side effects of PD treatment are: (i) prolonging the peripheral plasma half-life of the drug, (ii) increasing bioavailability of synthesised dopamine, and (iii) achieving more continuous dopaminergic stimulation. First two are provided by concomitant treatment with inhibitors of undesirable metabolic pathways of levodopa and nigral dopamine and the third one by adjusting the frequency and dose of the administration of drugs.

Diagnosis of Parkinson's disease occurs with the onset of motor symptoms (time 0 years, see Figure 1.2) but can be preceded by a premotor or prodromal phase of 20 years or more. This prodromal phase is characterised by specific non-motor symptoms. Additional non-motor features develop following diagnosis and with disease progression, causing clinically significant disability. Axial motor symptoms, such as postural instability with frequent falls and freezing of gait, tend to occur in advanced disease.

Long-term complications of dopaminergic therapy, including fluctuations, dyskinesia, and psychosis, also contribute to the disabilities. The most common of them are the excessive daytime sleepiness, the mild cognitive impairment, and the REM sleep behaviour disorder. (Kalia and Lang, 2015)

## 1.2 Pharmacokinetics of levodopa

L-DOPA is administered to the patient orally and it has to travel a complicated path to its site of action in the brain. Due to an extensive first-pass metabolism about 30-50% of L-DOPA reaches the bloodstream circulation and only 1% of the dose actually enters the brain. The plasma half-life of the drug is about 1 hour. (Andersson et al. 1975; Hauser, 2009; Waller and Sampson, 2003) Metabolism of levodopa is shown in Figure 1.3.

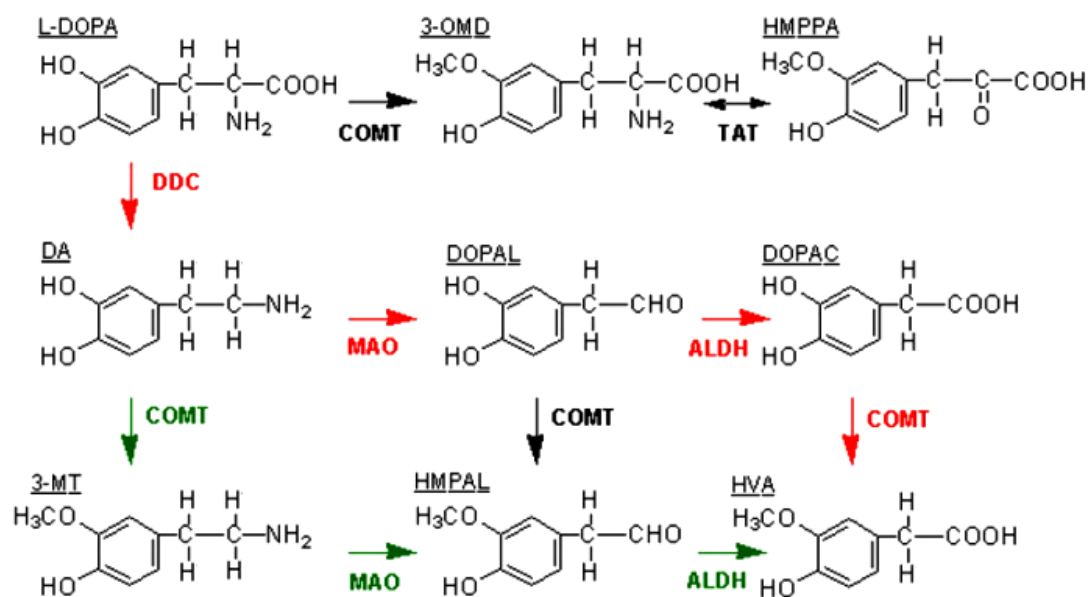


Figure 1.3: Metabolism of L-DOPA. Abbreviations include: 3-OMD, 3-*O*-methyldopa; ALDH, aldehyde dehydrogenase; COMT, catechol *O*-methyltransferase; DA, dopamine; DDC, DOPA decarboxylase; DOPAL, 3,4-dihydroxyphenylacetaldehyde; DOPAC, 3,4-dihydroxyphenylacetic acid; HMPPA, 4-hydroxy-3-methoxyphenylpyruvic acid; HMPAL, 4-hydroxy-3-methoxyphenyl acetaldehyde; HVA, homovanillic acid; L-DOPA, L-3,4-dihydroxyphenylalanine; MAO, monoamine oxidase; TAT, tyrosine aminotransferase. Adopted from (Schneider et al. 2018) and edited.

Decarboxylation by ubiquitous DOPA decarboxylase (DDC) in gut, liver, and kidney outbalances the other pathways; 69% of L-DOPA urinary recovered metabolites appear as dopamine and its metabolites. (Nutt and Fellman, 1984) Administration of DDC inhibitor carbidopa prolongs half-life of levodopa almost 2-fold. Carbidopa does not cross the BBB; hence, it does not inhibit dopamine synthesis in the dopaminergic neurons of substantia nigra. (Deleu et al., 2002).

Second most probable pathway is methoxylation by catechol-*O*-methyltransferase (COMT). However, if carbidopa co-treatment is introduced, it becomes the primary pathway, producing metabolite 3-*O*-methyldopa (3-OMD) which is a competitive inhibitor of active transport of levodopa across the BBB. (Männistö and Kaakkola, 1989) It also competes with levodopa in the synthesis, transport and uptake of dopamine in the brain. (Lee et al., 2007) Administration of COMT inhibitors entacapone or tolcapone simultaneously with levodopa/carbidopa treatment decreases average levodopa daily dose, alleviates the wearing-off symptoms and increases the duration of the on-state. (Baas et al., 1997) BBB is permeable for tolcapone which allows it to act as COMT inhibitor also in the brain, leading to a higher efficiency than



entacapone. On the other hand, treatment with tolcapone carries the risk of hepatic injury and requires careful monitoring. (Factor et al., 2001; Deleu et al. 2002)

Once dopamine is synthesised in the presynaptic neuron of substantia nigra, it is released in the synaptic cleft where it becomes target for methylation by COMT to 3-methoxytyramine (3-MT) and transamination to 3,4-dihydroxyphenylacetaldehyd (DOPAL) by monoamine oxidase (MAO) followed by oxidation to 3,4-dihydroxyphenylacetic acid (DOPAC) by aldehyde dehydrogenase. The former is regulated by COMT inhibitor tolcapone and the latter can be prevented by administration of MAO-B inhibitor; e.g., selegiline which in addition to being MAO-B inhibitor reduces presynaptic dopamine reuptake in the brain. (Chrisp et al., 1991; Gerlach et al., 1996) It postpones the time when levodopa treatment is necessary for newly diagnosed patients and once levodopa is introduced MAO-B inhibitor enhances its bioavailability which again reduces the wearing-off symptoms. (Ives et al., 2004) Common final metabolite of these pathways is homovanillic acid (HVA).

The uptake of dopamine by postsynaptic striatal neurons can be potentiated by dopamine agonists. There are several of them being used for adjunct therapy or as an initial monotherapy for PD. (Fox et al., 2011; Connolly and Lang, 2014) Thanks to their long half-life they provide less pulsatile stimulation of striatal dopamine receptors; thus, reduce the motor symptoms of PD.

Figure 1.4 shows the summary of possible L-DOPA metabolic pathways and their eventual inhibition in the treatment of PD.

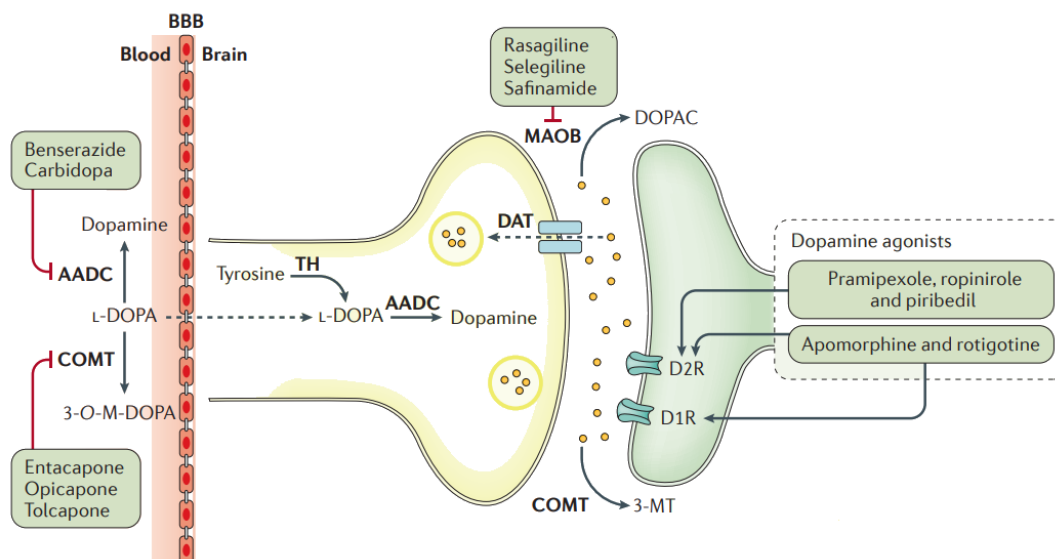


Figure 1.4: Dopaminergic drug pathways in PD. Presynaptic targets include L-DOPA substitution combined with peripherally active inhibitors of aromatic amino acid decarboxylase (AADC) or catechol-*O*-methyltransferase (COMT). Monoamine oxidase type B (MAO-B) inhibitors enhance the synaptic availability of dopamine (both endogenous and exogenous), whereas dopamine agonists act postsynaptically. Dashed arrow from blood to brain designates blood–brain barrier (BBB) transport of L-DOPA. Dashed arrow through the dopamine transporter (DAT) denotes reuptake of dopamine from the synaptic cleft. 3-*O*-M-DOPA, 3-*O*-methyl-dopa; 3-MT, 3-methoxytyramine; D1R, dopamine D1 receptor; DOPAC, 3,4-dioxy-phenylacetic acid; TH, tyrosine hydroxylase. Adopted from (Poewe et al., 2017).

### 1.3 Deuterated forms of L-DOPA in PD treatment

As already mentioned before, levodopa is used as the gold standard in PD treatment. However, as the disease progresses, number of degenerated dopaminergic neurons increases, and levodopa dosage increase is required. That elicits side effects such as wearing-off symptoms and levodopa induced dyskinesia (LID). Thanks to a concomitant treatment with inhibitors of L-DOPA metabolism and dopamine agonists, which increase the bioavailability of L-DOPA and dopamine, respectively, lower doses of levodopa are necessary. Thanks to that the emergence of the side effects is postponed and their symptoms are attenuated. However, these co-treatments have their own side effects and complications. Thus, developing other ways of enhancing the efficiency of L-DOPA is desirable.

Studies mentioned below have proved that triple-deuterated  $\alpha,\beta,\beta$ -D3-L-DOPA (once at the  $\alpha$  and twice at the  $\beta$ -carbon, Figure 1.5) exhibits higher potency in dopamine synthesis and a longer dopamine half-life. As a result, lower doses of D3-L-DOPA compared to non-deuterated L-DOPA are sufficient to achieve the same

efficiency. Thus,  $\alpha,\beta,\beta$ -D3-L-DOPA may be the first drug to appear superior to L-DOPA in the treatment of PD. (Alken, 2016)

### 1.3.1 Stereospecificity of L-DOPA metabolism

Stereospecificity is a property of chemical reaction which yields different stereoisomers from different stereoisomeric reactants.

Kinetic isotope effect (KIE) is a change in the rate of a chemical reaction caused by a substitution of one of the reactant's atoms by its isotope. Primary KIE occurs when the bond to the isotopically labelled atom is being broken or formed whereas secondary KIE occurs when the isomerization is remote from the bond that is being broken or formed. Naturally, secondary KIE is lower than primary KIE. Hydrogen atom substitution by deuterium is expected to lower the reaction rate. However, in some reactions deuterated species react faster than non-deuterated, exhibiting so called inverse KIE.

In previous research (Yu et al., 1986, 1988) the stereospecificity of dopamine deamination by MOA and its kinetic deuterium isotope effect was studied *in vitro*. Firstly, it was observed that decarboxylation of  $\alpha$ -D1-L-DOPA in H<sub>2</sub>O by DDC from hog kidney is stereospecific. It only produces *S*-enantiomer of  $\alpha$ -D-Dopamine. To obtain *R*-[ $\alpha$ -D]-Dopamine, non-deuterated L-DOPA has to be decarboxylated in D<sub>2</sub>O. (Figure 1.5)

Secondly, they have shown that MAO-A and MAO-B (from different sources including rat liver, human platelet, and placenta) catalyse the stereochemical removal of *R*-hydrogen/deuterium, whereas *S*-hydrogen/deuterium is maintained at DOPAL. (Figure 1.5) This was confirmed when only small reduction in the dehydrogenation of *S*-[ $\alpha$ -D]-Dopamine in comparison to non-deuterated dopamine occurred, thanks to the secondary KIE, whereas the rate of oxidation of *R*-[ $\alpha$ -D]-Dopamine was much slower thanks to the primary KIE of substituted deuterium.

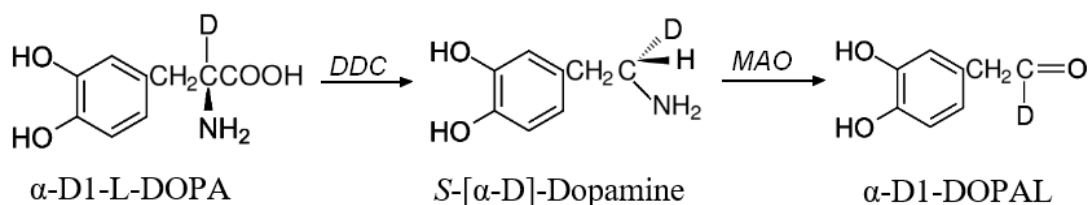


Figure 1.5: Metabolism of  $\alpha$ -D1-L-DOPA; DOPA decarboxylase (DDC) catalyses the decarboxylation to *S*- [D1]-L-DOPA, which is further oxidized by monoamine oxidase to  $\alpha$ -D1-DOPAL proving that MAO removes the hydrogen in *R*-position.

### 1.3.2 Studies in rodent model of PD disease

Research group led by professor Torgny Svensson and associate professor Björn Schilström at Karolinska Institutet in Stockholm used a rodent model of PD to study *in vivo* the effects of four differently deuterated derivatives of L-DOPA on dopamine production:  $\alpha$ -D1-L-DOPA,  $\beta,\beta$ -D2-L-DOPA,  $\alpha,\beta$ -D2-L-DOPA and  $\alpha,\beta,\beta$ -D3-L-DOPA (Figure 1.6; Malmjöf et al., 2008). Two indicators were measured to determine the effect of different compounds: dopamine levels and dopamine metabolite DOPAC levels. Their ratio was calculated to determine the dopamine turnover.

$\alpha$ -D1-L-DOPA did not significantly affected neither dopamine levels nor its turnover, indicating that dopamine synthesis was attenuated due to the KIE.  $\beta,\beta$ -D2-L-DOPA did not significantly affected dopamine levels, but the turnover of dopamine was higher when compared to L-DOPA, indicating faster dopamine degradation due to the inverse secondary deuterium KIE. In case of  $\alpha,\beta$ -D2-L-DOPA, dopamine production as well as its turnover was similar to that one of non-deuterated L-DOPA. Finally, D3-L-DOPA demonstrated increased potency in dopamine production and slower dopamine turnover when compared to L-DOPA.

Previous *in vivo* research of dopamine deamination (Yu et al., 1986; Miller and Klinman 1983) and mechanism of dopa decarboxylation (Giardina et al., 2011; Bertoldi 2014) does not explain the strong KIE in  $\alpha$ -D1-L-DOPA decarboxylation, the inverse KIE in  $\beta,\beta$ -D2-L-DOPA, or the role of simultaneous deuteration of  $\alpha$  and  $\beta$ -carbon of L-DOPA. Also, it is not clear why the triple deuteration yields the most powerful effect on dopamine production and its slow degradation; however, thanks to this, it is the only deuterated derivative which has higher potency in PD treatment than non-deuterated L-DOPA. It should be noted though, that in case of  $\alpha,\beta$ -D2-L-DOPA there are two forms (diastereomers) differing in chirality at  $\beta$  carbon, which may differ in dopamine output and degradation; this, however, was not taken into account in these studies.

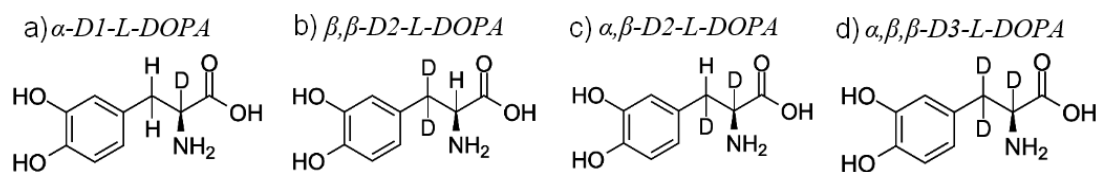


Figure 1.6: Deuterated forms of L-DOPA studied in the 2008 Malmjöf's study.

Further research has shown that 100% of D3-L-DOPA dose is equipotent to approximately 60% of L-DOPA dose. Consequently, D3-L-DOPA induced less dyskinesias in rodents. (Malmlöf et al., 2010)

Moreover, the effects of D3-L-DOPA alone have been proven to be similar to those produced by the treatment with L-DOPA combined with MAO inhibitor selegilin and it has been shown that pre-treatment with selegilin did not further potentiate the effect of D3-L-DOPA. This indicates that increased dopamine output may be attributed to decreased postsynaptic metabolism at MAO-B-containing sites. (Malmlöf, 2015)

### 1.3.3 Studies in healthy subjects

In a 2018 study of L-DOPA pharmacokinetics, metabolism and safety was performed in 16 healthy subjects after administration of single dose of the drug. It has shown that selective deuteration in D3-L-DOPA attenuates the peripheral metabolic degradation of deuterated dopamine and that peripheral pharmacokinetics and safety is comparable in healthy subjects to that of L-DOPA after single oral dose of the drugs.

This study gives the first clinical evidence in human showing that selective deuteration in the  $\alpha$  and  $\beta$  positions of the L-DOPA side chain causes a reduction of the metabolic breakdown of dopamine by MAO due to the intended deuterium isotope effect on this reaction. (Schneider et al., 2018)

## 1.4 Solubility

Solubility of a crystalline solid is dependent on its lattice energy which is a measure of the energy released when ions are combined to make up the crystal.

The molecule of levodopa consists of an aromatic ring with two hydroxyl groups and  $\alpha$ -amino acid chain. Amino acids are in general water-soluble thanks to their zwitterionic form in neutral pH, when the hydrogen from the acid carboxylic group transfers to the basic amine group forming a so called inner salt with the net charge being 0. (Figure 1.7)

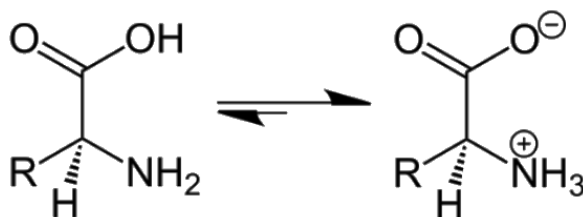
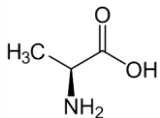
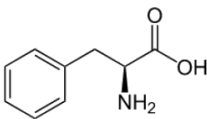
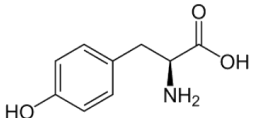
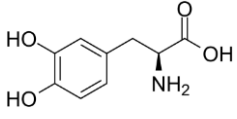


Figure 1.7: General  $\alpha$ -amino acid (left) and its zwitterionic form (right). Hydrogen transfers from the acidic carboxylic group to the basic amine group.

However, various *R* substituents interact differently with the zwitterions of surrounding molecules potentially affecting the lattice energy of the crystal and, therefore, the solubility. A solubility comparison of several amino acids in water is given in the Table 1.1. Solubility of phenylalanine is lowered by the presence of aromatic ring almost eight times when compared to alanine. Addition of a hydroxyl group in tyrosine further lowers the solubility fifty-six times. The second hydroxyl group in levodopa disrupts the lattice stability of the crystal which results in a ten times higher water solubility when compared to tyrosine. (Wishart et al., 2018)

Table 1.1: Water solubility of different  $\alpha$ -amino acids.

name	structure	solubility in water (Wishart et al., 2018)
alanine		204 mg/ml
phenylalanine		26.9 mg/ml
tyrosine		0.48 mg/ml
levodopa		5 mg/ml

L-DOPA in its zwitterionic form in water is soluble only up to 5 mg/ml (Wishart et al., 2018). It is much more soluble in basic or acidic solutes when it appears in a form of anion or cation, respectively. Depending on the pH, L-DOPA can have net charge +1, 0, -1, or -2. Theoretical dissociation constants and occurrences of different charge states of L-DOPA are shown in the Figure 1.8; yellow line indicates the zwitterionic form which outbalances the others in the pH region from 1.65 to approximately 8. In a strong acid L-DOPA exists in its cationic form with an extra hydrogen atom on the carboxylic group (red line). In basic medium, levodopa first loses hydrogen from the hydroxyl groups and then, with increasing alkalinity of the solvent, also the hydrogen from the amine group. Calculations were performed by Chemicalize package developed by (ChemAxon, 2019).

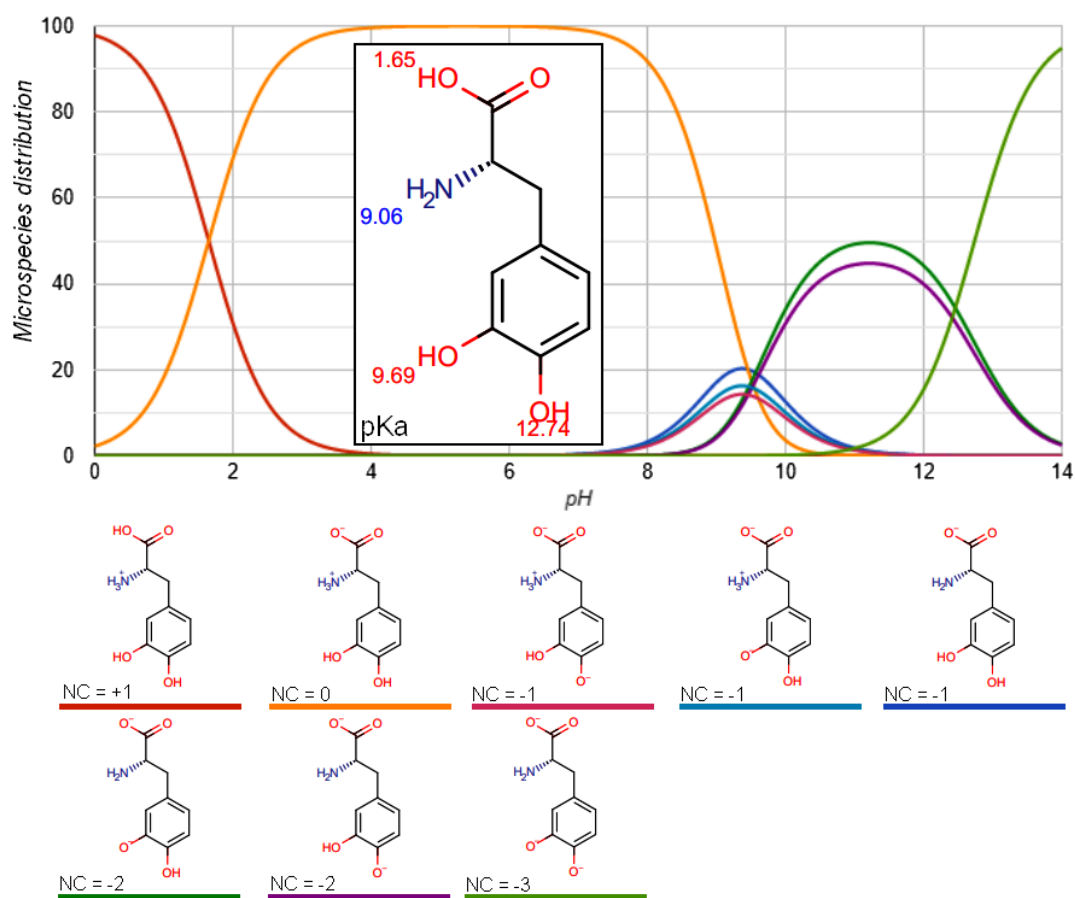


Figure 1.8: Calculated dissociation constants and occurrences of different charge states of L-DOPA depending on the pH of the solvent. The figure is adopted and edited from (ChemAxon, 2019). (NC – net charge)

## 1.5 L-DOPA as a model system

The zwitterionic form of L-DOPA in solid state was confirmed by X-ray diffraction (Mostad et al., 1970). Further it was confirmed that L-DOPA occurs in the *S*-enantiomeric form. This is with agreement with absolute configuration determination of others L-amino acids. (Mostad et al., 1971).

L-DOPA molecule may also serve as a suitable system for testing the boundaries of solution state molecular simulation methods. There are four functional groups strongly interacting with surrounding solvent molecules in L-DOPA – two hydroxyls, amine, and carboxyl. Depending on the pH, they might be differently charged. Taking account for correct solvent-solute interactions generally means including several explicit solvent molecules (at least the directly hydrogen bounded molecules in the first solvation sphere) which substantially increases the computational cost of *ab-initio* or DFT simulation. However, the information about the dynamics and flexibility of those functional groups can be obtained also from the molecular dynamics. This gives us the possibility to test the limits of implicit solvent models used in QM simulations.

Two vibrational spectral analysis of L-DOPA using the DFT method (Edwin and Hubert, 2013; Siddiqui, et al., 2010) and one study concerning the geometry optimisation (Elroby et al., 2012) have been published up to this point. The geometry optimisation study focuses rather on the bond lengths between the atoms than molecule's spatial arrangement and conformational preferences. Moreover, the study does not take into account the zwitterionic form of L-DOPA, in which it naturally occurs, and does not confirm its result with an experiment. Geometry optimisation of neutral (non-charged) as well as differently deprotonated conformers is performed on the DFT/B3LYP/6-311+G\*\* level of theory. It revealed that “*the geometry of the phenyl ring and its OH groups is planar but alaninyl side chain acts as a free rotor across several single bonds*” and that “*the deprotonation of the carboxyl group is more favourable than at other sites and leads to the accumulation of excess charge density on the nitrogen*” (Elroby et al., 2012) which corresponds to the formation of the zwitterion. The 2013 vibrational study (Edwin and Hubert, 2013) works with a monomer and dimer of L-DOPA in the optimized geometry with the lowest energy from (Elroby et al., 2012). Hence, it also does not take in account the zwitterionic form of L-DOPA. The spectra were computed also on the B3LYP/6-311+G\*\* level of theory. The study presents a comparison with experimental IR and Raman spectra,



however it is not very conclusive. The first conformational and vibrational study of L-DOPA published in 2010 (Siddiqui, et al., 2010) also does not work with the zwitterionic form of L-DOPA. They generated the possible L-DOPA conformers by Monte Carlo Multiple Minimum method and chosen the one with the lowest energy. The IR and Raman vibrational frequencies were computed using the B3LYP functional and 6-311+G(d,p) basis set and were compared to experimental vibrational frequencies measured by Sigma-Aldrich chemical company (USA). However, none of these studies presents an elaborate conformational study and most importantly, none of them performs the geometry and frequency analysis with the zwitterionic or cationic form of L-DOPA molecule.

In contrast with above mentioned publications, in this thesis we consider the zwitterionic and cationic form of L-DOPA both in the solid and liquid state. For DFT computations we use the 6-31+G\*\*, 6-31++G\*\*, and 6-311++G\*\* basis sets and either the B3LYP or the B3PW91 functional. We compare the computed vibrational frequencies to four experimental spectroscopic techniques (Raman, IR, ROA, and VCD). The fact that we are dealing with several deuterated analogues of L-DOPA enables also empirical assignment of some molecular vibrations related to the C-H (resp. C-D) motion, which nicely accompanies the spectral interpretation based on QM simulations. The numbering convention of the carbons in L-DOPA molecule adopted in this thesis is presented in the Figure 1.9. We have chosen not to number the other atoms because their designation would be redundant.

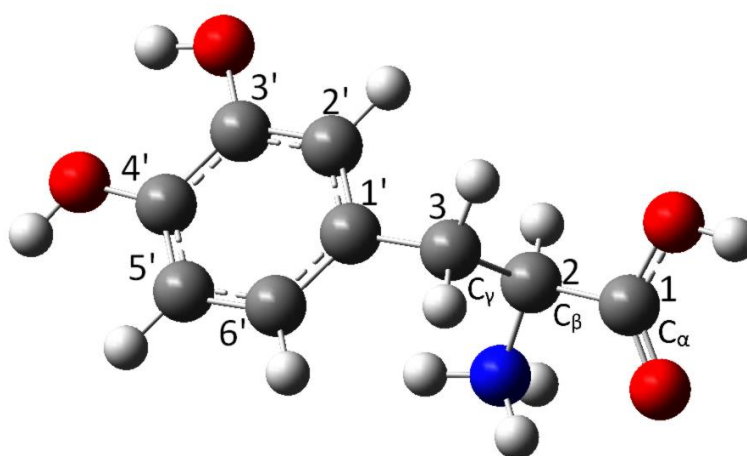


Figure 1.9: Numbering of L-DOPA molecule (cationic form) adopted in this thesis.

## 2 Fundamentals of vibrational spectroscopy

Molecules in general show three types of motion – translational, rotational, and vibrational. Given a molecule consisting of  $N$  atoms, it has  $3N$  degrees of freedom in total, including 3 translational and 3 (2 in case of a linear molecule) rotational. That leaves  $3N-6(5)$  degrees of freedom for vibrations.

For the purpose of this thesis we focus on quantum mechanical description of the molecular vibrations. First we deal with the approximation of Schrödinger equation and then with its application to the vibrational motion of diatomic molecule. In the end we present derivation of equations describing the vibrations of polyatomic molecules as well.

We follow selected parts of Molecular Quantum Mechanics by P. W. Atkins and R. S. Friedman (Atkins and Friedman, 2011) and Quantum Theory of Molecules by L. Skála (Skála, 1995).

### 2.1 Born-Oppenheimer approximation

Schrödinger equation cannot be solved analytically even for the simplest molecule  $H_2^+$ . To deal with that several approximations are used. Born-Oppenheimer approximation takes into consideration the great mass difference of electrons and nuclei. Electrons, being much lighter than the nuclei, are following their movement almost immediately, therefore we can account the nuclei as fixed in space and solve the Schrödinger equation for the electrons in their static electric potential. Also we can assume that nuclei react only very slowly to the change of electric field caused by the moving electrons so we can imagine nuclei being affected by the effective electric field of all the electrons.

Further we derive the Born-Oppenheimer approximation of a non-relativistic Schrödinger equation for a molecule with  $i$  electrons and  $j$  nuclei:

$$\left( -\frac{\hbar^2}{2m_e} \sum_i \Delta_i - \sum_j \frac{\hbar^2}{2M_j} \Delta_j + V \right) \psi = E\psi \quad (2.1)$$

here  $\hbar$  is reduced Planck constant,  $m_e$  is the mass of an electron,  $\Delta$  is the Laplace operator,  $M_j$  is the mass of  $j$ -th nucleus,  $V$  is the potential containing the

electron-electron, electron-nuclei, and nucleus-nucleus interactions,  $\psi$  is the wave function of the molecule and  $E$  is its energy in atomic units.

Based on the assumptions mentioned above, we can separate the wave function into a product of an electron wave functions in the field of  $j$ -th nucleus  $\varphi_{R_j}(\vec{r}_i)$  and the wave function of the nuclei  $\chi(\vec{R}_j)$ :

$$\psi(\vec{r}_i, \vec{R}_j) = \varphi_{R_j}(\vec{r}_i)\chi(\vec{R}_j). \quad (2.2)$$

Assuming that  $\varphi_{R_j}(\vec{r}_i)$  is the solution to the Schrödinger equation of the electrons in the potential of a steady nuclei, then the following applies:

$$\left(-\frac{\hbar^2}{2m_e} \sum_i \Delta_i + V\right) \varphi_{R_j}(\vec{r}_i) = U(\vec{R}_j) \varphi_{R_j}(\vec{r}_i), \quad (2.3)$$

where  $U(\vec{R}_j)$  is the effective potential energy for nuclei and it also includes the potential energies of internuclear repulsions at selected positions of nuclei and the energy of the electrons. It is called the potential energy surface of the molecule.

By combining equation (2.2) with (2.1) and using (2.3) we get the Schrödinger equation of the nuclei wave functions in a so-called adiabatic approximation:

$$U(\vec{R}_j) \varphi_{R_j}(\vec{r}_i) \chi(\vec{R}_j) - \sum_j \frac{\hbar^2}{2M_j} \left[ \chi(\vec{R}_j) \Delta_j \varphi_{R_j}(\vec{r}_i) + 2 \left( \nabla_j \varphi_{R_j}(\vec{r}_i) \right) \left( \nabla_j \chi(\vec{R}_j) \right) + \varphi_{R_j}(\vec{r}_i) \Delta_j \chi(\vec{R}_j) \right] = E \varphi_{R_j}(\vec{r}_i) \chi(\vec{R}_j). \quad (2.4)$$

Furthermore, assuming that the wave function of electrons  $\varphi_{R_j}(\vec{r}_i)$  changes only little with the movement of the nuclei which is called Born-Oppenheimer approximation, we get

$$\begin{aligned} \Delta_j \varphi_{R_j}(\vec{r}_i) &= 0, \\ \nabla_j \varphi_{R_j}(\vec{r}_i) &= 0, \end{aligned} \quad (2.5)$$

and consequently

$$-\sum_j \frac{\hbar^2}{2M_j} \Delta_j \chi(\vec{R}_j) + U(\vec{R}_j) \chi(\vec{R}_j) = E \chi(\vec{R}_j), \quad (2.6)$$

where  $E$  is the total energy of the molecule, consisting of the translational, rotational, vibrational and electronic energies:

$$E = E_{trans} + E_{rot} + E_{vib} + E_{el}. \quad (2.7)$$

## 2.2 Vibrations of diatomic molecules

### 2.2.1. Harmonic approximation

When nuclei are displaced from the equilibrium position, their potential energy  $V(x)$  increases. For small displacement  $x$  we can expand the potential into Taylor series and neglect terms higher than second order. Furthermore, we can set the potential in equilibrium  $V(0) = 0$ . This represents the harmonic approximation of the potential:

$$V(x) = \frac{1}{2} kx^2, \text{ where } k = \left( \frac{d^2V}{dx^2} \right)_{x=0}. \quad (2.8)$$

The Hamiltonian for a diatomic molecule with masses  $m_1$  and  $m_2$  is

$$H = -\frac{\hbar^2}{2\mu} \frac{d^2}{dx^2} + \frac{1}{2} kx^2, \quad (2.9)$$

where  $\mu = \frac{1}{m_1} + \frac{1}{m_2}$  is the effective mass.

Equation (2.9) corresponds to a Hamiltonian of a linear harmonic oscillator for which the solution is well known:

$$E = \hbar\omega \left( v + \frac{1}{2} \right), \text{ where the frequency } \omega = \sqrt{\left( \frac{k}{m} \right)}. \quad (2.10)$$

Here  $v = 1, 2, \dots$  are individual vibrational energy levels of the molecule equally separated by the distance  $\hbar\omega$ .

### 2.2.2. Vibrational selection rules

Consider a molecule in the state  $|\varepsilon, v\rangle$  where  $\varepsilon$  and  $v$  denote its electronic and vibrational state, respectively. The change of the electric dipole moment operator  $\hat{\mu}$  under the transition from one vibrational state ( $v$ ) to another ( $v'$ ) is given by the transition matrix element

$$\hat{\mu}_{v'v} = \langle v' | \hat{\mu}_\varepsilon | v \rangle. \quad (2.11)$$

Here  $\hat{\mu}_\varepsilon$  is dipole moment of the molecule in a particular electronic state  $\varepsilon$ . We get that by performing the integration over the electronic state which can be done separately thanks to Born-Oppenheimer approximation.

The dipole moment depends on the displacement of nuclei, therefore we can expand it into Taylor expansion as

$$\hat{\mu} = \hat{\mu}_0 + \left( \frac{d\hat{\mu}}{dx} \right)_0 x + \frac{1}{2} \left( \frac{d^2\hat{\mu}}{dx^2} \right)_0 x^2 + \dots \quad (2.12)$$

where  $\hat{\mu}_0$  is the dipole moment for null displacement.

By combining equations (2.11) and (2.12), taking into account the orthogonality of the vibrational states for  $\nu' \neq \nu$  and considering only small displacements (i.e. neglecting the terms of higher order than linear), we get the transition matrix element

$$\langle \nu' | \hat{\mu}_\varepsilon | \nu \rangle = \left( \frac{d\hat{\mu}_\varepsilon}{dx} \right)_0 \langle \nu' | x | \nu \rangle \quad (2.13)$$

which is non-zero only when the dipole moment varies with displacement.

Hence we can conclude that for a molecule to show vibrational spectra, it must have a dipole moment which changes with displacement of the nuclei.

By further investigation of the conditions under which  $\langle \nu' | x | \nu \rangle \neq 0$  it was found that the allowed vibrational transitions are only those when initial and final vibrational states differ by unity, i. e.

$$\Delta\nu = \pm 1. \quad (2.14)$$

This is the selection rule for vibrational transition of an electric dipole in harmonic approximation, it only allows transitions between two neighbouring vibrational levels.

### 2.2.3. Selection Rules for Raman transition

For Raman transition the induced dipole moment is defined by the polarizability  $\hat{\alpha}$ :

$$\hat{\mu} = \hat{\alpha} \hat{E}. \quad (2.15)$$

Using the same approach as in section 2.2.2., we can separate electronic and vibrational wavefunction, evaluate  $\langle \varepsilon | \hat{\alpha} | \varepsilon \rangle$ , and write:

$$\langle \nu' | \hat{\mu} | \nu \rangle = \left( \frac{d\hat{\alpha}}{dx} \right)_0 \cdot \hat{E} \langle \nu' | x | \nu \rangle, \quad (2.16)$$

which again leads us to the conclusion that for the vibration to be visible in the Raman spectrum, the displacement of the atoms must change the polarizability of the molecule. Also the Raman selection rules are the same as the vibrational ones:

$$\Delta\nu = \pm 1. \quad (2.17)$$

### 2.2.4. Polyatomic molecules

In practise we always deal with the vibrations of atoms in polyatomic molecules, in which the potential energy depends on the displacements of all atoms in the molecule, so in the harmonic approximation we get:

$$V = \frac{1}{2} \sum_{i,j} \left( \frac{\partial^2 V}{\partial x_i \partial x_j} \right) x_i x_j \quad (2.18)$$

We now introduce the mass-weighted coordinates  $q_i = \sqrt{m_i} x_i$ , where  $m_i$  is the mass of an atom displaced by  $x_i$ . Hence we can express potential energy in the form

$$V = \frac{1}{2} \sum_{i,j} K_{ij} q_i q_j, \text{ where } K_{ij} = \left( \frac{\partial^2 V}{\partial q_i \partial q_j} \right). \quad (2.19)$$

For the total energy of the molecule we get:

$$E = \frac{1}{2} \sum_i \dot{q}_i^2 + \frac{1}{2} \sum_{i,j} K_{ij} q_i q_j. \quad (2.20)$$

The terms which make difficulties in the computation are those where  $i \neq j$ ; therefore, it is desirable to find a linear combination  $Q_i$  of the coordinates  $q_i$  thanks to which we rewrite the energy as

$$E = \frac{1}{2} \sum_i \dot{Q}_i^2 + \frac{1}{2} \sum_i \lambda_i Q_i^2, \quad (2.21)$$

with  $\lambda_i$  being the coefficients.

Some of the linear combinations  $Q_i$  correspond to the translational and rotational motion. For such we expect  $\lambda_i = 0$ . Linear combinations that enable this separation are called normal coordinates.

The Hamiltonian in normal coordinates has the form

$$H = \frac{1}{2} \sum_i -\hbar^2 \frac{\partial^2}{\partial Q_i^2} + \lambda_i Q_i^2. \quad (2.22)$$

For a non-linear molecule the Hamiltonian is a sum of  $3N-6$  harmonic-oscillator Hamiltonians, each corresponding to one of the independent vibrating modes  $\nu_i$  of the molecule which are called the normal modes. The wavefunction of the molecule  $\psi$  is the product of all the  $3N-6$  wavefunctions of the normal modes:

$$\psi = \prod_{i=1}^{3N-6} \psi_{\nu_i}(Q_i). \quad (2.23)$$

Total energy of the molecule is the sum of the energies of normal modes:

$$E = \sum_{i=1}^{3N-6} \left( v_i + \frac{1}{2} \right) \hbar \omega_i, \quad (2.24)$$

where  $\omega_i$  is the frequency of the mode.

Regarding the selection rules for vibrational and Raman transition, we can extend them to the normal coordinates by rewriting the equations (2.13) and (2.16) for each normal vibrational mode  $v_i$  as

$$\langle v_i' | \hat{\mu}_\varepsilon | v_i \rangle = \left( \frac{d\hat{\mu}_\varepsilon}{dQ_i} \right)_0 \langle v_i' | Q_i | v_i \rangle \quad \text{and} \quad \langle v_i' | \hat{\alpha} | v_i \rangle = \left( \frac{d\hat{\alpha}}{dQ_i} \right)_0 \cdot \hat{E} \langle v_i' | Q_i | v_i \rangle, \quad (2.25)$$

respectively.

Allowed transitions are in both cases those where  $v_i' = v_i \pm 1$ . The fundamental transition of a molecule is such during which a single mode transits from  $v_i = 0$  to  $v_i' = 1$  and *vice versa* while all the others remain in the same level.

If the displacement of a nuclei along normal coordinate changes the electric dipole moment, that is  $\left( \frac{d\hat{\mu}_\varepsilon}{dQ_i} \right)_0 \neq 0$ , then the appropriate normal mode  $v_i$  is said to be infrared active because it contributes to the vibrational IR absorption or emission of the molecule. If, on the other hand, the displacement of nuclei along normal coordinate changes the polarizability, that is  $\left( \frac{d\hat{\alpha}}{dQ_i} \right)_0 \neq 0$ , the appropriate normal mode  $v_i$  is said to be Raman active because it contributes to the Raman spectra of the molecule.

### 3 Methods of vibrational spectroscopy

By applying electromagnetic radiation of different energies, we are able to study different transitions in the molecule. Frequencies of molecular vibrations correspond mostly to the frequencies of the infrared part of electromagnetic radiation. Hence, to study vibrational transitions, we use infrared spectroscopy (IR) based on direct absorption of infrared light, or Raman spectroscopy (RS) based on the inelastic scattering of visible light.

The positions of the peaks in the spectra are usually given by their wavenumber, in the units of  $\text{cm}^{-1}$ , which is defined as

$$\tilde{\nu} = \frac{1}{\lambda}, \quad (3.1)$$

where  $\lambda$  is the wavelength corresponding to the frequency of the vibration.

Vibrational spectra of the molecules can be divided into three regions: (i) low-wavenumber region ( $0 - 400 \text{ cm}^{-1}$ ), (ii) so called fingerprint region (around  $400 - 1400 \text{ cm}^{-1}$ ) which is unique for each compound, and (iii) the functional group region (around  $1400 - 4000 \text{ cm}^{-1}$ ) where the vibrations of functional groups occur. (El-Azazy 2018) Infrared spectrometers usually operate in the mid infrared region, that is  $2.5\text{-}25 \mu\text{m}$  (around  $400 - 4000 \text{ cm}^{-1}$ ), and the absorbed frequencies give rise to the absorption spectra. Raman spectrometers, on the other hand, use only monochromatic source of visible light which is not absorbed by the molecule. Such light is being scattered mostly without the change in energy by Rayleigh scattering; however, some of the scattered light (approximately one millionth of it) is scattered inelastically having higher or lower energy, giving rise to the anti-Stokes or Stokes lines in Raman spectra, respectively.

In this chapter we describe the general theory of vibrational spectroscopy and also the theory of specific methods used in our work. We follow selected parts of (Prosser et al., 1986).



### 3.1 Infrared absorption spectroscopy (IR)

#### 3.1.1. Process of absorption

When light of a frequency  $\nu$  passes through translucent material its intensity decrease. Physical quantity characterising this phenomena is called absorbance and it is defined as

$$A(\nu) = \log \frac{I_0(\nu)}{I(\nu)}, \quad (3.2)$$

where  $I_0(\nu)$  and  $I(\nu)$  are the intensities of incident and transmitted light, respectively. According to Lambert law, absorbance depends linearly on the distance  $l$  travelled by light in the sample being propotional to the attenuation coefficient  $b$ :

$$A(\nu) = lb(\nu). \quad (3.3)$$

By combination of equations (3.2) and (3.3) we arrive to the expression for the intensity decrease

$$I(\nu) = I_0(\nu)e^{-b(\nu)l}. \quad (3.4)$$

Furthermore, according to the Beer law the extinction coefficient is proportional to the molar attenuation coefficient  $\varepsilon(\nu)$  and the molar concentration of the sample  $c$ :

$$b(\nu) = c \varepsilon(\nu). \quad (3.5)$$

Thus we obtain the Beer-Lambert law for absorbance:

$$A(\nu) = lc\varepsilon(\nu) \quad (3.6)$$

The most common technique of acquisition of absorption spectra of liquid sample in a cuvette is measuring the transmittance  $T(\lambda)$  which is defined as the ratio of the intensity of transmitted light to the intensity of incident light:

$$T(\lambda) = \frac{I(\lambda)}{I_0(\lambda)} \quad (3.7)$$

To eliminate the reflection from the sample-air interface, usually the relative transmittance  $T_{rel}(\lambda) = \frac{I(\lambda)}{I_{ref}(\lambda)}$  is measured, where  $I_{ref}(\lambda)$  is the intensity of light transmitted through the cuvette containing the pure solvent.

#### 3.1.2. IR spectrometers

Modern IR spectrometers are built as Fourier transform infrared spectrometers (FTIR). As the name implies, they use two Fourier transforms to obtain the spectra. First one is performed by the interferometer which is built-in the spectrometer. We will now shortly describe the principle of Michelson interferometer shown in the

Figure 3.1. Light from the black body-like source is split by a beam splitter into two separate beams. One of them continues to a fixed mirror (in distance  $l$ ) where it reflects and travels back. The second one is reflected from a movable mirror. If the mirror deflection from the distance  $l$  is  $d$ , it generates a length difference  $2d$  in the path of both beams. When the two beams interfere, constructive interference happens only for the wavelength  $\lambda$  for which  $d = \frac{k\lambda}{2}$ , where  $k$  is an integer. By detecting transmittance for different values of  $d$ , the interferogram is obtained and subsequently converted to a transmission spectrum by the second Fourier transform performed by a computer.

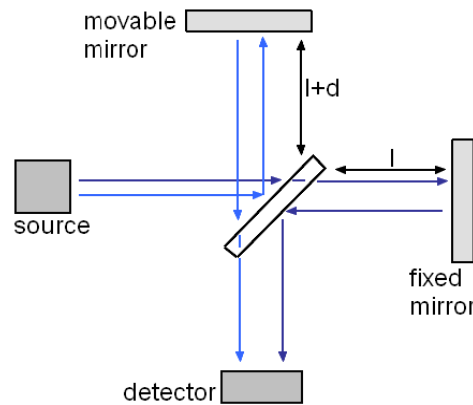


Figure 3.1: Michelson interferometer: by changing the distance  $d$ , only the wavelengths for which  $d = \frac{k\lambda}{2}$ , where  $k$  is an integer, are selected from continuous spectra.

The use of Fourier transform is conditioned by the advances in microtechnology. In the past only dispersion infrared spectrometers were used. These measure transmittance of only one wavelength at a time using a monochromator. Nowadays, dispersion spectrometers are not used for routine measurements because of their relatively high signal-to-noise ratio and long measurement time compared to FTIR spectrometers, but they are still used for special applications like time-resolved measurement. (Barth, 2007)

## 3.2 Raman spectroscopy

### 3.2.1 Raman effect

Let us consider a molecule in a ground electronic state. In contrast to absorption, where molecule changes its vibrational or electronic state and the energy of the absorbed photon is the same as the energy difference of the vibrational or electronic states, Raman scattering is an off-resonance two-photon process in which the molecule is excited into unstable virtual energy state. From there it immediately transits back into a) the ground electronic state, in which case we are dealing with elastic Rayleigh scattering, b) one of the higher vibrational energy states of the electronic ground state which leads to Stokes Raman scattering, hence the molecule gains energy, or c) the molecule's initial energy state is one of the higher vibrational states and after absorbing the radiation it transits to the ground vibrational state by emission of a photon of higher energy than that of absorbed photon. The last case is called anti-Stokes Raman scattering and the molecule loses energy. Figure 3.2 illustrates all three possible transitions. Although it is not technically process of absorption and emission, it is often referred to as such.

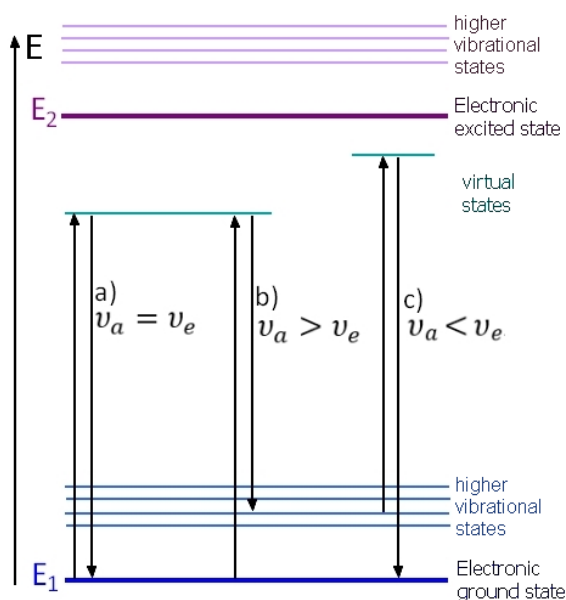


Figure 3.2: Three possible transitions of molecular energy state after absorption of light: a) Rayleigh scattering, where the energy of emitted light is the same as of the incident light b) Stokes Raman scattering, where the energy of emitted light is lower than that of the incident light c) anti-Stokes Raman scattering where the energy of emitted light is higher than that of the incident light.  $\nu_a$  and  $\nu_e$  stand for the frequency of absorbed and emitted light, respectively.

The difference in wavelengths of incident and emitted radiation ( $\lambda_i$  and  $\lambda_e$ , respectively) is called the Raman shift and it corresponds to the energy difference between initial and final state of the molecule. It is defined as

$$\Delta\tilde{\nu} = \frac{1}{\lambda_i} - \frac{1}{\lambda_e}. \quad (3.8)$$

Therefore, the magnitudes of the shifts of Stokes and anti-Stokes lines are the same for given vibrational state and they are independent of the initial light frequency.

Intensity of scattered light increases with the fourth power of the frequency of the incident light. The vast majority of incident photons, more than 99,9999 %, is scattered elastically. The probability (cross section) of Raman scattering is much lower, only one of every  $10^6$ - $10^8$  photons scatters inelastically. (Smith and Dent, 2004) Therefore, Raman lines in molecule's spectra are much less intense. Moreover, because the vast majority of molecules occurs in the ground state at room temperature, the intensity of anti-Stokes lines is even lower than that of the Stokes lines. An illustration of Raman spectrum is shown in Figure 3.3.

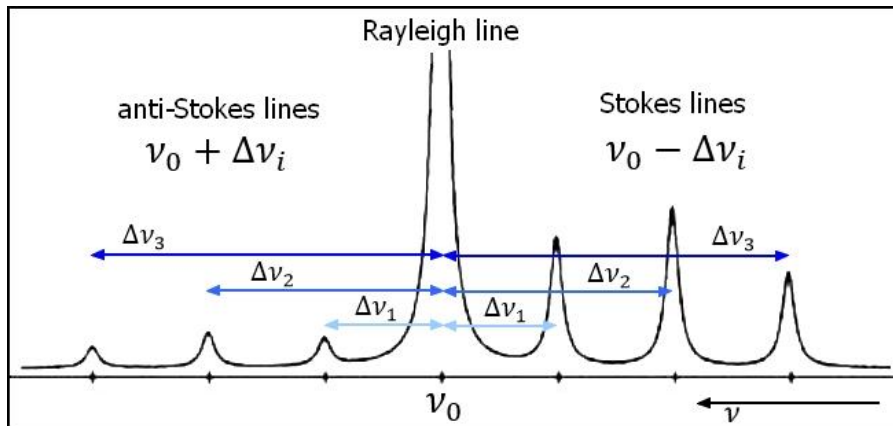


Figure 3.3: Illustration of Raman spectrum. In the middle at  $\nu_0$  (frequency of the incident radiation), is shown the Rayleigh line of elastic scattering, the left side of the spectrum is formed by anti-Stokes lines and the right side by Stokes lines. The value of frequency increases from right to left. Raman shift  $\Delta\nu_i$  equals to energy difference between molecule's initial and final state.

Using the classical theory we can describe the Raman effect as follows (B&W Tek., 2019): Consider a polarized coherent monochromatic light oscillating with frequency  $\nu_0$  and amplitude  $E_0$ . Such light can be described by equation of harmonic electric field

$$E = E_0 \cos(2\pi\nu_0 t). \quad (3.9)$$

This light interacts with the electron clouds of the molecules and distorts them, creating a dipole moment  $\mu$  of properties dependent on the ability of the electron cloud to be polarized:

$$\mu = \alpha E . \quad (3.10)$$

If the molecule vibrates with the frequency  $\nu_m$  and amplitude  $x_0$ , the displacement of the nucleus  $x$  is given by equation

$$x = x_0 \cos(2\pi\nu_m t). \quad (3.11)$$

Polarizability is a function of  $x$  hence for small amplitude of vibration we can use harmonic approximation of polarizability:

$$\alpha = \alpha_0 + \left( \frac{\partial \alpha}{\partial x} \right) \Big|_{x=0} x, \quad (3.12)$$

where  $\alpha_0$  is the equilibrium position of polarizability.

Combining equations (3.9)-(3.12) we get

$$\begin{aligned} \mu = & \alpha_0 E_0 \cos(2\pi\nu_0 t) \\ & + \frac{1}{2} \left( \frac{\partial \alpha}{\partial x} \right) \Big|_{x=x_0} x_0 E_0 (\cos 2\pi(\nu_0 - \nu_m) + \cos 2\pi(\nu_0 + \nu_m)). \end{aligned} \quad (3.13)$$

The first term of equation (3.13) represents a dipole oscillating with frequency  $\nu_0$  which corresponds to the Rayleigh scattering. The other two terms representing dipoles with frequencies  $(\nu_0 - \nu_m)$  and  $(\nu_0 + \nu_m)$  correspond to Stokes and anti-Stokes Raman scattering, respectively. If  $\left( \frac{\partial \alpha}{\partial x} \right) = 0$ , the last two terms would disappear meaning that the vibration is Raman-inactive.

### 3.2.2 Raman spectrometer

Unlike in IR absorption, monochromatic source of light is sufficient in Raman spectrometers to obtain the whole Raman spectra. Since the intensity of scattered light is proportional to the fourth power of its frequency, it seems desirable to work in the UV region but unfortunately many compounds absorb UV radiation which leads to complications in obtaining UV Raman spectra. Thus, most Raman spectrometers employ visible or near IR lasers.

Even though Fourier-transform Raman spectrometers with near IR light source exist, the most common are disperse Raman spectrometers which use visible light for excitation. (Smith and Dent, 2004) In principle, scattered light can be collected from every direction, however, three main scattering geometries are employed in common practice – forward scattering, right-angle scattering, and backward scattering (see

Figure 3.4). In forward scattering the laser beam passes through the sample and the scattered light is collected behind the sample while the laser beam is screened out. In  $90^\circ$  geometry the laser beam passes through the sample and the scattered light is collected by a lens positioned at  $90^\circ$  with respect to the beam. In the backward, or  $180^\circ$ , geometry the path of the laser beam is guided by a system of mirrors to the lens-sample connecting line. The last geometry is mostly used in Raman microscopes.

Most of the scattered light collected by lenses is due to the Raleigh scattering. This is filtered out usually by a notch filter which absorbs at the frequency of incident laser light and a little band around it (usually within  $200\text{ cm}^{-1}$ ) or edge filter which cuts off the Rayleigh as well as the anti-Stokes Raman scattering. Filtered light then passes through a monochromator which spatially separates different wavelengths of Raman-scattered light and finally it is recorded by a coupled charged device (CCD) detector. (Smith and Dent, 2004)

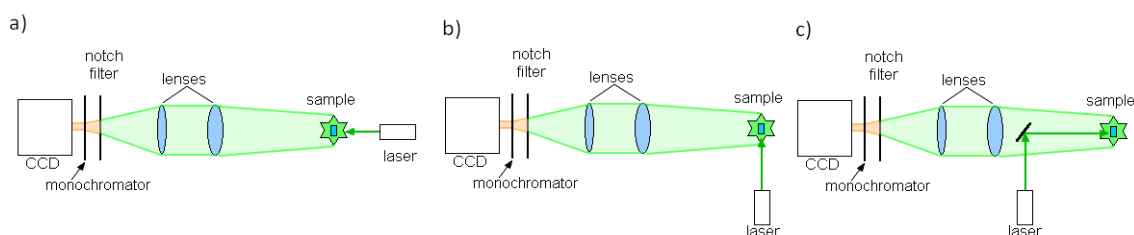


Figure 3.4: possible geometries of Raman spectrometer. a) forward-scattering geometry b)  $90^\circ$  geometry c)  $180^\circ$  geometry.

### 3.3 Vibrational optical activity (VOA)

Methods of VOA are based on the optical activity of chiral molecules. They include two separate techniques: vibrational circular dichroism (VCD) and Raman optical activity (ROA), both resulting in difference vibrational spectra with respect to right- and left-circularly polarized light. Former reveals optical activity of molecules using IR absorption and the latter uses Raman scattering.

#### 3.3.1 Chirality

Chiral molecules are such which are not similar to their mirror images (as shown in the Figure 3.5). In organic molecules the most common cause of chirality is the presence of a carbon that is attached to four different atoms or atom groups, so called asymmetric carbon. The molecules which differ only in the spatial arrangement of the

atoms are called stereoisomers and one of such molecules is referred to as an enantiomer.

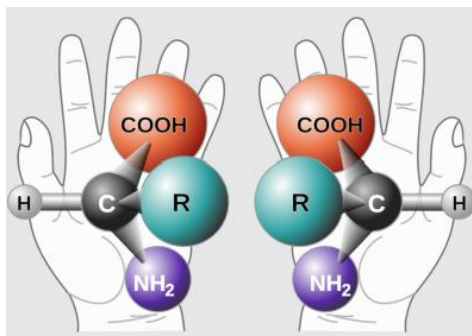


Figure 3.5: Demonstration of left handed and right handed chiral molecule. Adapted from (Renstrom, 2018).

There are several nomenclatures which use different conventions to distinguish between the enantiomers:

(i) by absolute configuration of the molecules we distinguish *R*- and *S*-enantiomers (Figure 3.6). Each atom or group on the chiral centre is assigned a priority based on its atomic number. The centre is then oriented so that the atom with the lowest priority points away from the viewer. The crucial criterion is if the priority of the remaining substituents decreases in clockwise direction, in which case we are dealing with *R*- enantiomer (*R* stands for Latin word Rectus which means right), or anti-clockwise which is the case of *S*- enantiomer (*S* for Sinister, Latin for left).

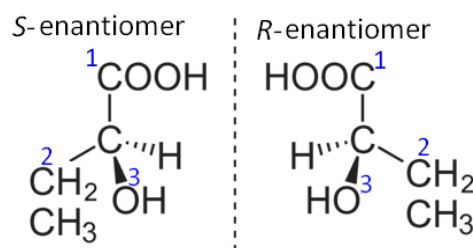


Figure 3.6: Example of *S*- and *R*- enantiomers.

(ii) Enantiomers differ in their optical activity. Based on that we distinguish enantiomers which rotate the plane of polarized light clockwise, the (+)- enantiomer, or anticlockwise, the (-)- enantiomer (Figure 3.7)

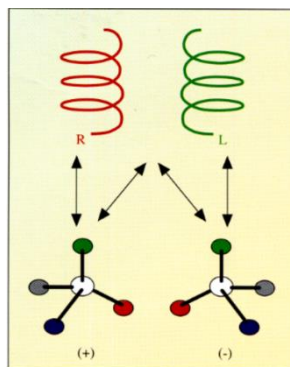


Figure 3.7: Illustration of right- and left-circularly polarized light and (+) - and (-)-enantiomers of the same molecule. (Nafie, 1996)

(iii) By compound's stereochemistry relative to the geometry of the dextrorotatory, (+) -, or levorotatory, (-) -, enantiomers of glyceraldehyde we distinguish D- and L-enantiomers, respectively. This convention is not related to the actual optical activity of the molecules, dextrorotatory enantiomer of glyceraldehyde is indeed an D-enantiomer, however, 9 of 19 L-amino acids commonly found in the proteins are dextrorotatory.

### 3.3.2 Vibrational circular dichroism (VCD)

IR absorption associated with VCD is a one-photon process. Hence, there is only one way to define VCD – as the difference of absorbance of the sample for left- and right-circularly polarized light:

$$\Delta A = A_L - A_R. \quad (3.14)$$

Illustration of the process of absorption is shown in the Figure 3.8 bellow. Letters g and e mark the ground and excited electronic or vibrational state of the molecule, R and L the right- and left-circularly polarized light, respectively, and A marks the absorption of light.

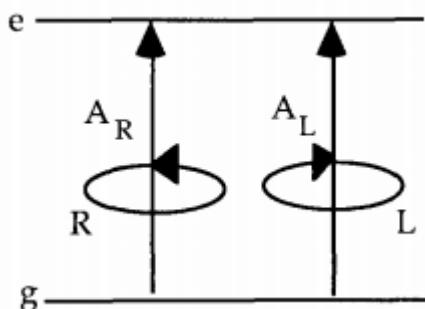


Figure 3.8: Process of absorption of right- (R) or left- (L) circularly polarized light. Adapted from (Nafie, 1995).



Intensity of VCD signal depends on the magnetic-dipole interactions of molecule and radiation. The anisotropy ratio  $g$  is defined as the ratio of experimental VCD absorbance to the experimental infrared absorbance:

$$g = \frac{\Delta A}{A} \quad (3.18)$$

Theoretically this is proportional to the ratio of rotatory strength  $R$  and dipole strength  $D$ :

$$g = \frac{4R}{D} = \frac{4Im(\vec{\mu} \cdot \vec{m})}{|\mu|^2} \quad (3.19)$$

Here  $\vec{\mu}$  and  $\vec{m}$  denote the electric and magnetic dipole transition moment, respectively. Dipole strength is always positive, whereas the sign of the rotatory strength depends on the relative directions of the electric and magnetic dipole transitions moments.

### 3.3.3 Raman optical activity (ROA)

Raman scattering, on the contrary of absorption, is a two photon process; therefore, there are more possibilities to the arrangement of ROA experiment. Namely, incident circular polarization (ICP) ROA, scattered circular polarization (SCP) ROA, in-phase dual circular polarization (DCP<sub>I</sub>) ROA and out-of-phase dual circular polarization (DCP<sub>II</sub>) ROA. As their names imply, they differ in the polarization of the incident and detected scattered light. All forms of ROA are shown in the Figure 3.6 and they are defined as follows:

$$\begin{aligned} \text{ICP: } \Delta I_u(\xi) &= I_u^R(\xi) - I_u^L(\xi) \\ \text{SCP: } \Delta I^u(\xi) &= I_R^u(\xi) - I_L^u(\xi) \\ \text{DCP}_I: \Delta I_I(\xi) &= I_R^R(\xi) - I_L^L(\xi) \\ \text{DCP}_{II}: \Delta I_{II}(\xi) &= I_L^R(\xi) - I_R^L(\xi). \end{aligned} \quad (3.17)$$

The superscript and subscript denote the polarization of the incident and detected radiation, respectively,  $u$  stands for unpolarised, and  $\xi$  is the scattering angle which depends on the spectrometer geometry. For instance, in case of ICP-ROA the polarization of incident radiation is modulated between right and left circular states and unpolarised scattered light is detected. The most commonly used techniques are SCP-ROA and DCP<sub>I</sub>-ROA thanks to the highest signal gain of all methods.

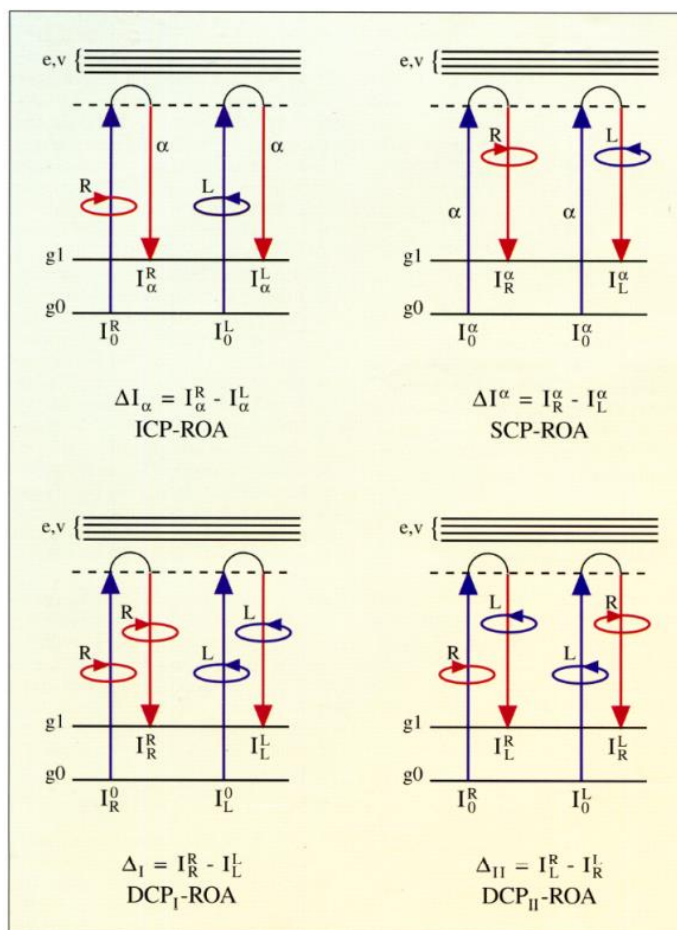


Figure 3.9: Different arrangements of ROA experiments. (Nafie, 1996)

Like in the case of VCD, intensity of ROA also depends on the magnetic-dipole interactions of the molecule and radiation, but ROA additionally depends also on the electric-quadrupole interaction.

ROA intensity is expressed as the circular intensity difference (CID). It is the ratio of ROA to regular Raman intensities, which can be theoretically expressed as the ratio of linear combinations of ROA tensor invariants to ordinary Raman polarizability invariants. For instance in case of SCP-ROA the CID is

$$\Delta_u = \frac{\Delta I_u}{I_u} = \frac{48}{c} \frac{[3\beta(G)^2 + \beta(A)^2]}{2[45\alpha^2 + 7\beta(\alpha)^2]}, \quad (3.20)$$

where  $\beta(G)^2$  and  $\beta(A)^2$  are the magnetic-dipole and electric-quadrupole anisotropic Raman optical activity invariants, respectively, and  $\alpha$  and  $\beta(\alpha)^2$  are the isotropic and anisotropic Raman polarizability invariants.

### 3.4 Comparison of IR and Raman spectroscopy

Raman and IR spectroscopy are complementary techniques. They use different physical phenomena to gain spectra of molecules and usually the employment of both of them is beneficial for acquiring the detailed information about vibrational behaviour of studied molecule. While IR spectra are the result of one-photon resonance process, the absorption of electromagnetic radiation, Raman spectra are produced thanks to an off-resonance two-photon inelastic scattering process. Raman spectroscopy depends on a change of polarizability of a molecule, whereas IR spectroscopy depends on a change in the dipole moment. Raman spectroscopy is best at vibrations of nonpolar or homo-nuclear groups, while IR spectroscopy is best at the asymmetric vibrations of polar or hetero-nuclear groups. (Larkin, 2017; Exline, 2013).

The advantage of Raman spectroscopy is that it requires little to no sample preparation, while the IR spectroscopy is limited by the requirement of sample uniformity, thickness, and dilution to avoid high absorbance. Moreover, the measurable spectral range of sample's absorption is limited by the cuvette absorbance. IR spectra, on the other hand, are not affected by the fluorescence of the sample; however, IR absorbance of water often intervenes with the liquid sample spectra, if used as a solvent. (Exline, 2013).

Following table gives a summary of main differences between Raman and IR spectroscopy:

Table 3.1: Comparison of Raman and infrared spectroscopy. Adopted from (Peeran, 2005)

<b>Raman</b>	<b>IR</b>
It is due to the scattering of light by the vibrating molecules.	It is the result of absorption of light by vibrating molecules.
The vibration is Raman active if it causes a change in polarisability.	Vibration is IR active if there is change in dipole moment.
The molecule need not possess a permanent dipole moment.	The vibration concerned should have a change in dipole moment due to that vibration.
Water can be used as a solvent.	Water cannot be used due to its intense absorption of IR.
Sample preparation is not very elaborate, it can be in any state.	Sample preparation is elaborate Gaseous samples can rarely be used.
Gives an indication of covalent character in the molecule.	Gives an indication of ionic character in the molecule.
Cost of instrumentation is very high	Comparatively inexpensive.

## 4 Quantum mechanical simulations

Computational simulations of molecular properties have wide range of applications in physical chemistry including interpretation of experimental spectra, the absolute configuration determination, determination of the structure of biomolecules and biomolecular systems, and the elucidation of their mechanism of action. Large molecules with high degrees of freedom are modelled empirically with the use of molecular force fields models of smaller compounds. Small and medium sized molecules with less than 100 atoms can be computed using *ab-initio* methods.

### 4.1 Ab-initio methods

*Ab-initio* calculation methods are based merely on the laws of physics, lacking the use of empirical data. Their aim is to solve the multi-electron Schrödinger equation of a molecule in Bohr-Oppenheimer approximation (see section 2.1). However, the Schrödinger equation can be solved analytically only for one-electron systems such as hydrogen atom and diatomic hydrogen ion. Thus, for the multi-electron atoms and molecules, it has to be solved numerically with the employment of approximate methods such as the variational principle and perturbation theory. *Ab-initio* computations of properties of larger molecules or molecular systems tend to be time and cost consuming.

The available quantum chemical methods can be divided into wavefunction and density-based methods, depending on whether they are built upon an *ab initio* wavefunction requiring a Hartree – Fock ground state calculation as prerequisite, or whether they formally require a ground state electron density derived from Kohn – Sham density functional theory (DFT). (Comba, 2011)

#### 4.1.1 Hartree-Fock theory (HF)

HF, also called the Self-Consistent Field method (SCF), is an iterative technique which uses a model of non-correlated electrons to obtain the molecular orbitals. Thanks to the approximation of non-interacting electrons, the wave function of the stationary state can be represented by the Slater determinant, a product of single-electron wave functions (i.e. spin-orbitals for the calculation of an atomic orbital or the linear combination of atomic orbitals, LCAO, for a molecular orbital) and the Hamiltonian as a sum of single-electron Hamiltonians in Born-Oppenheimer approximation. Subsequently, the variational method is used to find the energy

estimate and the coefficients of the atomic orbitals in the LCAO. HF method is then iterated with thus created wavefunction until the energies converge. The derivation of HF and illustrative calculations can be found for instance in (Szabo and Ostlund, 1996).

The advantage of HF method is a low computational expense. Nevertheless, the neglect of the electron correlation can lead to large disagreement with the experimental data. Therefore, to improve the molecular model, it is necessary to include the correlations and interactions of the electrons. There are different approaches of doing so and all together are called the Post-Hartree-Fock methods. Their summary can be found in (Townsend et al., 2019 and Magnasco, 2013)

The refinement of the computational results usually requires much higher computational power and it is therefore costly and even unaffordable for large systems.

#### 4.1.2 Density functional theory (DFT)

A different approach of computing the electronic structure is represented by DFT. It introduces the concept of an electron-density distribution of the physical system which contains the same information as the wavefunction. The ultimate goal of DFT is calculation of electron-density distribution without the use of the wave function of the system. (Piel, 2020) Unlike HF theory, it does not neglect the correlation of the electrons; it rather takes them into account from the very beginning.

DFT relies on the formulation of the Hohenberg-Kohn (HK) theorem which postulates the existence of exchange-correlation functional which is minimized by the ground-state electron density distribution giving the energy of the ground state. The ground-state energy includes the problematic exchange-correlation energy of the electrons which corresponds to the exchange-correlation potential. The mathematical form of the HK functional is not known, but its approximations yield results that are highly sufficient. Once the energy approximation is obtained, the iterative process of solving HK equations (analogous to the HF method) is applied until the energy converges.

The most popular functional used to approximate the exchange-correlation functional is B3LYP. It is a hybrid of other types of functionals with their individual contributions balanced so that it gives the best possible result. In this work we use B3LYP (Kim and Jordan, 1994) for the identification of stable conformations of significant dihedral angles and B3PW91, which is another hybrid functional, for

further computations. Overview of commonly used functionals can be found in (Devlin, 2019)

DFT is not an *ab-initio* method *per se* because, in practise, a few empirical data are needed for the guess of the functional. So far there is no way of systematically improving the functional in order to yield better results. Nonetheless, the average cost of a DFT calculation is still extremely convenient in calculations of moderate accuracy for molecular systems of chemical complexity. (Magnasco, 2013)

#### 4.1.3 Basis sets

Basis sets are sets of functions used in HF and HK methods to yield the wavefunction or electron-density distribution, respectively. In quantum-chemistry computations the basis functions used are usually the atomic orbitals. Atomic orbitals can be Gaussian-type, Slater-type or numerical. The most commonly used are Gaussian-type orbitals. Basis sets used in this work are composed of Gaussian-type orbitals — the double and triple-zeta Pople basis sets 6-31+G\* and 6-311++G\*\*.

## 4.2 Spectral simulations

To compute spectra in a good agreement with the experiment, we need to simulate the molecule as realistically as possible. Given the nature of spectroscopic methods, where the specimen is often dissolved in a solvent in order to perform the measurement, it involves taking in the consideration its interaction with the solvent. After the most probable conformations of the molecule in the particular solvent are determined, the vibrational frequencies and intensities can be computed for each conformation separately giving their full spectra. The final spectra is obtained by their Boltzmann average.

### 4.2.1 Geometry optimization

Prior to the geometry optimization, it is necessary to find all possible conformers of the molecule by scanning over its torsion angles and finding the position in which the energy of the molecule is minimal. Subsequently, conformers with all possible combination of the found minima of torsion angles are compiled and the geometry optimisation is performed on each single one of them.

It is done so by an iterative algorithm which is designed to find the minima (which correspond to the stable form of the molecule) and maxima (which correspond to the

transition states) of the potential energy surface (PES) by changing the coordinates of the molecule.

The essence of all geometry optimization algorithms is the computation of the Newton-Raphson step towards the local minimum or maximum on the PES. It requires the computation of first and second derivatives of the energy; that is, the gradient vector  $\vec{g}$  and the Hessian matrix  $H$ , respectively. The Newton-Raphson step is then defined as  $\vec{h} = -H^{-1} \vec{g}$ . If all the elements of diagonalized Hessian are positive, i.e., the matrix is positively definite, the step taken will attempt to minimize the energy; if only one element is negative, the step will attempt to maximize the energy in that direction while minimizing it in all the others, heading toward a transition state. When the minimum on PES is reached, the gradient is equal to zero and the Hessian is positively definite.

Even though all quantities in ab-initio methods are computed and stored in the Cartesian coordinates, that is in Z-matrix, those are usually not the best choice for the geometry optimization algorithm itself because of their high level of coupling. Defining the molecule in a set of internal coordinates often results in the need of less optimization cycles, hence, a faster convergence of the used algorithm.

Nowadays, Cartesians are being replaced by the set of delocalized internal coordinates (that is linear combinations of bond lengths, valence angles and torsions; Baker, 1996), the generalized internal coordinates (Fogarasi, 1992), which are derived directly from the normal coordinates used in the theory of molecular vibration discussed in the section 2.3, or some other set of redundant internal coordinate system (Pulay and Fogarasi, 1992; Peng et al., 1996). All of them are readily derived from the Cartesian Z-matrix input during every optimization step. More details about geometry optimization algorithm can be found in (Schlegel, 2011 or Baker, 2017)

For the spectral simulation it is necessary to identify the minima of PES corresponding to the major stable conformers of the molecule and subsequently to include all of these conformers in the computation of spectra.

#### 4.2.2 Vibrational frequencies and intensities

After the conformational analysis is performed, the spectra, i.g., the vibrational frequencies and intensities of major stable conformers can be computed. It is important to perform this computation on the same level of theory as the geometry optimization.

Vibrational frequencies and intensities can be obtained from the mass-weighted Hessian matrix in Cartesian coordinates. The procedure involves following steps: 1) separating the translational and rotational motion by shifting the coordinate system into the centre of mass and projecting the Hessian into the rotational reference frame defined by the principal axes of inertia; 2) diagonalization of the projected matrix.

The eigenvalues of hereby obtained matrix give the force constants of normal modes which are easily converted to the frequencies (eq. 2.10) and wavenumbers (eq. 3.1). Its eigenvectors, after being mass-weighted and normalized, yield the normal modes.

Computation of intensities differs for each vibrational method. For IR and VCD spectroscopies it involves computation of dipole and rotatory strength (eq. 3.19). In case of ROA and Raman spectroscopies the corresponding invariants (eq. 3.20) are computed. Details about VOA spectral intensity calculation can be found e.g. in (Nafie, 2011).

The bandshape of experimental spectra is Lorentzian curve, hence, the final spectra are calculated by performing a convolution of the obtained intensities with Lorentzian function.

The presence of different conformers with different spectra is dealt with by computing the Boltzmann average of the spectra weighted by the calculated energies of the conformers.

#### 4.2.3 Solvent models

Incorporating the solvent in the model can be done in three ways: implicitly, explicitly, or by a combination of these two approaches. An overview of developed models along with their advantages and disadvantages can be found in (Skyner, 2015).

Implicit approach is less computationally demanding but does not take into account the local fluctuations of solvent density around the molecule. The solvent is modelled as homogeneously polarizable medium and the main parameter is the dielectric constant, i.e., the relative permittivity  $\epsilon$  of this medium. The solute is placed in a cavity with the correspondent charge distribution on its surface. The solvent surrounds the cavity and is being polarized by it.

Commonly used implicit model are the Polarizable Continuum Model (PCM) which is rather a family of models which treat the solute as a polarizable dielectric

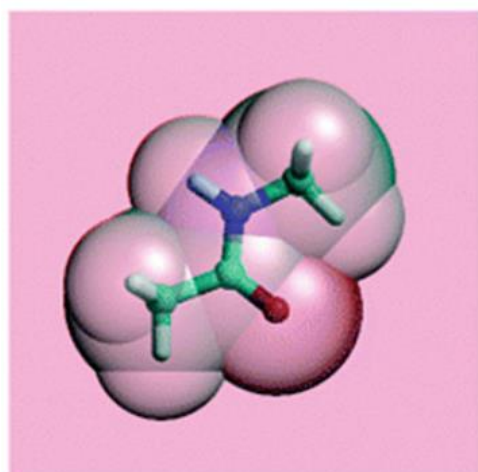


(Tomasi, 2005), Conductor-like Screening Model (COSMO), which considers  $\epsilon = \infty$  (Klamt and Schürmann, 1993) or Solvation Model Based on Density (SBD).

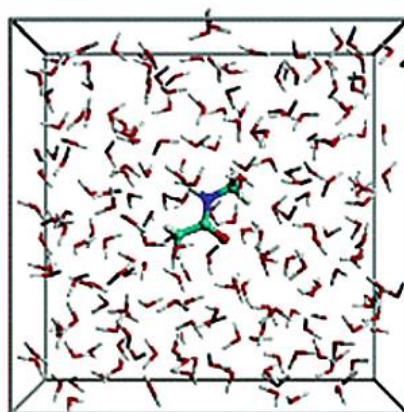
In this work a conductor-like PCM (C-PCM) version of PCM is used. It is a combination of COSMO and PCM where the dielectric permittivity is  $\epsilon = \infty$  which simplifies the computation. (Barone and Cossi, 1998). More details on continuum models are discussed in (Tomasi, 2007).

Explicit solvent models treat individually every molecule of the solvent. This allows to model direct solute-solvent interactions but, on the other hand, it leads to a higher computational cost. This models are usually used in molecular dynamics or Monte Carlo simulations. The difference between implicit and explicit solvent models is demonstrated in the Figure 4.1.

Hybrid models combine the two approaches with the aim to minimize the computational cost while preserving some of the spatial properties of the solute.



a) implicate solvent model



b) explicite solvent model

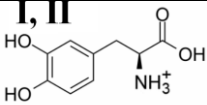
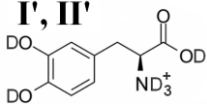
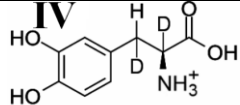
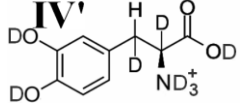
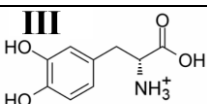
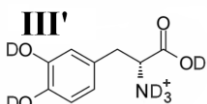
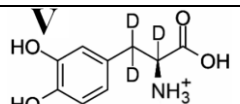
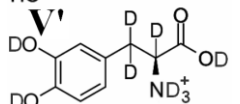
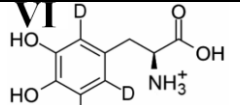
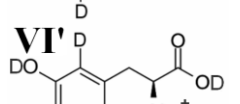
Figure 4.1: Different approaches of modelling a solute in a solvent: a) the continuum approach – the molecule is closed in a cavity with the approximation of molecules charge distribution on the surface which interacts with the dielectric continuum representing the solvent; b) the fully solvated system – the solute is placed in a box filled with solvent molecules which are all modelled individually. (Monard and Rivail, 2017, edited)

## 5 Experimental Details

### 5.1 Samples

DOPA samples are distributed in a form of white powder. In our work we used and studied six different DOPA samples of different origin: one non-deuterated sample, which is used as pharmaceutical secondary standard from Supelco: PHR1271 – Levodopa – L-DOPA – (I); two non-deuterated and one deuterated samples from Sigma-Aldrich: D9628 – 3,4-dihydroxy-L-phenylalanine – L-DOPA – (II), D9378 – 3,4-dihydroxy-D-phenylalanine – D-DOPA – (III), and 333786 – L-DOPA-(phenyl-d<sub>3</sub>) – 2',5',6'-D<sub>3</sub>-L-DOPA – (VI); and two differently deuterated isotopologues from Teva Pharmaceuticals CR: SD1076 –  $\alpha,\beta$ -D<sub>2</sub>-L-DOPA – (IV), SD1075 –  $\alpha,\beta,\beta$ -D<sub>3</sub>-L-DOPA – (V). Moreover we prepared six additional deuterated analogues samples by isotopic exchange of easily-exchangeable hydrogens (carboxyl, hydroxyl and amine groups) for deuterium– samples I' – VI'. Designations of the samples used through out this work is summarized in the Table 5.1:

Table 5.1: Available samples

PHR 1271 D9628 – L-DOPA	<b>I, II</b>  <b>I', II'</b> 	SD 1076 – $\alpha,\beta$ -D <sub>2</sub> -L-DOPA	<b>IV</b>  <b>IV'</b> 
D9378 – D-DOPA	<b>III</b>  <b>III'</b> 	SD 1075 – $\alpha,\beta,\beta$ -D <sub>3</sub> -L-DOPA	<b>V</b>  <b>V'</b> 
		333786 L-Dopa-(phenyl-d <sub>3</sub> ) – 2',5',6'-D <sub>3</sub> -L-DOPA	<b>VI</b>  <b>VI'</b> 

The two L-DOPA samples from Supelco and from Sigma-Aldrich gave identical spectra in all experiments, therefore, we summarize the results from both of them under designation L-DOPA, unless the distinction is required, in which case we refer to them as **I**(PHR 1271) and **II**(D9628), respectively.

## 5.2 Absorption methods

IR and VCD spectra were measured at the Institute of Physics at Charles University using commercial spectrometer ChiralIR-2X<sup>TM</sup> from BioTools.

### 5.2.1 ChiralIR-2X<sup>TM</sup>

ChiralIR-2X<sup>TM</sup> is a commercial spectrometer from company BioTools. It allows a simultaneous measurement of IR and VCD spectra in a mid-IR spectral range of 4000-400 cm<sup>-1</sup>. Spectrometer uses DualSource<sup>TM</sup> radiation source which significantly increases signal to noise ratio (Nafie et al. 2004) and two photoelastic modulators (PEM) patented as a DualPEM technology which provides significant reduction in artefacts and improvement in baseline stability. (Biotools, Inc.) Signal from the sample is collected by MCT (HgCdTe) detector which requires cooling by liquid nitrogen to reduce the noise. The sample holder is revolving; that allows sample rotation during the measurement which prevents the liquid samples from drying out and enables elimination of artefacts in the solid samples. Picture of the spectrometer is in the Figure 5.1.



Figure 5.1: Spectrometer ChiralIR-2X<sup>TM</sup> used for the measurement of VCD and IR spectra. (VCD, vibrational circular dichroism; IR, infrared)

### 5.2.1 Beta Cell

Liquid samples for IR and VCD measurements were prepared in a setup from International Crystal Laboratories (ICL). We used Beta Cell (Figure 5.2) with a 25×4 mm CaF<sub>2</sub> windows and either a 15 μm Teflon spacer from ILC or a 6 μm spacer made by Vladimír Kopecký Jr., Ph.D. at the Institute of Physics of Charles University from BoPET (biaxially oriented polyethylene terephthalate). This commercially manufactured polyester with high chemical stability can be found under different trademarks, e.g., Mylar, Melinex, or Hostaphan. (DeMueuse, 2011).



Figure 5.2: Beta Cell and a plastic cell holder from International Crystal Laboratories used for measurement on ChiralIR-2X

### 5.2.2 ChiralIR-2X<sup>TM</sup> measurement and data treatment

All liquid samples were measured in concentration 100 mg/ml in 1M HCl. Preparation of the sample was quite laborious compared to the other measuring techniques. First we put cleaned CaF<sub>2</sub> window in the back part of the Beta Cell with the Mylar spacer on it. We made sure that the spacer fits closely to the window. Next, we applied 6 μl of the sample and, as carefully as possible, put the second window on the spacer; this was the tricky part because most of the times some bubbles formed in the sample and we had to dismantle the whole thing and repeat the procedure. Presence of the bubbles could negatively affect the measurement due to the water vapours which form inside of them. If there were little to none bubbles, we finished the assembling of the cell by screwing its front part on and attached it to the plastic holder by a rubber band.

Setup of the spectrometer was fixed during the whole measurement: resolution  $4\text{ cm}^{-1}$ , 4000 scans per block, 2-PEM MODE, and Blackman Harris function for apodization. The only variable thing was the number of blocks measured for each sample which was determined either by available time for the measurement or by the speed of the sample's drying out. After every measured block a spectrum was obtained, meaning that every spectrum was composed from 4000 scans; measurement of each block took approximately one hour.

Raw IR and VCD spectra from each run (4 – 19 blocks) were averaged and the averaged data were treated by a background subtraction (signal of the Beta Cell filled with pure solvent) and polynomial baseline correction in GRAMS/AI™ 9.2. The data are presented as an absorption and its difference; the conversion to a molar extinction coefficient and its difference would be burdened by significant errors originated from the uncertainty of sample's thickness which was determined by the strength with which Beta Cell was tightened, therefore was different every time.

Measurement of the solid samples was relatively easy. A 7 mm KBr pallet with just a few micrograms of the sample (ratio KBr to sample was approximately 100:1) was prepared using Mini Pellet Press (Specac Ltd) with a 2 t pressure and measured with the same measurement setting as the liquid samples except of the rotation which was slower in this case – approximately 1 rotation every 10 seconds. The VCD signal from the solid sample was more intense than that from the liquid samples and generally 3 – 4 blocks of spectral acquisition were sufficient. The post-processing of the spectra was similar to the liquid samples.

### 5.3 Scattering methods

Raman spectra were measured at the Institute of Physics of Charles University using two different apparatus: Raman spectrometer SPEX and Raman confocal microscope Alpha300 RSA. SPEX allows only liquid sample measurement, whereas using the Raman microscope, we were able to measure solid state samples as well. ROA spectra were measured at the Department of Optics of Palacký University in Olomouc by Josef Kapitán, Ph.D. using his newly developed next generation ROA spectrometer.

### 5.3.1 Spectrometer SPEX

Spectrometer was built at the Division of Biomolecular Physics at the Institute of Physics. It uses a 90° geometry; that means that the scatter light is being collected under 90° angle with respect to the path of the incident laser beam. Four wavelengths can be used for the exciting radiation: 442, 488, 514, and 532 nm. Scattered light travels through an edge filter to the spectrograph SPEX 270M from Horiba company with focal length 270 mm. Spectrograph has two grids to choose from; one with 1200 (g1) and one with 1800 (g2) slits/cm. Light from the spectrograph is detected by CCD detector with a resolution 1340×100 pixels which requires cooling with liquid nitrogen.

### 5.3.2 Measurement using SPEX and data treatment

The setup of the spectrometer was same in all experiments. We used a 532 nm, Nd:YAG Verdi V2 laser of power of 400 or 1000 mW. Spectra were measured in the range from ~75 to 2300 cm<sup>-1</sup> using the g1 grating. Calibration was performed by neon lamp spectrum using the program Neocalpex2 developed by doc. Jiří Bok. Samples were measured in Hellma Micro-cuvette 101.015-QS, 3x3 mm, in approximately 80 µl volume.

Firstly, we used SPEX to test the solubility of L-DOPA in various solvents: Dimethyl sulfoxide (DMSO, (CH<sub>3</sub>)<sub>2</sub>SO), tetrafluoroethylene (TFE, C<sub>2</sub>F<sub>4</sub>), acetonitrile (CH<sub>3</sub>CN), chloroform (CH<sub>3</sub>Cl), and methanol (CH<sub>3</sub>OH). Each solution was prepared in a concentration of 100 mg/ml. We then lowered the concentration gradually up to 12.5 mg/ml and observed that L-DOPA did not completely dissolve in any of the solvents. Thus, we used centrifugation to let the undissolved solutes sediment and to make sure that we filled the cuvette only with eventual dissolved sample. Systematically the pure solvent for later background subtraction was measured every time prior to the sample and we used the same accumulation settings for both. Parameters of the measurements are shown in the Table 5.2.

Further we tested the solubility of the samples at neutral pH in distilled water (H<sub>2</sub>O) and heavy water (D<sub>2</sub>O) in concentration 1 mg/ml. Because the solutes did not dissolve completely, we used the centrifuge as in the previous case. Apart from the background spectra of pure H<sub>2</sub>O and D<sub>2</sub>O, we only measured the spectra for the

two different L-DOPA samples (PHR 1271 from Supelco and D9628 from Sigma-Aldrich). The parameters are shown in the Table 5.3.

Finally we prepared all samples in concentration of 100 mg/ml in 1M HCl and 1M DCl. Solutes easily dissolved in both solvents. We measured spectra of pure 1M HCl and DCl and of all solutions except of D-DOPA in DCl (due to the high fluorescence background arising from impurities present in the sample). Parameters of the measurement are shown in the Table 5.4.

Table 5.2: Parameters of the measurement of L-DOPA in different solvents

<b>Spectrometer SPEX; 532 nm; 400mW; 75-2300 cm<sup>-1</sup></b>			
<b>L-DOPA: c = 13 mg/ml</b>			
Solvent	Accumulation length	Number of accumulations	Total time
DMSO	0.2 s	1500	5 min
TFE	1.0 s	300	5 min
acetonitrile	0.5 s	600	5 min
chloroform	0.2 s	600	2 min
methanol	3.0 s	100	5 min

Table 5.3: Parameters of the measurement of L-DOPA in H<sub>2</sub>O and D<sub>2</sub>O

<b>Spectrometer SPEX</b>			
<b>532 nm; 400mW (H<sub>2</sub>O), 1000mW (D<sub>2</sub>O); 75-2300 cm<sup>-1</sup></b>			
<b>L-DOPA: c = 1 mg/ml</b>			
Sample	Accumulation length	Number of accumulations	Total time
H <sub>2</sub> O	5 s	24	2 min
<b>I</b> in H <sub>2</sub> O	10 s	120	20 min
<b>II</b> in H <sub>2</sub> O	10 s	120	20 min
D <sub>2</sub> O	5 s	24	2 min
<b>I</b> in H <sub>2</sub> O	10 s	120	20 min
<b>II</b> in H <sub>2</sub> O	10 s	120	20 min

Table 5.4: Parameters of the measurement of all samples in HCl and DCl Spectrometer SPEX; 532 nm; 400mW; 75-2300 cm<sup>-1</sup>  
all solutes: c = 100 mg/ml

Sample	Accumulation length	Number of accumulations	Total time
HCl	5 s	24	2 min
<b>I</b>	5 s	24	2 min
<b>II</b>	5 s	24	2 min
<b>III</b>	2 s	120	4 min
<b>VI</b>	5 s	24	2 min
<b>V</b>	5 s	24	2 min
<b>IV</b>	5 s	24	2 min
DCl	5 s	24	2 min
<b>I'</b>	5 s	24	2 min
<b>II'</b>	5 s	24	2 min
<b>VI'</b>	5 s	24	2 min
<b>V'</b>	5 s	24	2 min
<b>IV'</b>	5 s	24	2 min

Raw SPEX data were processed in GRAMS/AI™ 9.2. A subtraction of respective solvent signal and polynomial baseline correction was performed in all spectra and they were normalized by integral intensity in the region from 300 to 1800 cm<sup>-1</sup>.

### 5.3.3 Raman confocal microscope Alpha300 RSA

The Raman confocal microscope Alpha300 RSA from WITec Company is combined with atomic force microscopy (AFM) and scanning near-field optical microscopy (SNOM). It is equipped with excitation wavelengths 442, 532, 633, 785 and 830 nm. It is primarily suited for the imaging of cells and tissues and for nanoscale surface characterization. In Raman general operation modes it acquires a complete Raman spectra at every pixel of the image. It uses an ultra-high throughput spectrometer (UHTS) with focal length of 30 cm and grating 600 g/mm, which ensures of high quality spectra even with a low acquisition time and a low light intensity. The light is captured by Newton CCD detector DU970-BVF with resolution of 1600 × 200 pixels in 16 × 16 μm. Acquisition time used for the measurements was relatively short (0.10172 s) to prevent sample degradation.

Microscope software interface is WITec Suit FOUR package which includes Control FOUR for measurement control and data acquisition, and Project FOUR for image and spectra post-processing. It enables the user to select the part of the sample which is going to be scanned (marked with red rectangle in the Figure 5.3)



and, after the spectra is acquired for every pixel, the user can choose the pixels of the image for the compilation of the final spectrum using filters based on selected spectral lines (Figure 5.4). Final spectrum is then created by averaging the spectra from the selected pixels and treated with the “CRR+Smooth” function for the removal of cosmic-rays spikes and smoothing.



Figure 5.3: In WITec software Control FOUR, the user can select the desirable part of the image for scanning, that is marked by the red rectangle

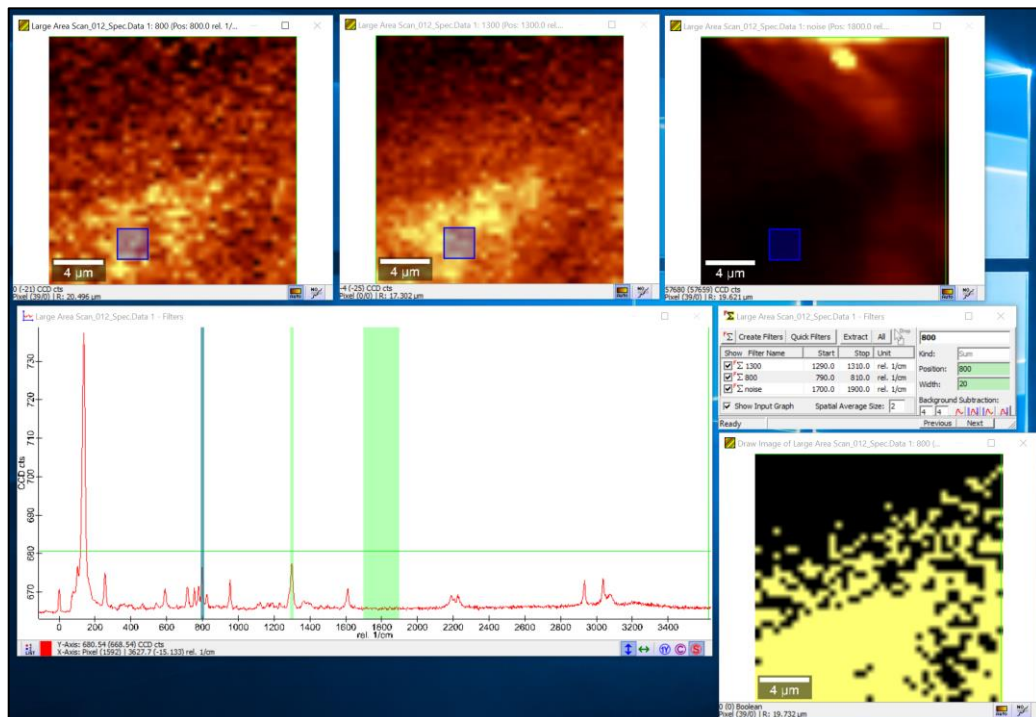


Figure 5.4: WITec software Project FOUR used for spectral post-processing. The window with spectrum shows the selected spectral ranges (blue and green bands), the three windows on the top show the presence of particular characteristics in the scan and the window in the bottom right corner shows the pixels from which the final spectrum going to be composed.

#### 5.3.4 Sample preparation and measurement using Alpha300 RSA

All samples were measured in solid phase, in liquid phase as 100 mg/ml solutes in 1M HCl, and using the drop-coating deposition Raman (DCDR) method with 1 mg/ml solute in H<sub>2</sub>O and 0.5 mg/ml solutes in 1M HCl. For the measurements a 532 nm laser was chosen with power of 9mW for the solid samples and DCDR method and 40 mW for the liquid samples, together with Carl Zeiss 50×/0.55 LD objective.

Preparation of the solid samples was not laborious; we simply spread some of the powder on the microscope slide and chose a section of the image which was convenient for spectra acquisition. Ideally we tried to find a crystal that was big enough and that was easy to focus on. An example of that is shown in the Figure 5.5. Scan width and height were fixed during all measurements, 20×20 μm, with resolution of 40×40, that is, 4 scans/μm<sup>2</sup>.

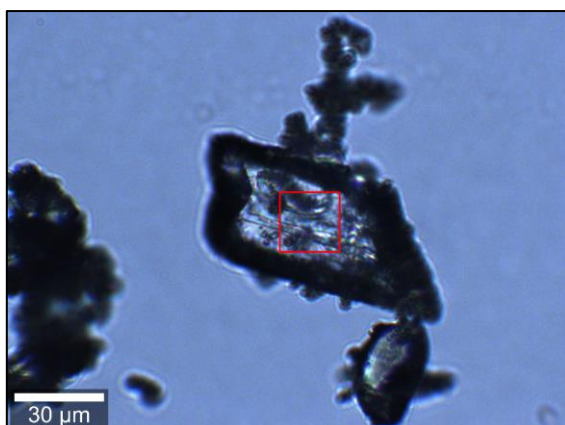


Figure 5.5: Sample in a solid phase in Alpha300. PHR 1271 crystal selected for scanning.

In liquid samples measurements 6 μl droplets were put to the microscope slit using micropipette. Scan width and height were fixed during all measurements, 20×20 μm, with resolution of 60×60, that is, 9 scans/μm<sup>2</sup>. Because the liquid samples were homogenous, there was no need to search for a convenient region for the measurement. We just had to make sure that the focus was somewhere in the sample droplet, neither under it nor above it.

Drop-coating deposition Raman (DCDR) is a spectroscopic technique which enables measurement of low-concentration solutions. Its core is a special sample preparation when a microdroplet of the solution is applied to a hydrophobic plate and left to dry. When the droplet evaporates, the solute gets concentrated on the edges and

forms a ring of a high concentration (Figure 5.6). The idea is that the molecules will stay in their solute-like conformation, not forming crystals, hence the DCDR spectra will resemble the spectra of a saturated solute of the molecule. (Zhang et al., 2003; Filik and Stone, 2007).

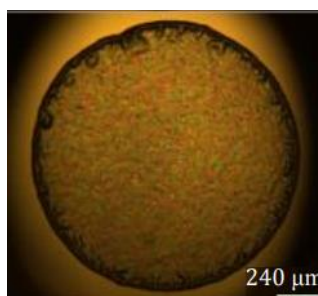


Figure 5.6: Demonstration of a DCDR sample. Typical “coffee-ring” of high sample concentration on the circumference is formed by dried microdroplet. Adopted from (Kuižová, 2019).

For DCDR measurement we dissolved all samples in H<sub>2</sub>O in concentration 0.5 mg/ml and in HCl in concentration 1 mg/ml. We applied 2 μl of each solution to Teflon-coated plate made of stainless steel from Tienta Sciences (surface SpectRIM™ Slide) and let it dry for several days.

Compared to the solid and liquid samples, it was more difficult to find an appropriate spot for spectra acquisition in some of the dried droplets. Eventually, we managed to do so in all of them except the PHR1271 in HCl. The samples, being low-molecular species, did not tend to form nicely resolved “coffee rings” as anticipated, but a sort of semi-crystallized bulge. An example of an image of DCDR sample is in the Figure 5.7. Because almost each sample looked differently, it was necessary to adjust scanned area for every single measurement. Parameters of the scanned area for every sample are in the Table 5.5.

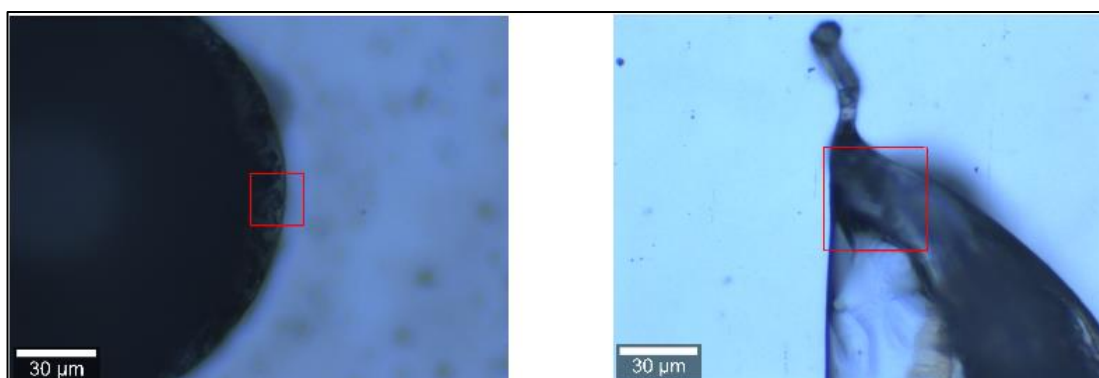


Figure 5.7: DCDR sample of 2',5',6'-D3-L-DOPA in HCl (left) and H<sub>2</sub>O (right). (DCDR, drop-coating deposition Raman)

Table 5.5: Parameters of the scanned area for DCDR samples.

sample	c=100 mg/ml in 1M HCl		c=1 mg/ml in H <sub>2</sub> O	
	Scan scale (width×height μm)	Resolution (scans/μm <sup>2</sup> )	Scan scale (width×height)	Resolution (scans/μm <sup>2</sup> )
<b>I</b>	20×25	4	30×40	4
<b>II</b>	–	–	30×40	4
<b>III</b>	40×40	1	30×40	4
<b>VI</b>	40×40	4	40×40	2
<b>V</b>	20×20	5	30×40	4
<b>IV</b>	15×15	9	40×40	4

Raw data were firstly treated in the WITec software Project FOUR as described above in the section 5.3.3 and then exported to GRAMS/AI™ where, if needed, the baseline correction was performed and the spectra were normalized by the integral intensity from 300 to 1800 cm<sup>-1</sup>.

### 5.3.5 ROA spectrometer

Recently developed next-generation ROA spectrometer was assembled by Josef Kapitán, Ph.D. at the Department of Optics of Palacký University in Olomouc. It is to some extent similar to the commercial ROA spectrometers from Biotools. It is based on the principle described by W. Hug (Hug and Hangartner, 1999) and uses a system of rotating half-wave plates for the reduction of artefacts of the measurement. Spectrograph allows simultaneous measurement in the whole range of fundamental molecular vibrations ranging from approx. 50 to 4000 cm<sup>-1</sup>. Excitation wavelength is 532 nm. Measurements can be performed in any of all four possible modulation schemes of ROA experiment (see Figure 3.9 in the chapter 3.3.3). Thanks to the high-quality components and its overall compilation, this spectrometer overcomes attributes of the commercially sold spectrometers.

### 5.3.6 Sample preparation and measurement using ROA spectrometer

Spectra were measured in the SCP (scattered circular polarisation) arrangement using back-scattering geometry. All six samples were dissolved in 1M HCl in concentration 100 mg/ml and used for measurements without further treatment. About 80 μl of each solution were put into narrow wall 3x4 mm microcuvettes (Starna Scientific Ltd). The total acquisition time was around 30 hours for each sample. Raw

spectra were calibrated using neon lamp spectrum and intensity corrected using spectral calibrated tungsten bulb (secondary standard). Further, we subtracted solvent signal using Grams AI software and corrected baseline by polynomial splines.

#### 5.4 Parameters of spectral simulation

All computations were performed using the Gaussian 09 software (Frisch et al., 2009) by the DFT method on B3LYP or B3PW91 level of theory. We used the 6-31+G\* basis set for 1D energy scans, G-316 for 2D scans, and 6-311++G\*\* for 2D scans, geometry optimization, and for the vibrational frequency calculations. In all cases we used water as an implicit solvent. Simulated spectral profiles were generated by convolution of calculated intensities with the Gaussian profile (FWHM=10) at 298 K.

## 6 Results and discussion

### 6.1 Solubility

#### 6.1.1 Solubility based on pH

Based on the predictions from Chemicalize software, L-DOPA should exist in different charged states depending on pH (Figure 1.8). Different ionic forms of the molecule should give different vibrational spectra. The goal was to determine if it would be possible to prepare the samples at sufficient concentration for measurements of vibrational spectra of differently protonated L-DOPA forms.

The neutral (zwitterionic) form of L-DOPA has a very low solubility, just like its related amino acid tyrosine. At pH  $\sim 6$  we tried to prepare a 1 mg/ml solution in deionized H<sub>2</sub>O. However, even such low concentration could not be achieved; there still was a substantial amount of undissolved DOPA powder floating in the solution. Therefore, we used the centrifuge to separate the crystal form of L-DOPA from the potentially dissolved one and extract only the supernate for the measurement.

Due to the very low pK<sub>a</sub> of carboxylic group (1.65), the protonated form of L-DOPA has to be measured at pH lower than unity. The maximum solubility is strongly correlated with the acidity of used solvent (HCl of various molarity) as evidenced in Table 6.1. In 1M HCl the sample dissolved completely within a few seconds to the final concentration of 100 mg/ml. Acidic L-DOPA solutions showed a long-term stability, enabling even time-consuming ROA measurements.

Table 6.1: solubility of L-DOPA in various pH

HCl molarity	L-DOPA concentration(mg/ml)	pH
1	100.0	<0.4
0.5	74.0	0.72
0.25	28.9	0.91
0.1	10.5	1.15

To test the solubility in a basic medium, we first prepared a suspension of 13.8 mg of L-DOPA (**I**) in 138  $\mu$ l of distilled H<sub>2</sub>O which we then gradually diluted by 2.5 M NaOH solution and observed if L-DOPA dissolved with an increasing concentration. After first 5  $\mu$ l of NaOH was added to the suspension, the white undissolved crystals of L-DOPA changed colour to a light brown indicating an oxidation of L-DOPA which, however, remained undissolved. We added up to 1.05

ml NaOH to the suspension but we observed no significant change in solubility. The sedimented undissolved crystals of L-DOPA turned even darker brown and the solution turned light brown indicating that a little amount of L-DOPA dissolved. Potentially, it would be possible to dissolve L-DOPA in degassed water in a protective atmosphere to prevent the oxidation. Nevertheless, the following spectroscopic measurements would also have to be performed in the protective atmosphere which would be very complicated. Moreover, in basic pH there are three ionisable functional groups (hydroxyl groups and amino group) which increase the number of differently charged L-DOPA forms present in the solution at basic pH and would complicate further analysis.

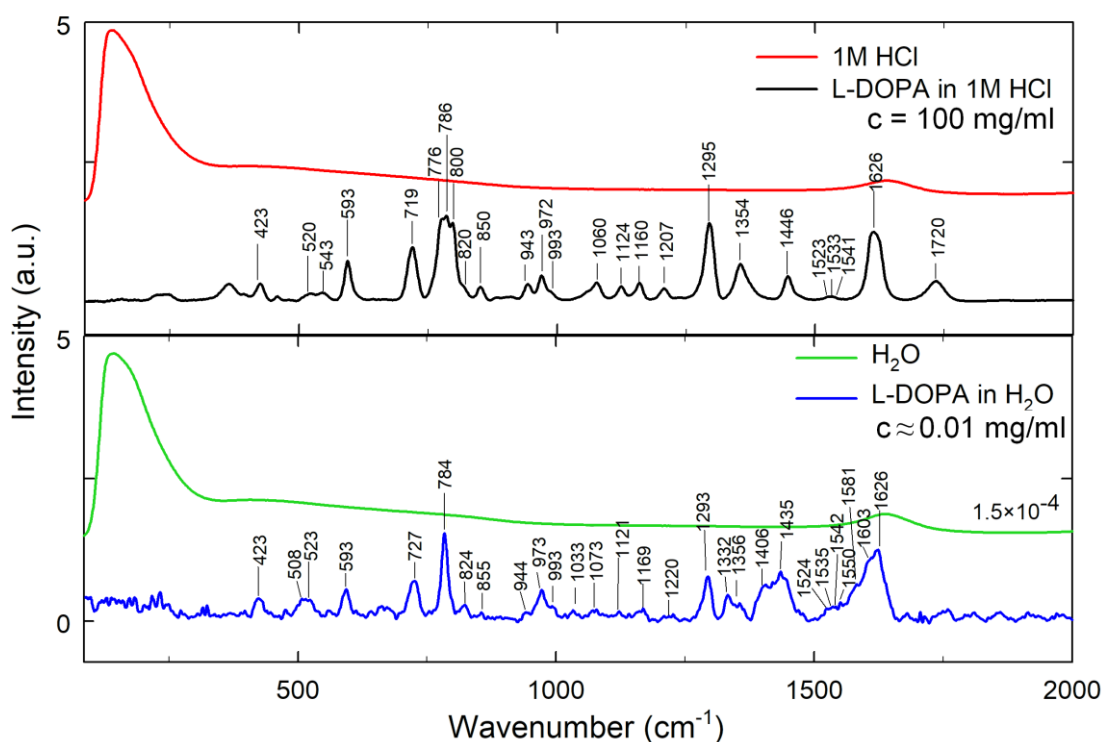


Figure 6.1: Comparison of L-DOPA Raman spectra in acidic and neutral pH.

The final Raman spectra for neutral (zwitterionic) and acidic (cationic) form of L-DOPA (**I**) in aqueous solution are shown in the Figure 6.1, lower and upper panel, respectively. The concentration of L-DOPA in 1M HCl was 100 mg/ml. Thanks to the fact that HCl is a strong acid and, therefore, it dissociates completely in aqueous solution, Raman spectrum of 1M HCl appears to be similar to those of pure deionized water. In acidic medium L-DOPA dissolves easily and the intensity of its spectra is comparable with that of the pure solvent, however in neutral pH it barely dissolves and the intensity of its spectra is approximately thousand times lower than that of the pure

solvent. Based on that we estimate that the concentration of L-DOPA in H<sub>2</sub>O was approximately 0.01mg/ml. Still we were able to obtain nicely resolved spectrum with ~ 30 resolved spectral bands (identified using the second derivative of the spectrum). Total acquisition time of L-DOPA spectra was 2 minutes in acidic medium and 20 minutes in pH-neutral medium.

Due to the relatively low signal to noise ratio of L-DOPA spectrum in neutral pH, it is not possible to fully qualitatively compare it to the spectrum in acidic pH. Overall spectral shape of both L-DOPA forms appears to be similar. In the lower spectral region it seems that peak at 786 cm<sup>-1</sup> in 1M HCl is actually composed of three whereas corresponding peak in H<sub>2</sub>O at 784 cm<sup>-1</sup> is a singlet. On the other hand, in the higher spectral region the three peaks in HCl, 1354, 1446 and 1626 cm<sup>-1</sup>, seem to have split up each into more peaks. However, in the region above 1560 cm<sup>-1</sup> there is a residual water signal left in the L-DOPA spectrum in H<sub>2</sub>O which makes it difficult to distinguish individual peaks. Some of the peaks seem to be shifted in the order of units of cm<sup>-1</sup> but this could be credited to the difficulty of distinguishing the exact position of the peaks thanks to the low intensity. The only significant shift is that of the peak at 719 cm<sup>-1</sup> in 1M HCl which in H<sub>2</sub>O changed its position to 727 cm<sup>-1</sup>. The more detailed vibrational analysis will be shown in the section 6.6.3.

### 6.1.2 Solubility in various solvents

It became clear already before that L-DOPA is soluble in a strong acidic medium which allowed for relatively fast spectral acquisition in the order of minutes. However, the zwitterionic form is almost insoluble. We wondered if it was possible to use other solvents for measuring the spectrum L-DOPA at neutral pH.

Therefore, we tried to prepare solution of L-DOPA of 100 mg/ml concentration in five different organic solvents. Unfortunately, L-DOPA did not dissolve in any of them so we lowered the concentration by gradually increasing the volume of the solvents. A partial dissolution was visible only when the concentration of 12.5 mg/ml was reached. Nevertheless, the real concentration of dissolved L-DOPA was much lower. Results are summarized in the Table 6.2.



Table 6.2: Testing of L-DOPA solubility in different solvents.

solvent	concentration (mg/ml)			
	100	50	25	12.5
DMSO	×	×	×	partially
TFE	×	×	×	partially
acetonitrile	×	×	×	minimally
chloroform	×	×	×	minimally
methanol	×	×	×	minimally

× means that dissolution was not visible, “partially” marks the situations where only partial dissolution was observable. DMSO, dimethyl sulfoxide; TFE, tetrafluoroethylene

Samples were centrifuged and supernates were used for Raman spectra measurements. The background subtraction and baseline correction was performed in all acquired spectra. The solute’s signal intensity was in most cases very close to the resolution limit and, moreover, most of the solvent’s Raman spectra were generally more than thousand times stronger than spectra of the solute and overlapped with it strongly; this made it impossible to perform the subtraction without any solvent residua. We could improve the quality of spectra by increasing the acquisition time or the number of acquisitions but our goal was to explore if in some of these solvents the acquisition of L-DOPA spectra could be performed as fast and easily as in HCl. We concluded that all of the used solvents failed to meet this condition.

Considering the above said nature of resulting spectra, we demonstrate only those of TFE and DMSO solutions because in other solvents the signal of L-DOPA was not distinguishable. Spectra are shown in the Figure 6.2. It presents the spectrum of L-DOPA in TFE and DMSO with total acquisition time of 5 minutes after the background subtraction and baseline correction and spectra of the pure solvents. The parts of L-DOPA spectra with high residual solvent signals were omitted. In both cases the significant residual solvent signal is present. The signal of L-DOPA in DMSO exhibits higher signal to noise ratio, based on that we conclude that L-DOPA dissolves better in it this solvent.

The comparison of L-DOPA (**I**) obtained in TFE and DMSO with that measured in water is shown in Figure 6.3. We have identified 14 peaks in H<sub>2</sub>O which are observable at least in one of the other solvents; 5 of them are observable in both (508, 784, 824, 1293, and 1626 cm<sup>-1</sup>), 6 are observable only in DMSO (423, 593, 855, 1169, 1524, and 1581 cm<sup>-1</sup>), and 2 only in TFE (729 and 1332 cm<sup>-1</sup>).

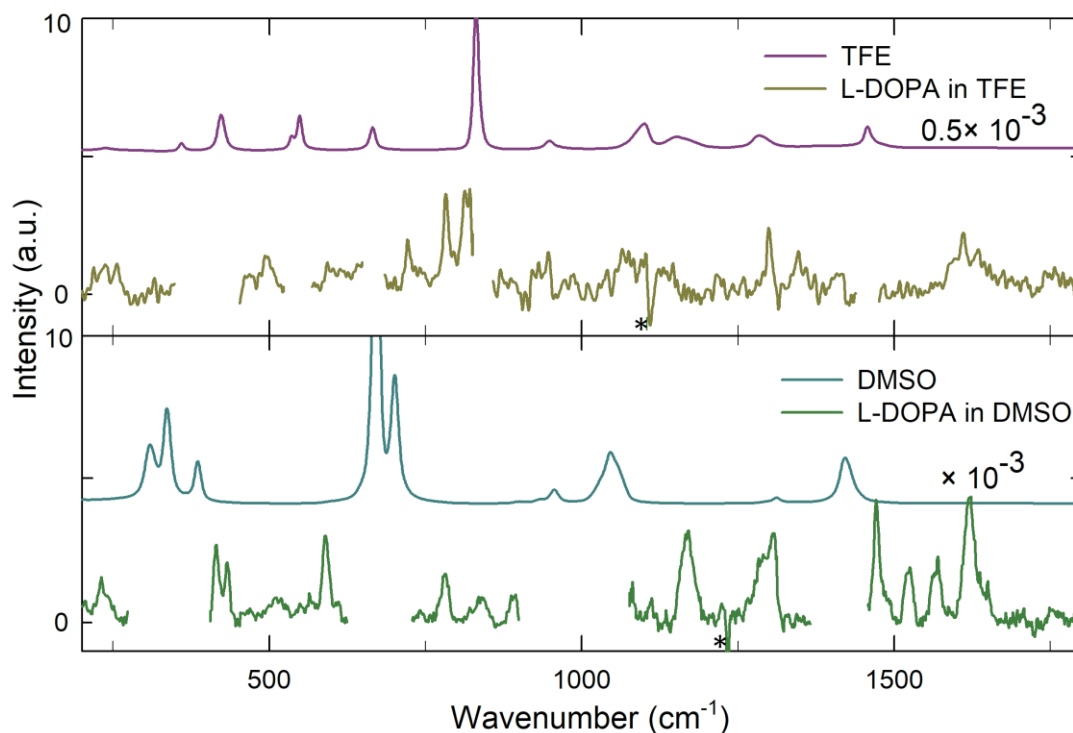


Figure 6.2: Raman spectra of L-DOPA in tetrafluoroethylene (TFE) and dimethyl sulfoxide (DMSO) compared to the spectra of pure solvents. Parts of the spectra with strong residual signal of the solvents are left out. Asterisk (\*) marks the artefacts caused by the background subtraction.

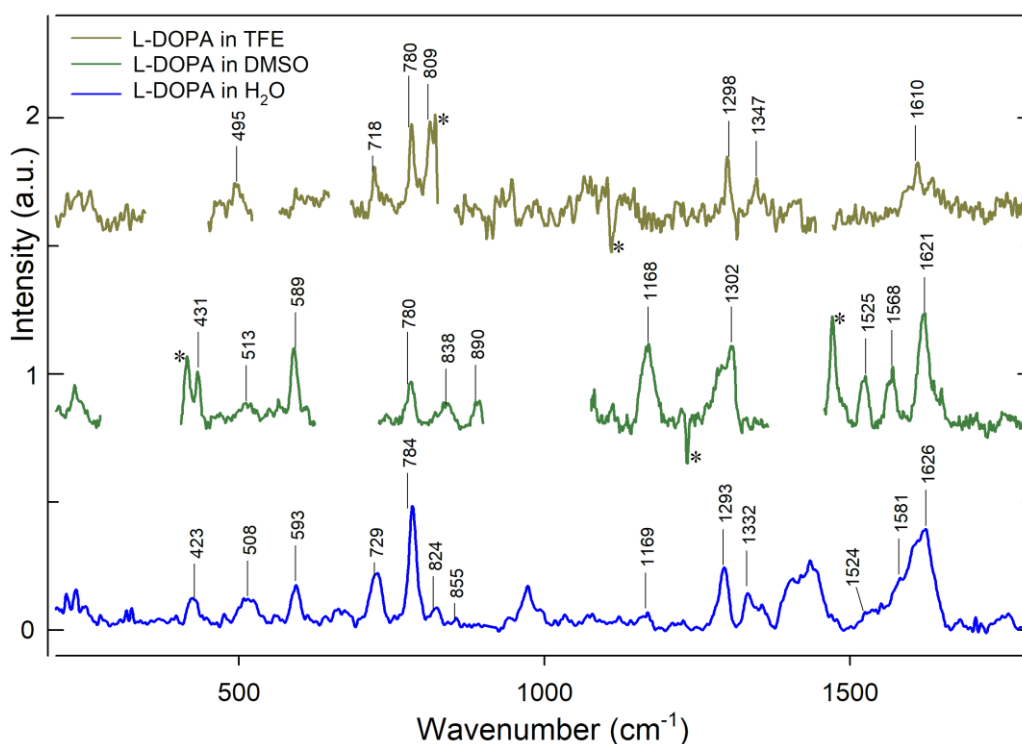


Figure 6.3: Comparison of L-DOPA (I) Raman spectra measured in different solvents. Asterisk (\*) marks the artefacts caused by the background subtraction or other experimental artefacts.

To sum up, L-DOPA dissolves very poorly in basic and neutral pH. Moreover, in the basic pH it oxidizes, so there is no point in measuring the spectra. We managed to obtain (with some difficulties) Raman spectrum of zwitterionic form in H<sub>2</sub>O which was approx. 10<sup>-4</sup> times less intensive than that in HCl. Based on that we estimate that the solubility in H<sub>2</sub>O is also approx. 10<sup>-3</sup> lower than in 1M HCl (≈0.01 mg/ml) which is too low for any VOA measurements. L-DOPA dissolved poorly or not at all in 5 different pH neutral solvents. Cationic form of L-DOPA was found to be easily soluble in concentrations enabling further ROA and VCD measurements (100 mg/ml in 1M HCl, 70 mg/ml in 0.5M HCl).

## 6.2 Raman spectra of different phases

In this section we present the Raman spectra of samples **I** - **VI** measured in different phases by different spectrometers. We compare (i) the measurements in a liquid state in acidic medium (1M HCl) from SPEX and Alpha 300, (ii) the spectra of crystal phase, liquid phase and “dried” state (DCDR technique) from Alpha 300, and (iii) the differences between DCDR spectra of neutral (zwitterionic, neat aqueous solvent) and cationic (1M HCl aqueous solvent) form of various samples. Spectra of the non-deuterated samples are presented in the Figure 6.4 and spectra of the differently deuterated samples in the Figure 6.5. Upon deuteration, new peaks of C-D vibrations appear around 2300 cm<sup>-1</sup> making the spectra of deuterated samples easily distinguishable. The resulting spectra are normalized based on integral intensity of 300 to 1800 cm<sup>-1</sup> spectral interval and they are shown from 300 cm<sup>-1</sup> because at a lower frequency-shifts the signal from Rayleigh scattering is still dominant.

Our first goal was to qualitatively compare liquid phase spectra measured by SPEX and Alpha 300 instruments (purple and blue lines in the Figure 6.4 and Figure 6.5). The main difference between SPEX and Alpha 300 is that the first spectrometer (equipped with g1 grating – 1200 slits/cm) acquires the spectra in the region from approximately 70 to 2400 cm<sup>-1</sup>; thus, it does not include the C-H stretching vibrations which occur around 3000 cm<sup>-1</sup>. (Their recording would require to reverse the grating and to stitch together the recorded spectra.) Spectra from Alpha 300 reach from 0 up to 3600 cm<sup>-1</sup>, hence, they cover the whole vibrational spectral range. Another difference is that the signal to noise ratios of resulting SPEX spectra are higher than those of spectra acquired with Alpha 300, thanks to the larger volume of the sample in laser focus. This becomes evident mainly in the cases of liquid D-DOPA (**III**, see

Figure 6.4 lower panel) and  $\alpha,\beta,\beta$ -D3-L-DOPA (V, see Figure 6.5 middle panel) spectra. These samples were contaminated by an impurity which, particularly when dissolved, showed a strong fluorescence with which was easier to cope with in the post-processing of the spectra from SPEX. Also spectra from SPEX manifested a slightly better spectral resolution enabling the distinguishing of delicate spectral features (small bands and shoulders; see e.g. Figure 6.5 lower panel around  $800\text{ cm}^{-1}$ , marked by arrows). Apart from these fine differences, the resulting spectra of liquid samples from both spectrometers are qualitatively identical.

The second goal was to determine the differences among spectra from crystal, dried and liquid phase (blue, lime, and maroon lines in the Figure 6.4 and 6.5). The main difference is that the peaks of the liquid-state spectra are generally wider and, moreover, those peaks which are close to each other in the crystal-state tend to merge and became undistinguishable. This happens because the positions of the atoms in a crystal are better defined than in a soluted state and, as a result, so are the frequencies of their vibrations. This is clearly observable in the area around  $750\text{ cm}^{-1}$ . Another notable difference in the liquid spectra is an appearance of a peak around  $1750\text{ cm}^{-1}$  corresponding to the COOH group vibration, which is not present in the spectra of crystalline phase in which L-DOPA remains in its zwitterionic form. (Mostad et al., 1971)

The third goal was to determine the applicability of DCDR (drop-coating deposition Raman scattering) technique to the measurements of differently charged DOPA samples (lime and orange lines in Figure 6.4 and Figure 6.5). This was motivated by the effort to enable simple measurement of DOPA samples in neutral (zwitterionic) form. In DCDR the spectra recorded from a “coffee ring”, which represents the desired dried state of the sample, usually resemble the spectra obtained from liquid phase at much higher concentration. However, our observations were (with a few exceptions) different. DOPA samples did not form the desired pattern during the drying-out process (compare Figure 5.6 and Figure 5.7). All of them tended to form semi-crystallized bulges probably due to their low-molecular nature. This tendency was even more pronounced for the samples in acidic solvent. In most cases the recorded DCDR spectra looked like a superposition of the crystal and liquid-phase spectra with a prevailing solid phase component; this was nicely evidenced by the shape of the signal in the C–H stretching region (around  $3000\text{ cm}^{-1}$ ). The only

exception was DCDR spectra of 2',5',6'-D3-L-DOPA in H<sub>2</sub>O which possessed characteristics of liquid-phase Raman spectra.

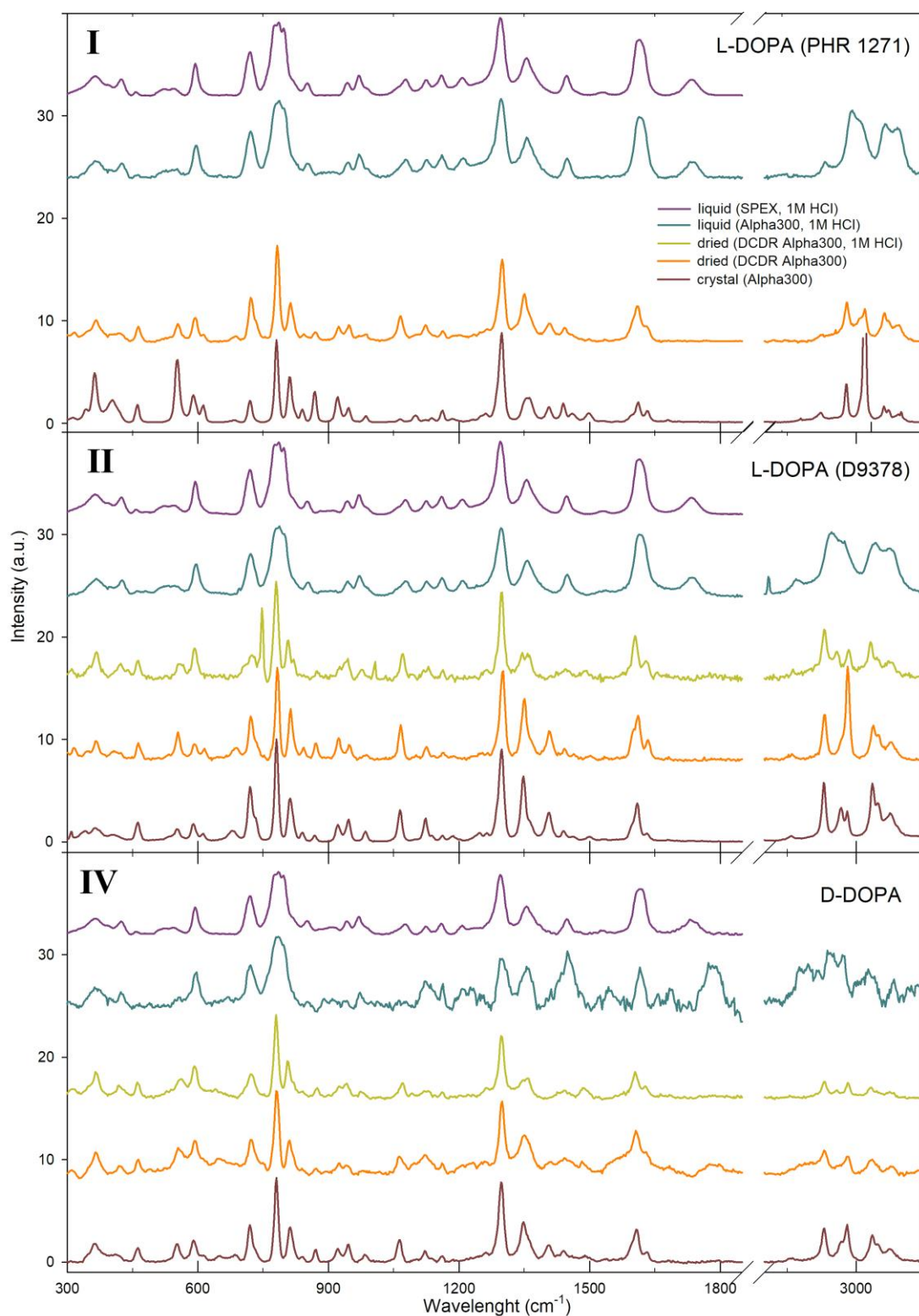


Figure 6.4: Raman spectra of three non-deuterated DOPA samples as measured by different spectrometers: SPEX and Raman microscope Alpha 300.

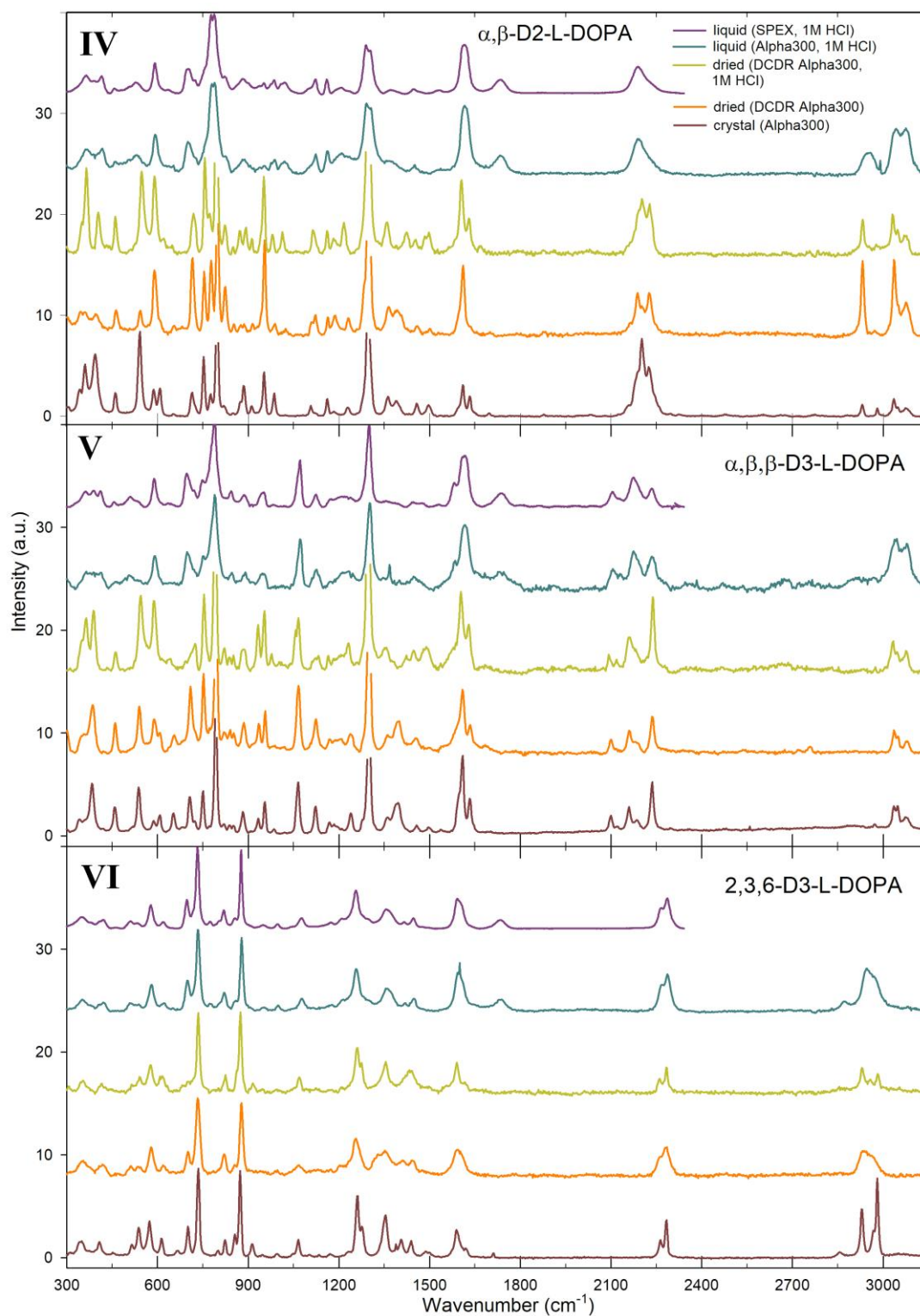


Figure 6.5: Raman spectra of three differently deuterated DOPA samples as measured by different spectrometers: SPEX and Raman microscope Alpha 300.

In general, the DCDR technique was not found particularly beneficial for the study of DOPA samples due to their problematic drying out. However, for 2',5',6'-D3-L-DOPA (**VI**) in H<sub>2</sub>O we obtained a fine quality DCDR spectrum which allowed identification of differences between spectra of differently charged forms (see Figure 6.6). It is evident that spectra of the zwitterionic and cationic form of (**VI**) are quite similar. The most noticeable differences are (i) the appearance of the 1733 cm<sup>-1</sup> peak in the spectrum of cationic form of L-DOPA (top blue line) corresponding to the COOH group vibration and (ii) the change of the relative intensity of the bands between 1320 – 1450 cm<sup>-1</sup> where C–O–H bending vibrations occur. Further, there are peaks of low intensity at 775, 950, and 2873 cm<sup>-1</sup> in the spectrum of cationic (**VI**) which cannot be observed in the zwitterionic form.

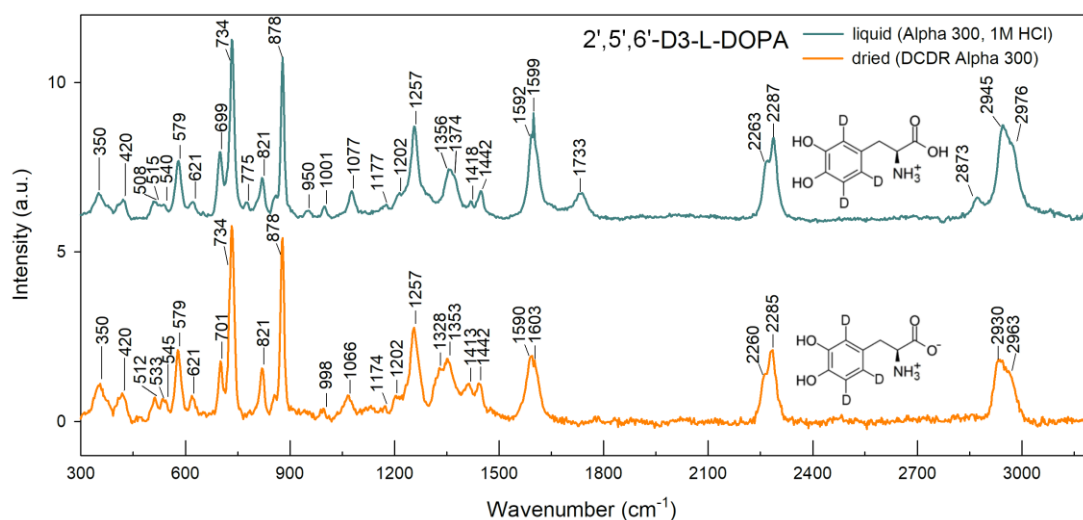


Figure 6.6: Comparison of the Raman spectra of 2',5',6'-D3-L-DOPA in acidic medium (top line) and pH neutral medium (bottom line).

In conclusion, on one hand, spectra from SPEX show a greater signal to noise ratio than spectra from Alpha 300, but on the other hand, they do not cover as big spectral range. Nevertheless, in the region covered by both spectrometers, the spectra are quantitatively similar. Spectra of the liquid samples differ mainly in the width of the bands which is greater than in the case of the liquid spectra thanks to the merging of the peaks which are close together, and in the appearance of a few new peaks around 1750 cm<sup>-1</sup> related to the COOH vibrations. DCDR technique has been found not suitable for the study of DOPA molecule because the samples did not dried out in a proper “coffee ring” shape but rather recrystallized thanks to their low molecular

weight. However, the spectra of cationic and zwitterionic forms of DOPA samples appear to be rather similar, as evidenced on the example of (VI) in the Figure 6.6.

### 6.3 Comparison of different non-deuterated DOPA samples

In this section we compare the non-chiral spectral properties of three different non-deuterated samples of DOPA (**I**, **II**, and **III**) with the intention to verify in which cases it is possible to interchange their spectra. In the Figure 6.7 we present the comparison of Raman and IR spectra of crystal phase and in the Figure 6.8 the comparison of Raman and IR spectra of liquid phase of DOPA.

The Raman spectra of crystalline samples (Figure 6.7) slightly differ from each other. Each spectrum is quantitatively unique in the region of C–H vibrations (around  $3000\text{ cm}^{-1}$ ), however, qualitatively the spectra of (**I**) and (**II**) are similar. On the other hand, the doublet which is present in the spectra of (**I**) and (**III**) around  $2990\text{ cm}^{-1}$  seems to merge in the spectrum of (**II**) into one peak. In the fingerprint region all three spectra are quantitatively similar; all the peaks are present in each spectrum, they only differ in their intensities. However, in the IR spectra, measured on ChiralIR-2X spectrometer, no differences are apparent. One possibility is to assign the variations in the crystal spectra to a slightly different crystalline structure of each sample caused by a different procedure of preparation, which is further confirmed by the fact that upon dissolution the differences disappear. In that case we would expect the IR spectra of crystal state to differ as well. They, however, do not. That is why we assume that the difference is caused by the low acquisition time of the spectra.

Both, Raman and IR spectra of the liquid samples (Figure 6.8) are quantitatively and qualitatively similar, virtually identical.

In conclusion, Raman spectra of the two non-deuterated L-DOPA samples (**I** and **II**) and the non-deuterated D-DOPA sample (**III**) differ only in the crystalline form. IR spectra of these samples are identical. Raman and IR spectra of the three liquid-state samples are also identical, therefore, it is safe to use only one of them as a representative of non-deuterated L-DOPA for the non-chiral measurement of liquid samples.



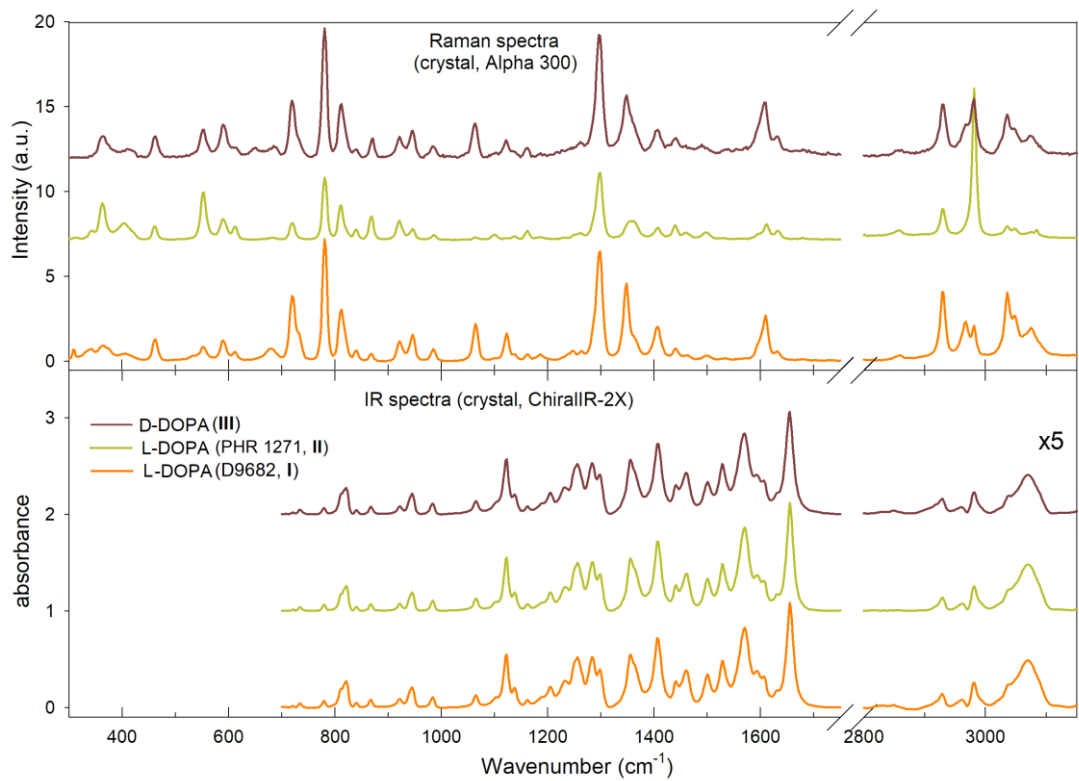


Figure 6.7: Crystal-phase Raman and IR spectra of three non-deuterated samples

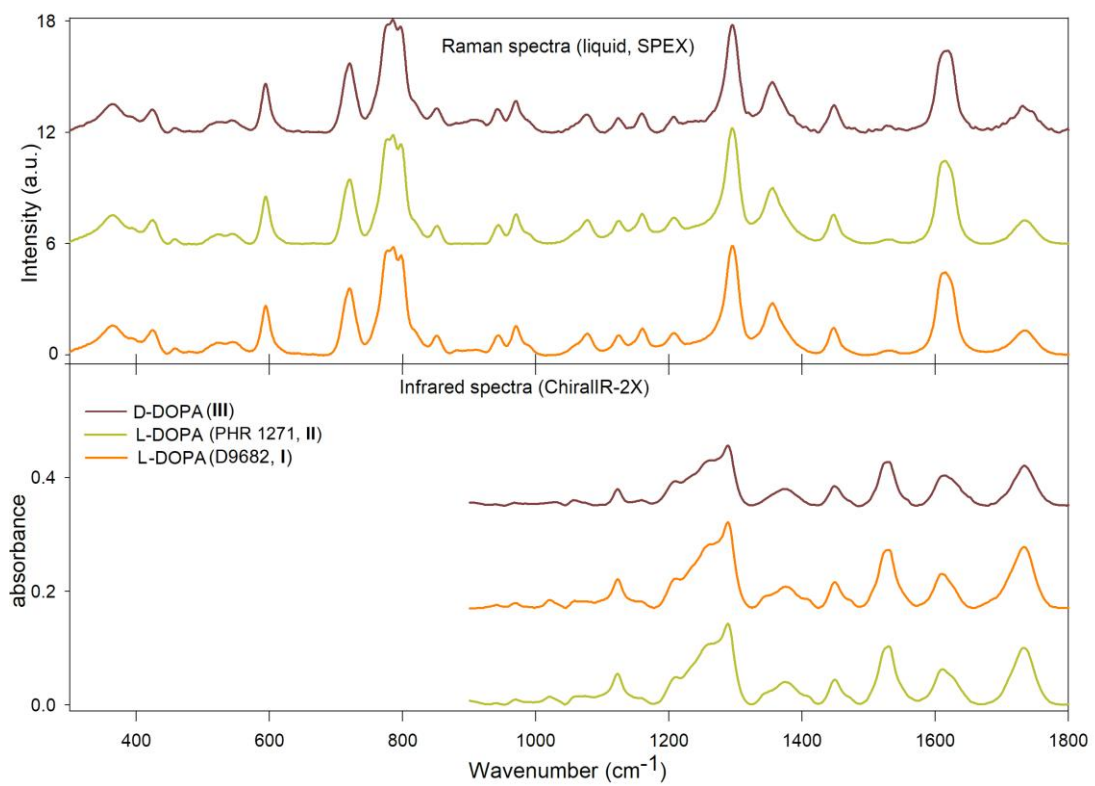


Figure 6.8: Liquid-phase Raman and IR spectra of three non-deuterated samples

## 6.4 Comparison of Raman and IR spectra of differently deuterated samples

In this section we compare Raman and IR spectra of the samples dissolved in 1M HCl to those dissolved in 1M DCl. In 1M DCl solution a relatively fast exchange is happening between the hydrogen and deuterium atoms on the “soft” positions in the molecule (OH and  $\text{NH}_3^+$  groups change into OD and  $\text{ND}_3^+$  groups) which is reflected in the changes of Raman and IR spectra (Figure 6.9). The observed changes can be divided into six main groups:

(i) The  $\nu(\text{O-D})$  vibrations observed in Raman spectra as broad overlapping bands at approximately  $2170\text{ cm}^{-1}$  (hydroxyl in the carboxyl group) and  $2250\text{ cm}^{-1}$  (hydroxyls at the aromatic ring). The relatively low intensity and broad character of these bands are caused by the strong interactions of hydroxyl groups with the solvent. In the case of deuterated L-DOPA analogues, the  $\nu(\text{O-D})$  vibrations are partially overlapped with the more pronounced  $\nu(\text{C-D})$  vibrations. (ii) The  $\nu(\text{N-D}_3)$  vibrations, particularly the symmetric one, evidenced as a very weak (but recognizable) band at  $2020\text{ cm}^{-1}$ . This band is also widened thanks to the strong interaction with the solvent. (iii) Slight  $\sim 4\text{ cm}^{-1}$  shift of  $\nu(\text{C=O})$  vibrations at  $\sim 1730\text{ cm}^{-1}$ , caused by the hydrogen/deuterium exchange at the carboxyl group, observable in both IR and Raman spectra. (iv) Sharpening of the band at  $\sim 1610\text{ cm}^{-1}$  in Raman spectra and a slight shift of bands at  $\sim 1610$  and  $1530\text{ cm}^{-1}$  in the IR spectra. These bands correspond to the asymmetric (higher wavenumber) and symmetric (lower wavenumber)  $\delta(\text{N-H}_3)/\delta(\text{N-D}_3)$  deformations which are only weakly evidenced in Raman but easily traceable in IR. (v) The variations of both IR and Raman spectral shapes in  $1180 - 1320\text{ cm}^{-1}$  region correspond to the  $\nu(\text{C-OH})/\nu(\text{C-OD})$  and  $\delta(\text{C-OH})/\delta(\text{C-OD})$  vibrations. (vi) Sharpening of the band at  $\sim 790\text{ cm}^{-1}$  in Raman spectrum corresponds to the aromatic ring  $\delta(\text{CCC})$  breathing vibrations and  $\delta(\text{OCO})$  vibrations.

In summary, the hydrogen-deuterium exchange on the “soft” positions enables relatively easy empirical identification of the corresponding spectral bands especially in the higher vibrational region.

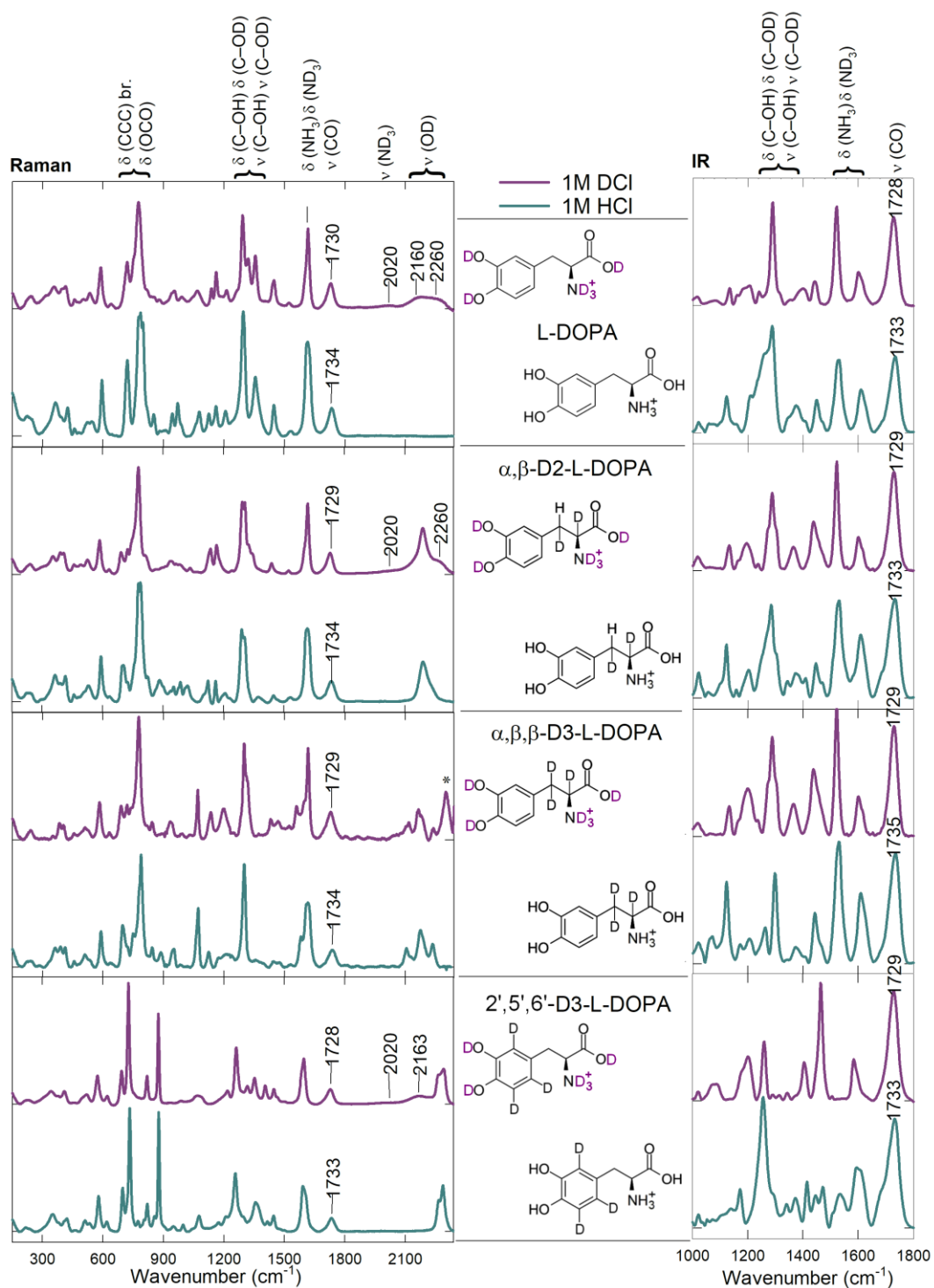


Figure 6.9: Raman and IR spectra of all L-DOPA samples in 1M HCl and 1M DCl where the interchange of hydrogen atom for the deuterium atom is happening on the soft positions. (br. – breathing vibration; \* – artefact)

Spectral manifestations of the deuteration on the “hard” (carbon) positions within L-DOPA molecule is considerably more distinctive as demonstrated in the Figure 6.10 where Raman signals of compounds (I), (IV), (V), and (VI) are compared. As expected, the most significant changes are found in the region of C–H and C–D

stretching vibrations. The changes in the fingerprint region are more subtle (with exception of the compound **VI** which is deuterated on the aromatic ring) which means that the overall spectral shape in this region is given mainly by the bands that correspond to the phenyl group vibrations.

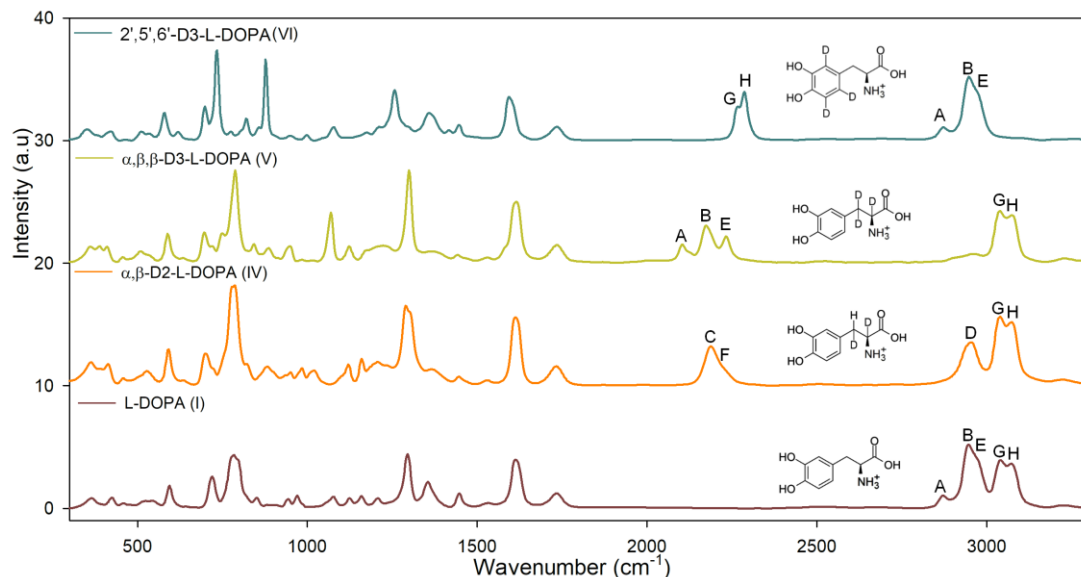


Figure 6.10: Raman spectra of differently deuterated samples in 1M HCl.

Thanks to the known deuteration patterns we may empirically assign all bands in the C–H and C–D stretching region (A – H): bands G and H at 3034 and 3081  $\text{cm}^{-1}$  move upon deuteration of the phenyl ring to 2262 and 2287  $\text{cm}^{-1}$ , respectively (compare the blue (**VI**) and the maroon (**I**) lines in the Figure 6.10). These bands thus certainly correspond to the out-of-phase and in-phase C–H stretching vibrations at the phenyl group, respectively. Remaining three bands with a lower wavenumber then have to correspond to different in-phase and out-of-phase combinations of C–H/C–D stretching vibrations at  $C_{2/\alpha}$  and  $C_{3/\beta}$ . A comparison of the spectra of L-DOPA samples **IV** and **V** (orange and lime line in the Figure 6.10), which are deuterated at aliphatic part of the molecule ( $C_{2/\alpha}$  and  $C_{3/\beta}$ ), enables further assignment. When all three hydrogens are exchanged for deuteria (sample **V**, lime line), the corresponding spectral pattern composed of the peaks A, B, and E remains similar to that in the non-deuterated L-DOPA (**I**), it is only shifted to the lower wavenumbers. However, when only one hydrogen at  $C_{3/\beta}$  is exchanged for deuterium, the characteristic pattern vanishes; there is a single band C with a shoulder F at the C–D stretching region and a single band D in C–H stretching region which position corresponds to the peak B in the spectrum of L-DOPA. Therefore, we may assign all peaks as shown in the Table 6.3.

Table 6.3: Empirical assignment of C–H and C–D vibrations.

peak	I	IV	V	VI	Assignment
A	2870 cm <sup>-1</sup>		2104 cm <sup>-1</sup>	2872 cm <sup>-1</sup>	v(C-H <sub>2</sub> ) / v(C-D <sub>2</sub> ) C <sub>3</sub> ss
B	2941 cm <sup>-1</sup>		2173 cm <sup>-1</sup>	2944 cm <sup>-1</sup>	v(C-H) / v(C-D) C <sub>2</sub>
C		2186 cm <sup>-1</sup>			v(C-D) C <sub>3</sub> , v(C-D) C <sub>2</sub> ip
D		2959 cm <sup>-1</sup>			v(C-H) C <sub>3</sub>
E	2977 cm <sup>-1</sup>		2235 cm <sup>-1</sup>	2979 cm <sup>-1</sup>	v(C-H <sub>2</sub> ) as / v(C-D <sub>2</sub> ) as
F		2236 cm <sup>-1</sup> sh			v(C-D) C <sub>3</sub> , v(C-D) C <sub>2</sub> op
G	3034 cm <sup>-1</sup>	3034 cm <sup>-1</sup>	3035 cm <sup>-1</sup>	2264 cm <sup>-1</sup>	v(C-H) ip / v(C-D) ip phenyl
H	3081 cm <sup>-1</sup>	3080 cm <sup>-1</sup>	3082 cm <sup>-1</sup>	2288 cm <sup>-1</sup>	v(C-H) op / v(C-D) op phenyl

v – stretching vibration; ip – in phase; op – out of phase

More precise assignment of vibrations in the fingerprint region is though impossible merely on the empirical basis, therefore we shifted from the purely experimental investigation to the QM simulations of vibrational profiles.

## 6.5 VOA spectra of L-DOPA

In this section we present ROA spectra of liquid samples measured in Olomouc by RNDr. Josef Kapitán, Ph.D. along with their parent Raman spectra. We also present the IR spectra of solid and liquid form of L-DOPA which were measured simultaneously with VCD on the spectrometer ChiralIR-2X<sup>TM</sup> at the Institute of Physics in Prague. Unfortunately, measurement of the VCD was accompanied by some difficulties which we discuss below in the section 6.5.1.

Figure 6.11 shows the Raman, ROA and IR spectra of L-DOPA with assigned vibrational modes according to the Table 6.6 (section 6.6.3). Some of the computed modes are not recognizable in the Raman spectrum. This is caused firstly by the fact that the resolution is not high enough and the peaks of the vibrations with close frequencies merge together, and secondly by the interaction of L-DOPA molecule with the solvent through the hydrogen bonds which results in the widening of the bands. The second problem concerns mainly the OH and NH vibrations in the higher spectral region above 3200 cm<sup>-1</sup>. In total, we were able to distinguish ~60 spectral features in the Raman spectrum in the region 100-3900 cm<sup>-1</sup> using the second derivative of the spectrum. In ROA the number of identified bands was lower (~40) due to the unresolved features in the CH/NH/OH stretching region (above 2750 cm<sup>-1</sup>) and higher noise level. In IR only 22 individual spectral features (bands and shoulders) were found as the spectrum was recorded only in the 900-1900 cm<sup>-1</sup> spectral region. Obtaining of the reasonable liquid phase VCD spectrum

was extremely difficult and demanding. Even though both of the DOPA enantiomers were available, only  $\sim 5$  spectral features could be assigned with certainty (we discuss this in detail in the following subsection 6.5.1).

The quality of the measured Raman and ROA spectra was exceptionally good and enabled detailed interpretation and assignment of individual vibrational features in the whole region of fundamental molecular vibrations. It should be emphasized that ROA instrument in Olomouc routinely enable reproducible measurement in both CH stretching region ( $2700\text{-}3900\text{ cm}^{-1}$ ) and low-wavenumber (terahertz) region (down to  $\sim 75\text{ cm}^{-1}$ ), which is unparalleled to other ROA instruments both commercial or home-build. CID (ROA to Raman signal ratio) is relatively low for L-DOPA, the most intense bands reach the value  $\sim 4 \cdot 10^{-4}$  ( $\sim 6 \cdot 10^{-5}$  in CH stretching region). IR and VCD spectra have mainly supportive and complementary character to Raman and ROA data. IR absorbance in 1M HCl was very low even at 100mg/ml sample concentration (6  $\mu\text{m}$  spacer) with maximum about 0.15. The g factor  $\leq 9 \cdot 10^{-5}$  shows that VCD signal was also rather low when compared to IR, which made its acquisition quite difficult.

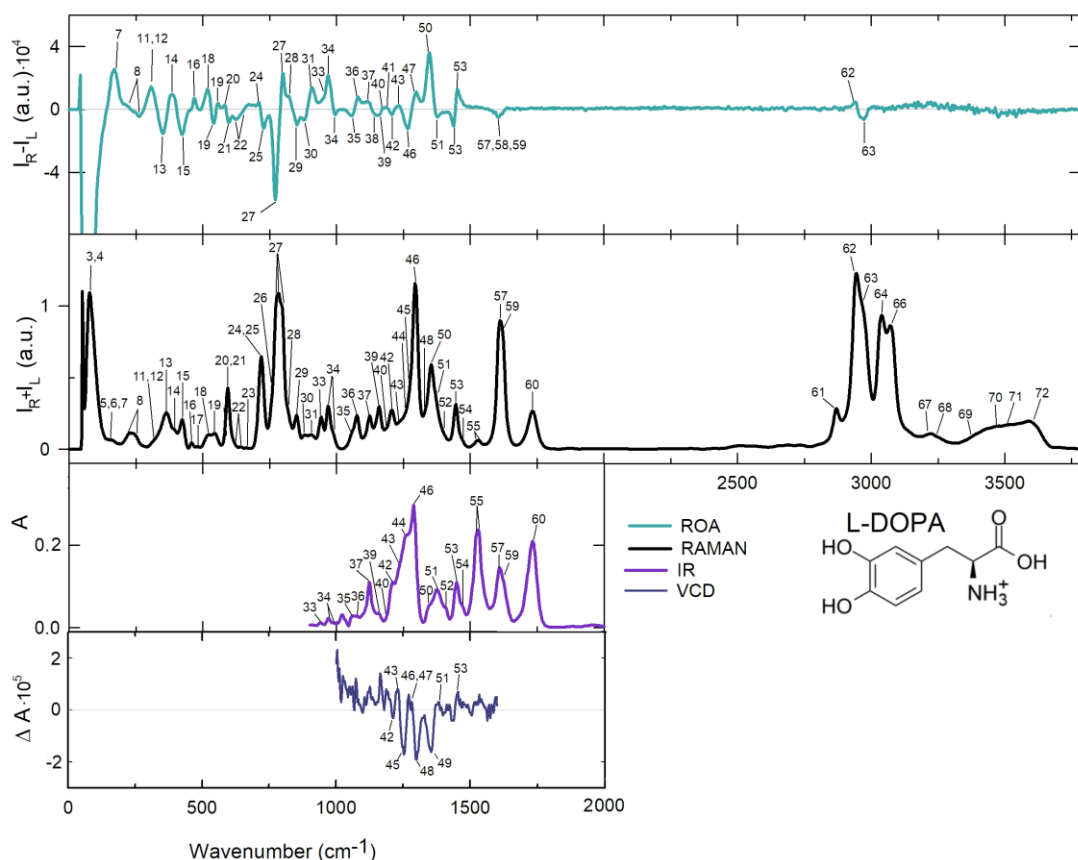


Figure 6.11: VOA spectra of L-DOPA. Numbering of the vibrational modes corresponds to the Table 6.6. VCD spectra were acquired as a half of the difference between spectrum of L-DOPA and D-DOPA in order to lower the number of artefacts.

### 6.5.1 VCD spectra of DOPA

The motivation was to measure the VCD spectra of both enantiomers of non-deuterated DOPA and then measure the spectra of other deuterated analogues using the same methodology. Especially, we hoped to get the spectrum of  $\alpha,\beta$ -D<sub>2</sub>-L-DOPA which would help us to determine the enantiomeric purity of the sample at the second chiral centrum C<sub>β</sub>. With a huge help of Vladimír Kopecký Jr., Ph.D. we attempted to measure VCD spectra of L-DOPA and its deuterated derivatives in solid and liquid state. In this section we focus on the results of non-deuterated samples, deuterated samples are discussed in the section 6.7.

The measurement of the solid-state samples went quite smoothly and the post-processing of the spectra was not a problem, we present the results in the Figure 6.12. The post-processed spectra are shown in the first panel along with half of their sum which indicates which parts of the spectra are burdened with high inaccuracy; these are the areas around 1150 – 1200 cm<sup>-1</sup> with a strong KBr signal, but then also the areas around 1250 and 1550 cm<sup>-1</sup> where the artefacts cannot be explained by the KBr signal. The middle panel shows the IR spectrum of L-DOPA and in the bottom panel are the processed spectra of L- and D-DOPA after artefact subtraction (i.e. calculated as a half of the difference between the measured L-DOPA and D-DOPA spectrum and vice versa) However, it is evident that in case both enantiomers of the studied substance would not be for disposal, the acquired VCD spectra would be burdened by significant errors.

On the other hand, the measurement of the liquid samples was more complicated. Firstly we measured all samples **I** – **VI** in concentration of 100 mg/ml in 1M HCl with the use of 6 μm Mylar spacer where we faced several problems starting with the sample preparation, where we had to work very carefully not to leave any air bubbles in the cuvette. We used 6 μl of the sample each time. The next obstacle was the drying out of the sample which caused a drop in the intensity of the signal after a few hours (generally 5). However, the main problem was that the VCD signal of DOPA is simply too weak and not even 15 hours of measurement were enough to obtain a nice spectrum. Moreover, the VCD signal had a strong background which was not caused by the solvent and due to which it was impossible to determine the baseline, and several artefacts which were not reducible by the spectral subtraction. While attempting to process the spectra, we realized that the results are unusable, and we

decided to try a 15  $\mu\text{m}$  Teflon spacer instead of the 6 $\mu\text{m}$  Mylar one, which caused the appropriate increase of absorbance. However, the absorbance of the solvent (water) was also increased by the same factor which led to the higher noise in the 1550–1750  $\text{cm}^{-1}$  region. Using the Teflon spacer we measured only samples **I** and **III** (L-DOPA and D-DOPA) and we were able to gain reasonably looking and reproducible signal of the two enantiomers in the 1000 – 1550  $\text{cm}^{-1}$  region (Figure 6.13). The signal was very noisy above that region due to the high absorbance of the solvent (water). The artefact from  $\text{CaF}_2$  cuvette is visible around 1170  $\text{cm}^{-1}$ . Despite all our efforts, we were able to assign only several bands in area from 1200 to 1450  $\text{cm}^{-1}$  (Figure 6.11 and Figure 6.27). On the positive side, spectral features in this region correspond to the simulated VCD spectra quite well. Their comparison is given in the section 6.7.

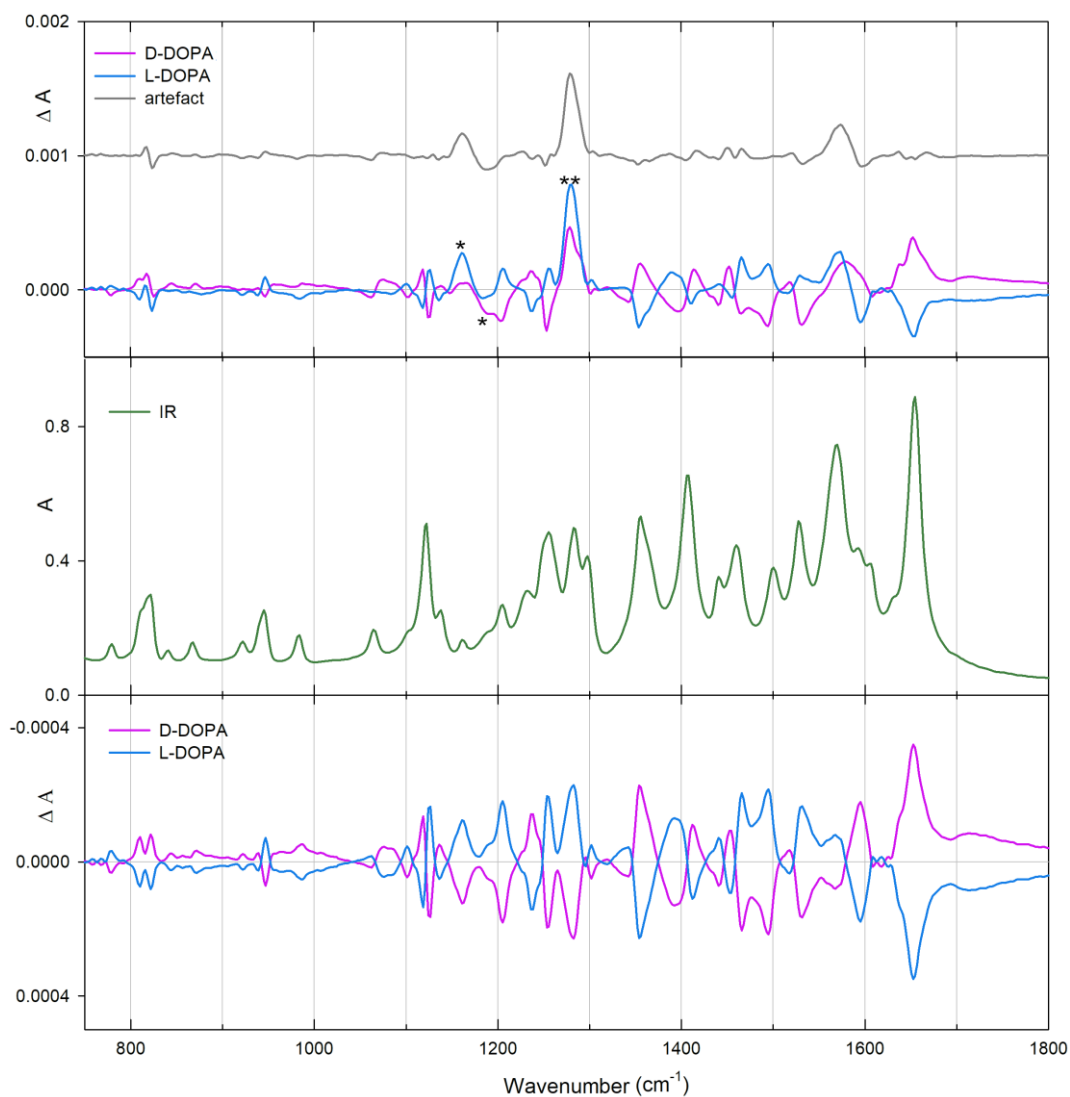


Figure 6.12: Solid phase VCD spectra of the two enantiomers of DOPA and their differential spectrum (top), overlapping IR spectra of both enantiomers (middle), and solid phase VCD spectra of DOPA enantiomers after artefact spectrum subtraction (bottom). \* – artefact from KBr, \*\* – artefact of an unknown origin.



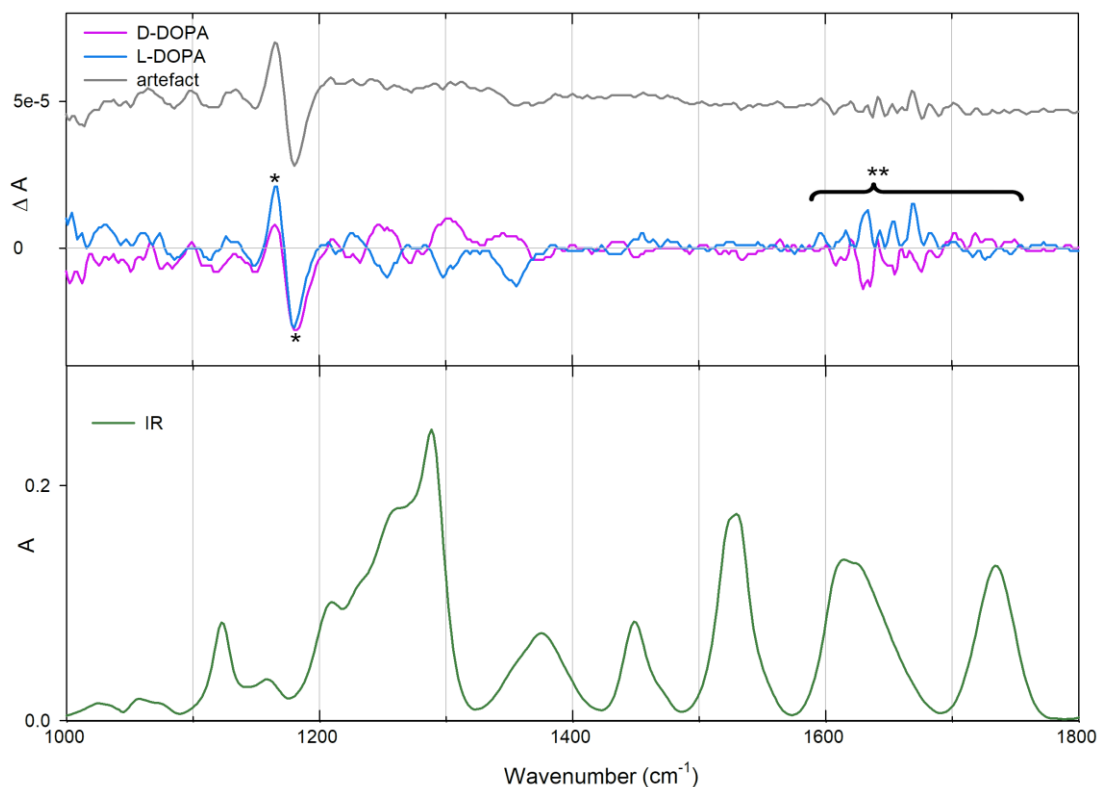


Figure 6.13: Liquid state VCD (top) and IR (bottom) spectra of the two enantiomers of DOPA in a 100 mg/ml solution in 1 M HCl. \* – artefact from  $\text{CaF}_2$ , \*\* – region of high water absorbance burdened with high noise signal.

In conclusion, the Raman, ROA and IR experimental spectra of L-DOPA solution in 1M HCl were measured without big complications, except the fact that ROA measurement was quite time consuming ( $\sim 30$  hours for one spectrum). All of them are of such good quality that it is possible to compare them to the simulated spectra and assign the majority of spectral features to the specific vibrational motions. On the other hand, measurement of the VCD spectra of liquid samples yielded ambiguous results. VCD signal of DOPA is undoubtedly very low (at least  $10^4$  times lower than IR absorption signal) and it is burdened with low signal-to-noise ratio. The results were reproducible after using a  $15\ \mu\text{m}$  Teflon spacer. The down side of such thick layer of sample is, that it made it impossible to obtain the spectrum in the  $1550 - 1750\ \text{cm}^{-1}$  region due to a high water absorbance.

## 6.6 Ab initio calculations of L-DOPA

In this section the process of calculation of Raman, ROA, IR and VCD spectra is shown. The conformational analysis was performed on the cationic form of L-DOPA and the calculation was performed by Gaussian 09 software (Frisch et al., 2009).

### 6.6.1 Conformational analysis

Levodopa is a small and flexible molecule, therefore, it has more possible conformations which can coexist in the aqueous solution. To find the most probable conformers, we defined 5 torsion angles in the cationic form of L-DOPA ( $\alpha$ - $\gamma$ ) (see Figure 6.14) and we performed a scan of the molecule's energy with a step of  $10^\circ$  for each defined angle, keeping the rest of the molecule rigid. We used the functional B3LYP, 6-31+G\* Pople basic set, and water as an implicit solvent in C-PCM theory. The results of this process is shown in the Figure 6.14. The description of the torsion angles and their positions in the local energy minima is given in the Table 6.4. While the energy of the molecule changes smoothly with the rotation of the angles  $\alpha$ ,  $\beta$ , and  $\delta$ , this is not the case with the other two angles. During the rotation of  $\gamma$  and  $\varepsilon$  at one point the energy of the molecule decreases rapidly (see orange and green lines marked by triangles in the Figure 6.14). In case of  $\gamma$ , this is accompanied by the change of the angle  $\beta$  and in case of  $\varepsilon$  by the change of  $\delta$ . Therefore, we run the scan also backwards (lines marked by circles in the Figure 6.14) to confirm the positions of the located potential energy minima. While the energy minima of forward and backward scans align well for  $\alpha$ ,  $\beta$ ,  $\delta$ , and  $\varepsilon$ , in case of  $\gamma$  the  $C_3$  minimum in the backward scan is shifted from  $132^\circ$  to  $102^\circ$ .

Table 6.4: Angle's values at the local energy minima of L-DOPA and their description.

angle	# of energy minima and the angle position	description
$\alpha$	2: $-35^\circ$ , $155^\circ$	rotation of the carboxylic group
$\beta$	3: $-170^\circ$ , $-60^\circ$ , $69^\circ$	rotation of the alaninyl chain
$\gamma$	3: $-79^\circ$ , $72^\circ$ , $132^\circ$	rotation of the phenyl group
$\delta$	2: $0^\circ$ , $180^\circ$	rotation of the $C_3$ hydroxylic group
$\varepsilon$	2: $0^\circ$ , $180^\circ$	rotation of the $C_4$ hydroxylic group

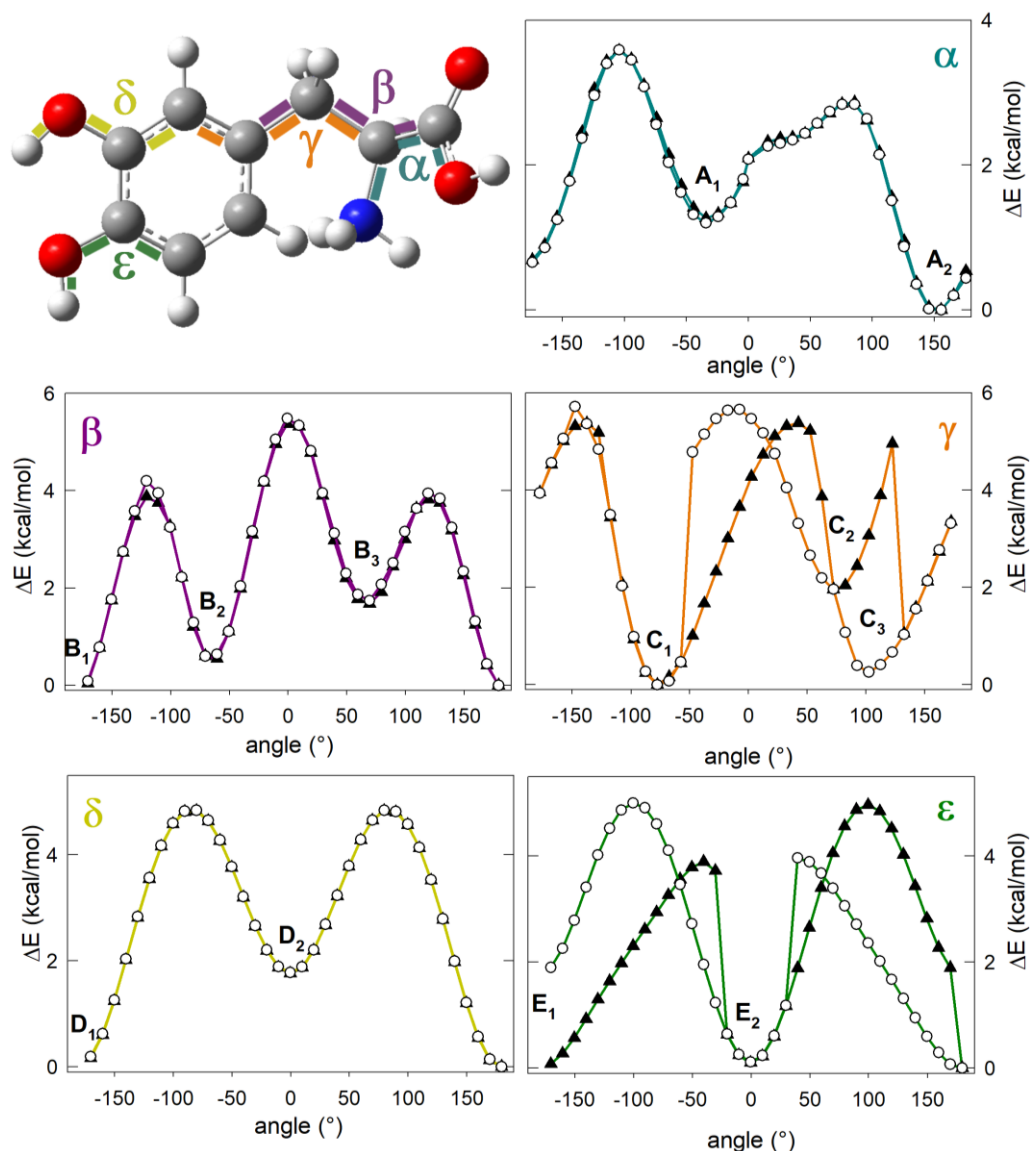


Figure 6.14: Definition of five torsion angles within L-DOPA structure characterising its conformation and the results of the 1D potential energy scans along the change of each of the angles with  $10^\circ$  step.

In order to estimate more accurately how the torsion angles interfere with one another, we run three 2D scans during which the neighbouring pairs of angles on the alaninyl chain:  $[\alpha, \beta]$  and  $[\beta, \gamma]$  and the pair of angles defining the steric position of hydroxyls on the phenyl ring,  $[\delta, \epsilon]$ , were simultaneously changed with a  $10^\circ$  step. The scans were calculated on the B3PW91/6-31G level of theory. Resulting 2D sections of the whole molecular potential energy surface along with the positions of the angles at local energy minima are shown in the Figure 6.15. Red areas correspond to the arrangement of the angles resulting in the lowest relative energy of the molecule. Local energy minima are marked with capital Greek letters:  $\Sigma_i = \{[\alpha_i, \beta_i]\}$ ,  $\Delta_i = \{[\beta_i, \gamma_i]\}$ , and  $\Omega_i = \{[\delta_i, \epsilon_i]\}$ .

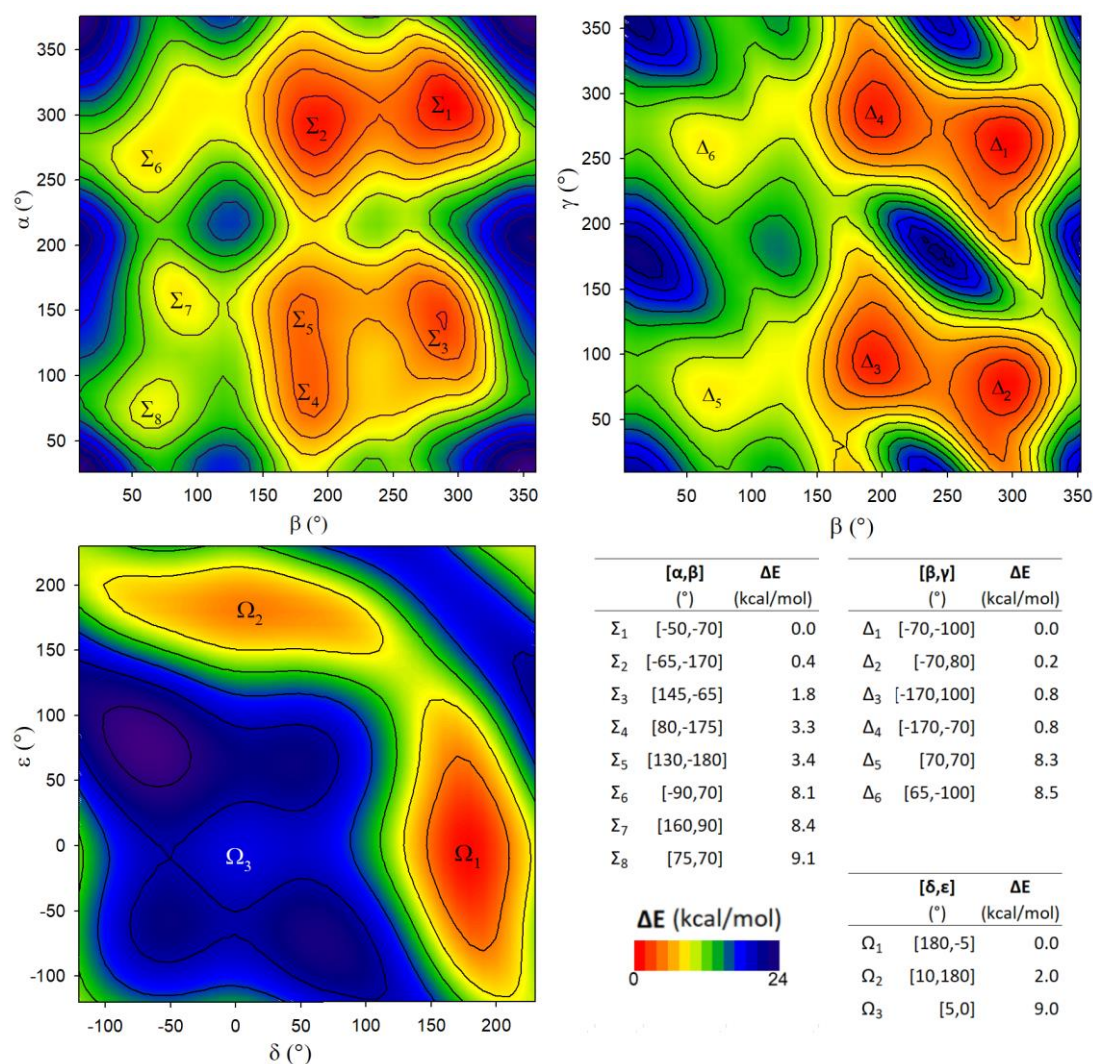


Figure 6.15: 2D potential energy scans of L-DOPA molecule covering  $[\alpha, \beta]$ ,  $[\beta, \gamma]$ , and  $[\delta, \epsilon]$  pairs of dihedral angles together with the overview of the all located local energy minima.

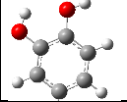
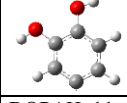
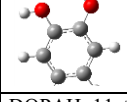
Despite the 1D scan revealed energy minima for two orientations of each OH group on the phenyl ring (that is for the angles  $\delta$  and  $\epsilon$ ), which means that theoretically there are 4 possible preferred mutual positions, 2D scan showed only three of them. The most unstable arrangement ( $\delta=\epsilon=180^\circ$ ), where the OH groups are facing towards each other, was not evaluated as an energy minimum during the 2D scan. Yet, from the molecular dynamics provided by Mgr. Jakub Klener at the Faculty of Mathematics and Physic of Charles University we know that the occurrence of these kind of conformers is non-zero. The actual overall occurrence of the conformers is affected by the interactions of the hydroxyl groups with the solvent via hydrogen bonds for which we did not account in the computation. Nevertheless, we assume that the missing

conformers do not significantly affect the accuracy of the results due to their low actual occurrence.

The approximate values of individual angles in the local minima found by 2D scan are:  $\alpha \in \{-70^\circ, 140^\circ, 75^\circ\}$ ,  $\beta \in \{-170^\circ, -70^\circ, 70^\circ\}$ ,  $\gamma \in \{-100^\circ, -70^\circ, 75^\circ, 100^\circ\}$ ,  $\delta \in \{0^\circ, 180^\circ\}$ , and  $\varepsilon \in \{0^\circ, 180^\circ\}$ . However, we do not need to take into account all possible combinations ( $4 \times 3 \times 4 \times 2 = 96$ ) of these angles for further conformational analysis because, if we look closely, some of them are already eliminated (e.g. from  $\beta \otimes \gamma = 3 \times 4 = 12$  possible combinations of  $\beta$  and  $\gamma$ , only six of them correspond to one of the minima). For further analysis we had chosen 54 ( $= 6 \times 3 \times 3$ ) conformers:  $\Delta \otimes \alpha \otimes \Omega$ ; thus we added only one extra combination of  $[\alpha, \beta]$  which was not present in the found minima and that was  $[75^\circ, -75^\circ]$ . We named the conformers DOPAH\_XYtc/cc/ct, where  $X \in \{1, 2, 3\}$  and marks the value of  $\alpha$ :  $\alpha_1 = -70^\circ$ ,  $\alpha_2 = 140^\circ$ ,  $\alpha_3 = 75^\circ$ ,  $Y \in \{1, 2, 3, 4, 5, 6\}$  and marks the combination of  $\beta$  and  $\gamma$ :  $\Delta_1 \dots \Delta_6$ , and t and c stand for trans ( $180^\circ$ ) and cis ( $0^\circ$ ) and denote the rotation angles  $\delta$  and  $\varepsilon$ , respectively. For these conformers we performed geometry optimization using the B3PW91 functional, 6-311++G\*\* Pople basis set and water as an implicit solvent in C-PCM theory. Resulting conformers are divisible into three groups based on the orientation of the OH groups on the phenyl ring:  $\Omega_1$ ,  $\Omega_2$ , and  $\Omega_3$ ) thanks to the fact that their rotation is adiabatically separable from the rotation of the torsion angles at the alaninyl chain. Accordingly, we determined the percentage occurrence of each conformer, both within the respective  $\Omega$  group and in total, based on the conformer's energies. The results are shown in the **Error! Reference source not found.**

The interaction of the OH groups of L-DOPA with the water molecules of the solvent, which is omitted in the computation, plays an important role in the stability of the conformers. That is why, even though the computed overall joint occurrence of the 12 conformers from cc ( $\Omega_3$ ) group is merely 1.7%, we did not discard them from the spectral analysis. We assume that the actual fraction of cc group is higher thanks to the hydrogen bonds which it forms with the solvent. As we will see in the next section, the comparison of computed and experimental spectra justifies this assumption.

Table 6.5: Most probable conformations of L-DOPA

conformer	$\alpha$	$\beta$	$\gamma$	$\delta$	$\varepsilon$	overall					within $\Omega$ group						
						$\Delta E$	$\Delta E_0$	$\Delta H$	$\Delta G$	$\eta$	$\Delta E$	$\Delta E_0$	$\Delta H$	$\Delta G$	$\eta$		
			( $^\circ$ )			(kcal/mol)					(kcal/mol)					(%)	
																	
DOPA_H_11tc	-73	-175	-77	-179	1	0.0	0.0	0.2	0.0	22.7	0.0	0.0	0.0	0.0			42.2
DOPA_H_12tc	-73	-175	102	180	0	0.3	0.5	0.6	1.0	14.3	0.3	0.5	0.4	1.0			26.7
DOPA_H_14tc	-52	-68	82	179	0	0.7	0.9	0.9	1.5	7.4	0.7	0.9	0.7	1.5			13.9
DOPA_H_13tc	-52	-67	-97	-179	1	0.9	1.1	1.1	1.6	5.2	0.9	1.1	0.9	1.6			9.7
DOPA_H_31tc	116	177	-74	-179	1	1.7	1.8	1.9	2.0	1.3	1.7	1.8	1.7	2.0			2.5
DOPA_H_22tc	117	176	100	180	-1	2.0	2.1	2.2	2.4	0.8	2.0	2.1	2.0	2.4			1.6
DOPA_H_16tc	-87	66	72	179	0	2.2	2.4	2.5	2.8	0.5	2.2	2.4	2.4	2.8			1.0
DOPA_H_34tc	132	-70	81	180	0	2.3	2.7	2.6	3.2	0.4	2.3	2.7	2.4	3.2			0.8
DOPA_H_15tc	-88	66	-104	-180	0	2.3	2.7	2.7	3.1	0.5	2.3	2.7	2.5	3.1			0.9
DOPA_H_33tc	131	-70	-97	-179	0	2.5	2.8	2.8	3.5	0.3	2.5	2.8	2.6	3.5			0.6
DOPA_H_36tc	86	62	73	179	0	3.6	3.7	3.8	3.9	0.1	3.6	3.7	3.6	3.9			0.1
DOPA_H_35tc	85	62	-104	-180	0	3.7	4.0	4.1	4.2	0.0	3.7	4.0	3.9	4.2			0.1
						$\Sigma$					43.5	$\Sigma$					100
																	
DOPA_C_11cc	-73	-175	-78	0	0	1.8	2.0	2.1	2.4	1.0	0.0	0.0	0.0	0.0			44.1
DOPA_C_12cc	-73	-175	103	-1	0	2.2	2.5	2.5	2.9	0.6	0.3	0.5	0.4	0.5			25.4
DOPA_C_14cc	-51	-68	83	-1	0	2.5	2.8	2.7	3.5	0.3	0.7	0.8	0.6	1.1			13.8
DOPA_C_13cc	-51	-68	-98	1	0	2.8	3.1	3.0	3.7	0.2	0.9	1.0	0.9	1.3			9.1
DOPA_C_31cc	107	179	-76	0	0	3.5	3.8	3.8	3.8	0.1	1.7	1.7	1.7	1.4			2.6
DOPA_C_22cc	109	179	106	0	0	3.8	4.1	4.2	4.4	0.0	2.0	2.1	2.1	2.0			1.6
DOPA_C_16cc	-87	66	73	-1	0	4.1	4.3	4.4	4.6	0.0	2.3	2.3	2.3	2.2			1.0
DOPA_C_34cc	133	-70	81	-1	0	4.2	4.5	4.5	5.1	0.0	2.3	2.5	2.3	2.7			0.8
DOPA_C_15cc	-88	66	-105	0	0	4.2	4.6	4.6	5.0	0.0	2.3	2.6	2.5	2.6			0.9
DOPA_C_33cc	132	-70	-98	0	0	4.4	4.8	4.7	5.5	0.0	2.6	2.8	2.6	3.2			0.6
DOPA_C_36cc	87	62	74	0	0	5.4	5.6	5.7	5.7	0.0	3.6	3.6	3.6	3.3			0.1
DOPA_C_35cc	85	61	-105	0	0	5.5	5.9	6.0	6.1	0.0	3.7	3.9	3.9	3.8			0.1
						$\Sigma$					1.7	$\Sigma$					100
																	
DOPA_T_11ct	-73	-176	-78	-1	180	0.1	0.2	0.3	0.6	19.1	0.0	0.0	0.3	0.0			43.5
DOPA_T_12ct	-73	-176	105	-1	-180	0.4	0.4	0.0	1.7	11.2	0.3	0.2	0.0	1.1			25.6
DOPA_T_14ct	-51	-68	82	-2	-180	0.8	1.0	0.9	1.6	6.2	0.7	0.8	0.9	1.0			14.1
DOPA_T_13ct	-51	-68	-98	1	180	1.0	1.2	1.2	1.7	3.9	0.9	1.0	1.2	1.1			9.0
DOPA_T_21ct	115	177	-77	-1	180	1.8	2.2	2.2	2.6	1.2	1.7	2.0	2.2	2.0			2.7
DOPA_T_22ct	109	179	107	0	-180	2.0	2.2	2.3	2.2	0.7	1.9	2.0	2.3	1.6			1.6
DOPA_T_16ct	-87	66	73	-1	-180	2.3	2.6	2.7	2.9	0.5	2.2	2.4	2.7	2.3			1.1
DOPA_T_15ct	-88	66	-105	1	-180	2.4	2.7	2.7	3.0	0.4	2.3	2.5	2.7	2.5			0.9
DOPA_T_34ct	133	-70	81	-3	180	2.4	2.7	2.7	3.3	0.4	2.3	2.5	2.7	2.7			0.9
DOPA_T_33ct	132	-70	-98	0	179	2.7	2.9	2.9	3.6	0.2	2.6	2.8	2.9	3.0			0.6
DOPA_T_36ct	87	63	74	0	-180	3.7	3.9	4.0	4.1	0.0	3.6	3.7	4.0	3.5			0.1
DOPA_T_35ct	86	62	-104	1	-180	3.8	4.0	4.1	4.1	0.0	3.7	3.8	4.1	3.6			0.1
						$\Sigma$					54.8	$\Sigma$					100

$\Delta E$  – energy difference from the minimum,  $\Delta E_0$  – difference of the zero-point energy,  $\Delta H$  – difference of the enthalpy,  $\Delta G$  – difference of the Gibbs energy

## 6.6.2 Spectral markers of different L-DOPA conformations

The aim of this section is to find spectral characteristic of different L-DOPA conformers in the computed spectra, to compare them with the experimental spectra, and, based on this comparison, to estimate the most common conformers and their probable population. All weighted averages of the spectra presented in this section are based on the energies ( $\Delta E$ ) of the conformers. Firstly, in the Figure 6.16 we present VOA (Raman, ROA, IR, and VCD) spectra of all 36 conformers from the **Error! Reference source not found.** and their Boltzmann weighted average (BA). The comparison of the spectra of all conformers demonstrates the difference in the sensitivity of the four techniques to the changes in the conformation of L-DOPA. Unsurprisingly, the two chiral techniques (ROA and VCD) are substantially more sensitive to the conformational changes than their parental non-chiral techniques (Raman and IR), which is manifested in greater variability of the 36 spectra. The biggest variability in Raman and IR spectra is in the region of low spectral shift ( $0 - 500 \text{ cm}^{-1}$ ) and in the region of N-H<sub>3</sub> vibrations (around  $3500 \text{ cm}^{-1}$ ). However, the NH<sub>3</sub> bands in the experimental Raman spectra are not well differentiated due to the strong interaction with the solvent, lower region in the Raman spectra contains too many bands which often overlap and become undistinguishable. The IR spectra were measured only in the region from  $900$  to  $1800 \text{ cm}^{-1}$ ; therefore, comparison to both low-wavenumber and N-H<sub>3</sub> vibrations region remained inaccessible.

In contrast, computed ROA and VCD spectra differ significantly depending on the conformation and the averaging has more significant effect than in the case of their parenting spectra. Chiral techniques are simply more sensitive to the conformational changes, which is why in the further conformer analysis we will focus mainly on them, and specifically on ROA because of the low quality of experimental VCD spectra, as discussed above in the section 6.5.1.

In the Figure 6.17 three different averages are introduced: black line represent the BA of all 36 spectra where all three possible orientations of the phenyl OH groups (tc, cc, and ct) contribute equally to the final spectra, green line represents simple non-weighted average of all 36 spectra, and finally, the orange line represents BA of all 36 spectra where the ratio of the occurrence of the different orientations of OH groups is given by the results of the geometry optimisation (tc:cc:ct=43:2:55). The plain spectral average (green line) differs significantly from the two weighted averages and the differences do not correspond to the experimental, therefor spectra. The two weighted

spectra are almost identical; they differ only in the intensities, not in the positions of the bands. This validates the importance of the spectral weighing and confirms the assumption that certain conformers are preferred. Nevertheless, the computed ratio of the conformers with different OH orientations most probably does not correspond to the reality because our model uses only implicit solvent; hence, does not take into account the hydrogen bonds which are undoubtedly formed between the OH groups and H<sub>2</sub>O molecules of the solvent and stabilize the cc conformation. Thus, we assume that the contribution of the cc conformation is in fact much higher and comparable to the other two conformations. However, the fact that the two weighted spectra are almost identical means that the rate of occurrence of the three classes with different orientations of OH groups does not significantly influence the appearance of the spectra, as long as they are all present. This is further confirmed in Figure 6.18 where the comparison of BA spectra of the three groups of conformers with different OH orientation is given; the differences of their spectra are subtle, therefore, we decided to stick with the ratio tc:cc:ct=1:1:1.

Next, we moved on to a more detailed examination of how the orientations of the other three torsion angles,  $\alpha$ ,  $\beta$ , and  $\gamma$ , influence the spectra. For every torsion angle we divided the conformers after the geometry optimisation (**Error! Reference source not found.**) into two or three groups based on the preferred orientations of that particular angle and made a Boltzmann weighted average of the relevant spectra. For angle  $\alpha$  we divided the conformers into two groups: first with positive value of  $\alpha$  ( $\alpha+$ ) and second with negative  $\alpha$  ( $\alpha-$ ); for  $\beta$  there are three preferred orientations: trans ( $\sim 180^\circ$ ) gauche+ ( $\sim +70^\circ$ ) and gauche- ( $\sim -70^\circ$ ); and for  $\gamma$  there are also two groups: with positive and with negative  $\gamma$  ( $\gamma+$  and  $\gamma-$ ). The results are shown in the Figure 6.19, Figure 6.21, and Figure 6.23.



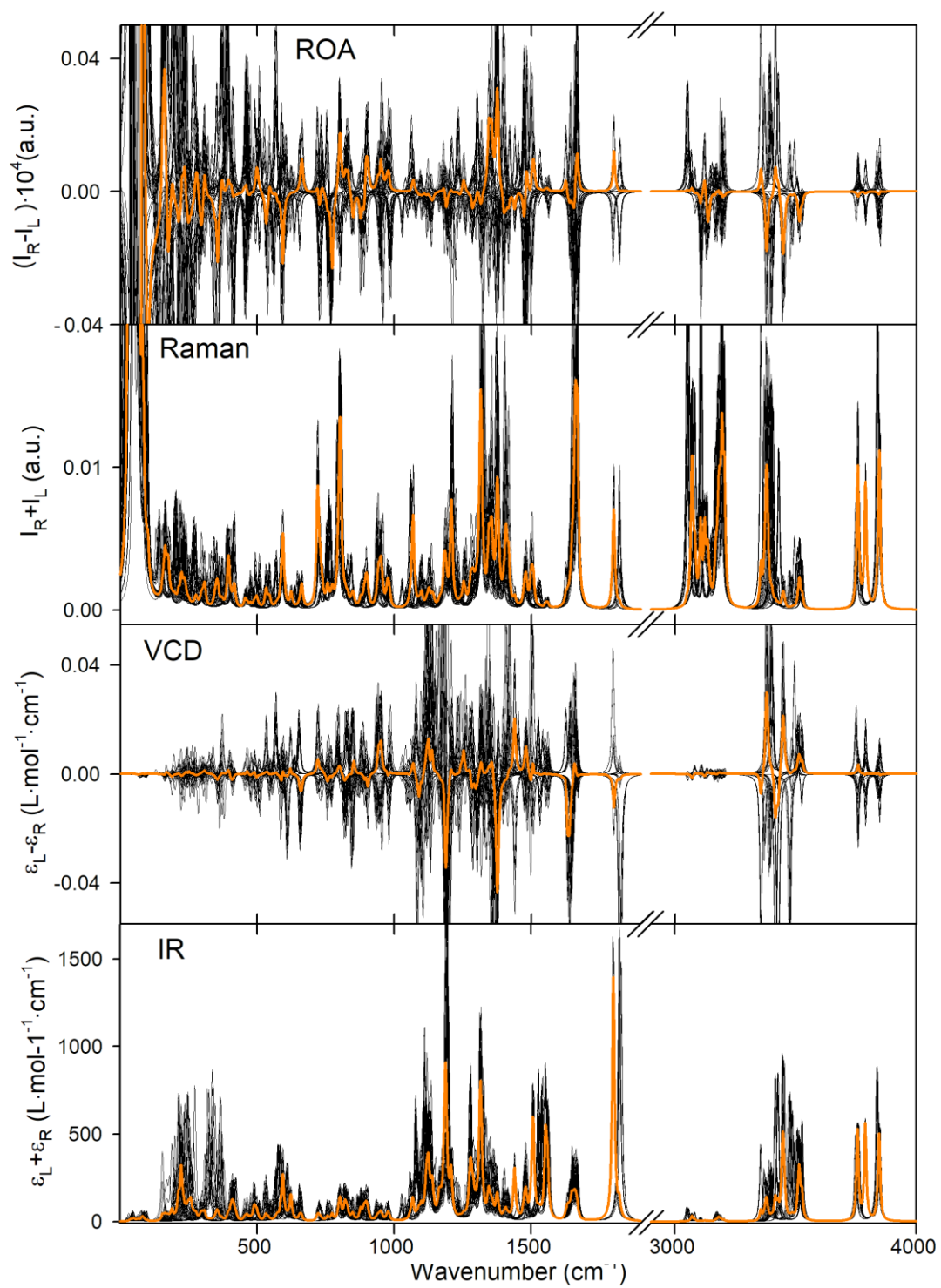


Figure 6.16: Computed VOA spectra of all individual 36 conformers (black lines) and their Boltzmann-weighted average (orange line).

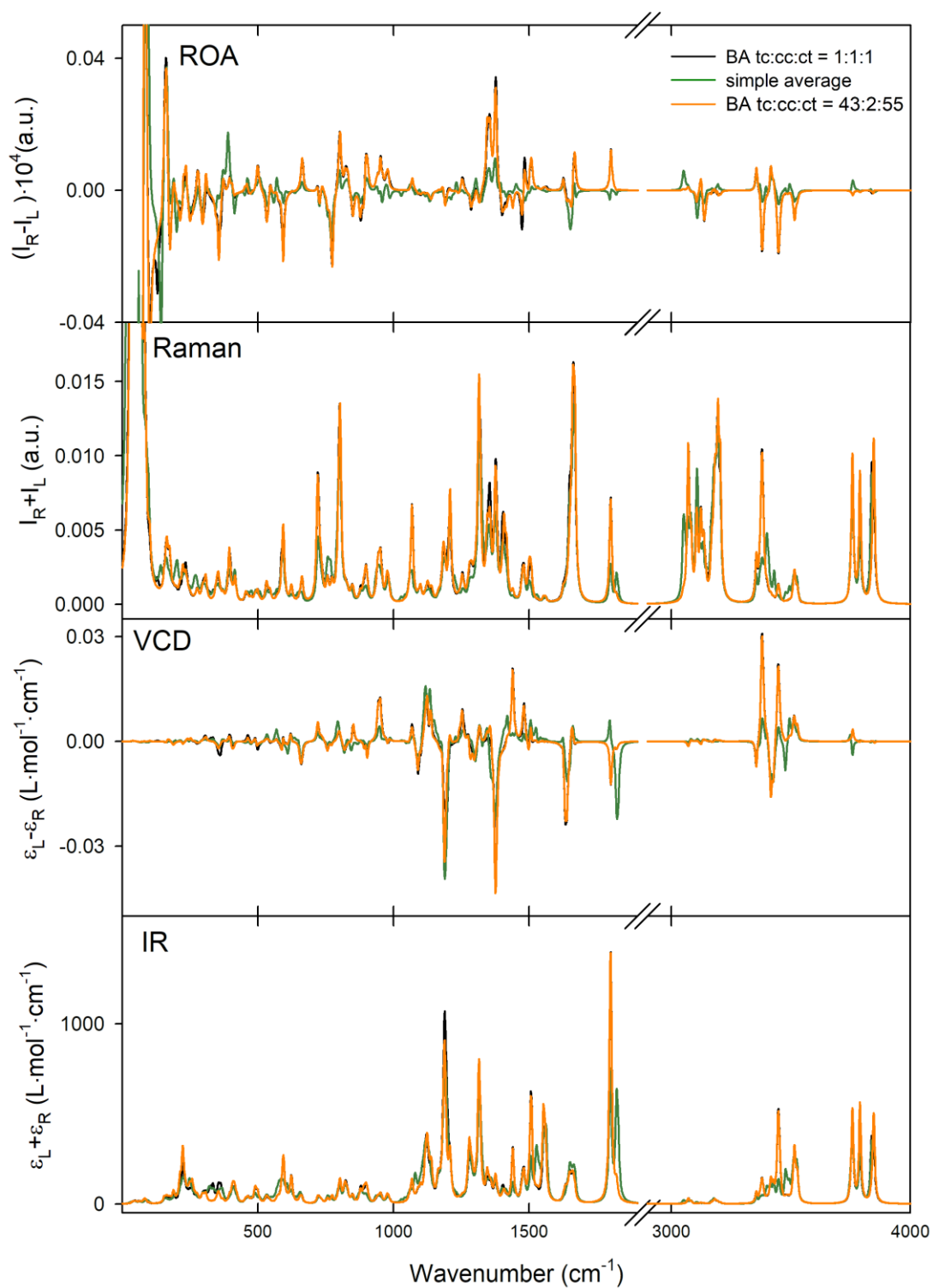


Figure 6.17: Differently weighted averages of the computed spectra of all 36 conformers based on the division into 3 groups with different OH orientation.

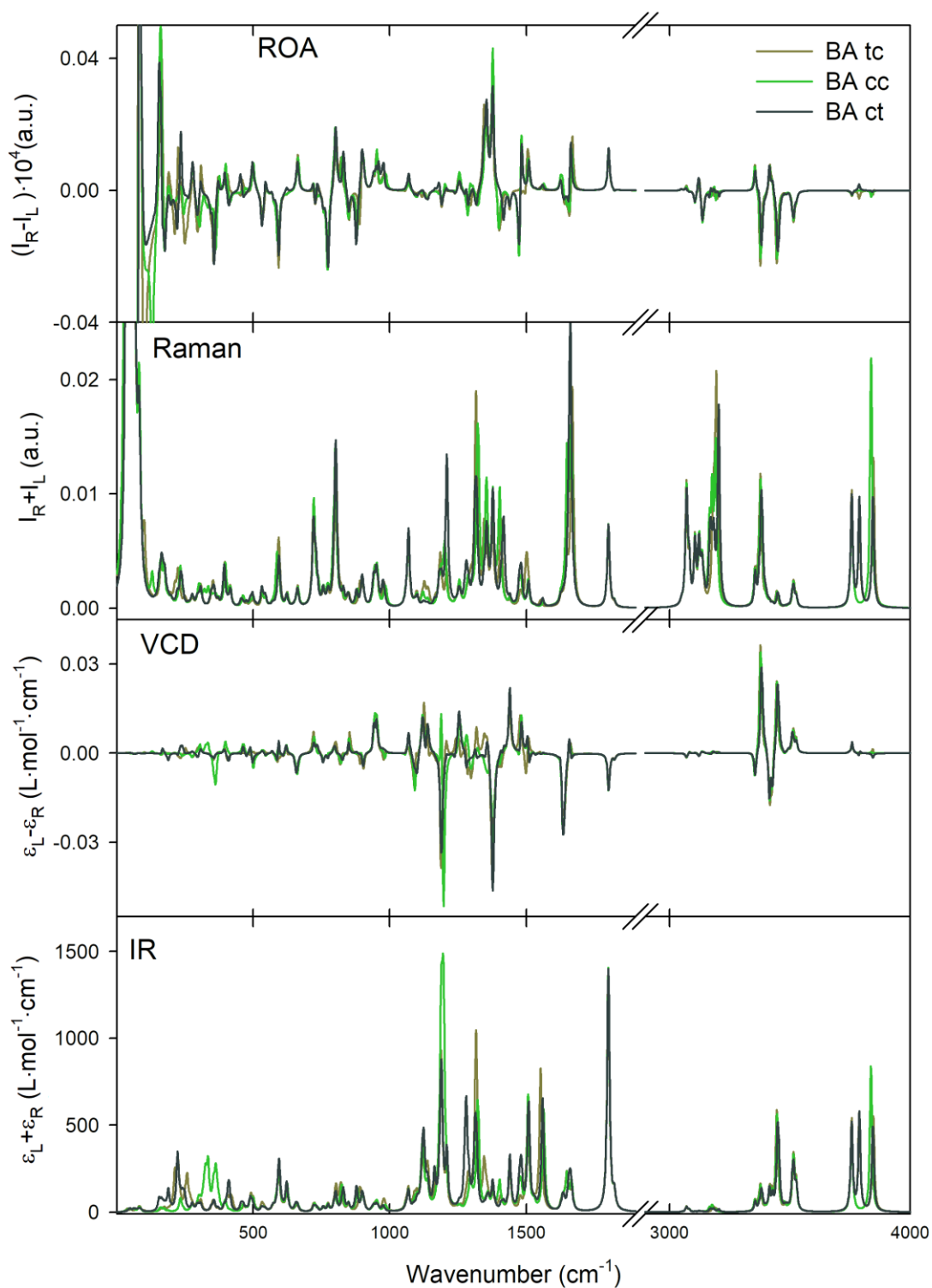


Figure 6.18: Boltzmann-averaged spectra of the three groups of conformers with different orientation of OH groups.

In the Figure 6.19 a comparison of the spectra for two different orientations of  $\alpha$  is shown. The most specific difference between them is the band corresponding to the vibration of the carboxyl group ( $\sim 1800\text{ cm}^{-1}$ ). The orientation of the band has an opposite orientation in ROA spectra and it is shifted in other three spectra. The NH vibrations ( $\sim 3500\text{ cm}^{-1}$ ) differ significantly but in the experimental Raman and IR spectra these bands are broadened and merged together, and they disappear completely in VOA and VCD due to the formation of hydrogen bonds between  $\text{NH}_3$  group and the water molecules of the solvent. This disables the comparison of  $\text{NH}_3$  bands with the computed spectra. Significant differences in the ROA spectra are observable also in the region  $\sim 1300 - 1600\text{ cm}^{-1}$ . In the experimental spectra a  $-++--+$  pattern is observable in this region to which clearly contribute both orientations of  $\alpha$  (see Figure 6.20). The estimate of the ratio of their occupation can be done based on the carboxyl valence vibration at  $1720\text{ cm}^{-1}$  (around  $1800\text{ cm}^{-1}$  in the computed spectra) which vanishes in the experimental ROA spectra thanks to the contribution from both conformers. Moreover, the width of the band in experimental Raman spectra also indicates that it is composed of two peaks which are however so close that they cannot be distinguished. Based on that, we can assume that despite the ratio of both conformers from geometry optimization is considerably unbalanced ( $(\alpha^+):(\alpha^-) = 6:94$ ), the real ratio would be more even ( $(\alpha^+):(\alpha^-) \approx 40:60$ ). The  $\alpha^-$  orientation is preferred in the computational results due to the formation of hydrogen bond between the amine and carboxyl groups. In reality  $\alpha^+$  conformation is stabilized by the hydrogen bonds formed with the  $\text{H}_2\text{O}$  solvent molecules which are not accounted for in the computations.

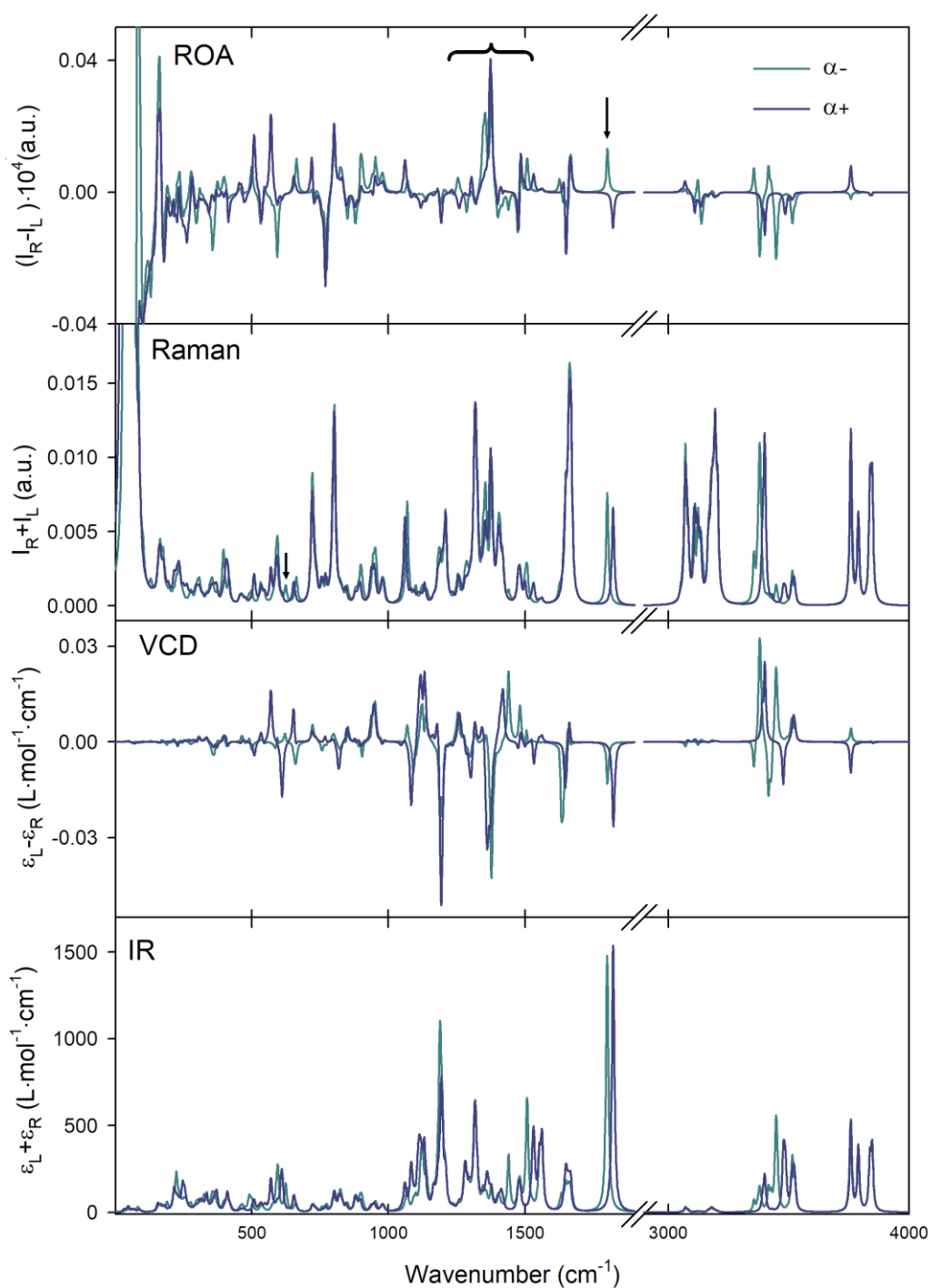


Figure 6.19: Boltzmann weighted average VOA spectra of L-DOPA for two different conformations of the angle  $\alpha$ .

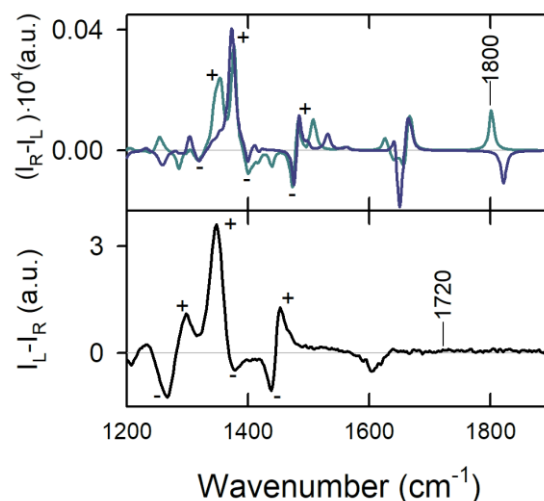


Figure 6.20: Computed (top) and experimental (bottom) ROA spectra. Determination of the occurrence of two different orientation of the angle  $\alpha$ .

Figure 6.21 shows the comparison of spectra of three different orientations of the angle  $\beta$  (trans, t; gauche-, g-; gauche+, g+). Results of the geometry optimization showed us that their ratio is t:(g-):(g+) = 73:25:2. Change of  $\beta$  affects the spatial configuration of the alaninyl chain in an immediate proximity of the chiral carbon  $C_2$ , so the value of  $\beta$  significantly influences spectra from the chiral techniques (ROA and VCD). From the comparison of the spectral characteristics (wavenumbers, intensities, and the sign of the bands) of the computed spectra with the experimental spectra, it is obvious that the trans conformation is dominant (60 – 70 %). The most convincing demonstration of that is the peak in ROA spectrum at  $1375\text{ cm}^{-1}$  to which contributes only the trans conformation and which is clearly observable in the experimental spectrum at  $1348\text{ cm}^{-1}$  (see the Figure 6.22). The g- conformation is present in smaller but not negligible amount (20 – 30 %) which can be demonstrated on the negative band at  $726\text{ cm}^{-1}$  ( $727\text{ cm}^{-1}$  in the experiment), and finally, the g+ conformation is least represented (< 10 %) which we assume based on the fact that there are several bands of g+ and trans conformations with opposite sign in ROA, e.g.  $800\text{ cm}^{-1}$  and  $1375\text{ cm}^{-1}$  or the couplet at  $1476$  a  $1486\text{ cm}^{-1}$ , but in the experimental spectra the signs of the corresponding peaks agree with those of the trans conformation and their intensity is not significantly lowered. Therefore, the experimental data are in a good agreement with the computed ratio of individual orientations of  $\beta$ .

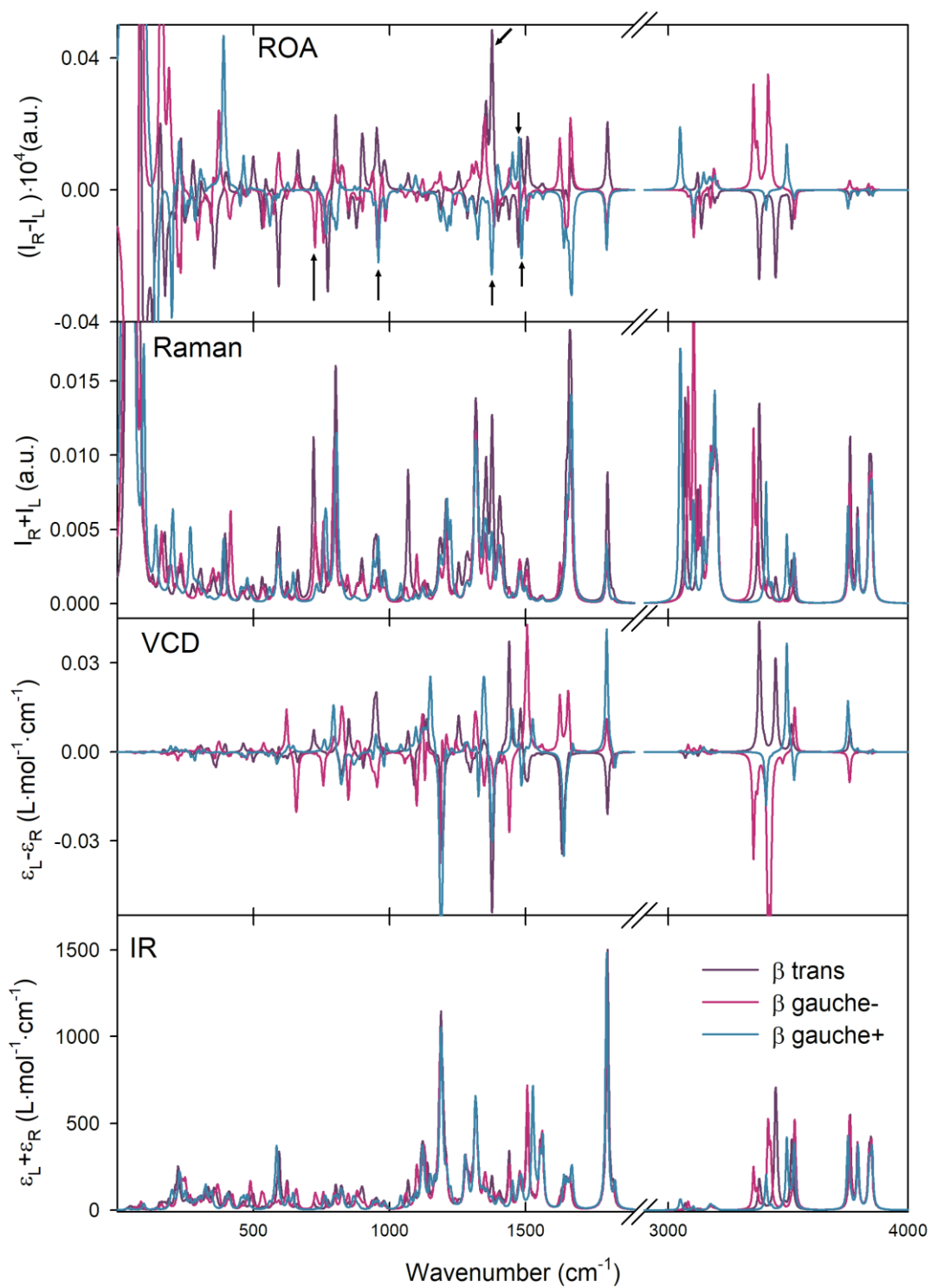


Figure 6.21: Boltzmann weighted average VOA spectra of L-DOPA for three different conformations of the angle  $\beta$ .

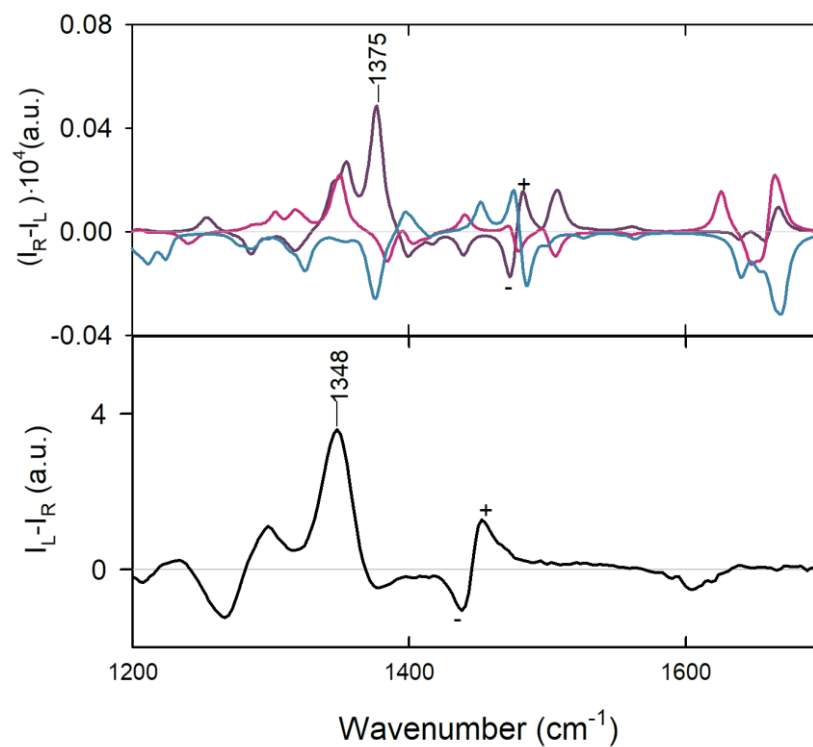


Figure 6.22: Computed (top) and experimental (bottom) ROA spectra. Determination of the occurrence of three different orientation of the angle  $\beta$ .

Figure 6.23 shows the spectral comparison of two different orientations of  $\gamma$  ( $\gamma^+$  and  $\gamma^-$ ). Value of  $\gamma$  defines the orientation of the phenyl group. There is no chemical or spatial reason for neither of the orientations to be significantly preferred which is confirmed by the computed ratio of the conformers with different  $\gamma$ :  $(\gamma^+):(\gamma^-) = 57:43$ . ROA spectra appear to be very sensitive to the change of  $\gamma$ , VCD is less sensitive and IR and Raman are almost insensitive.



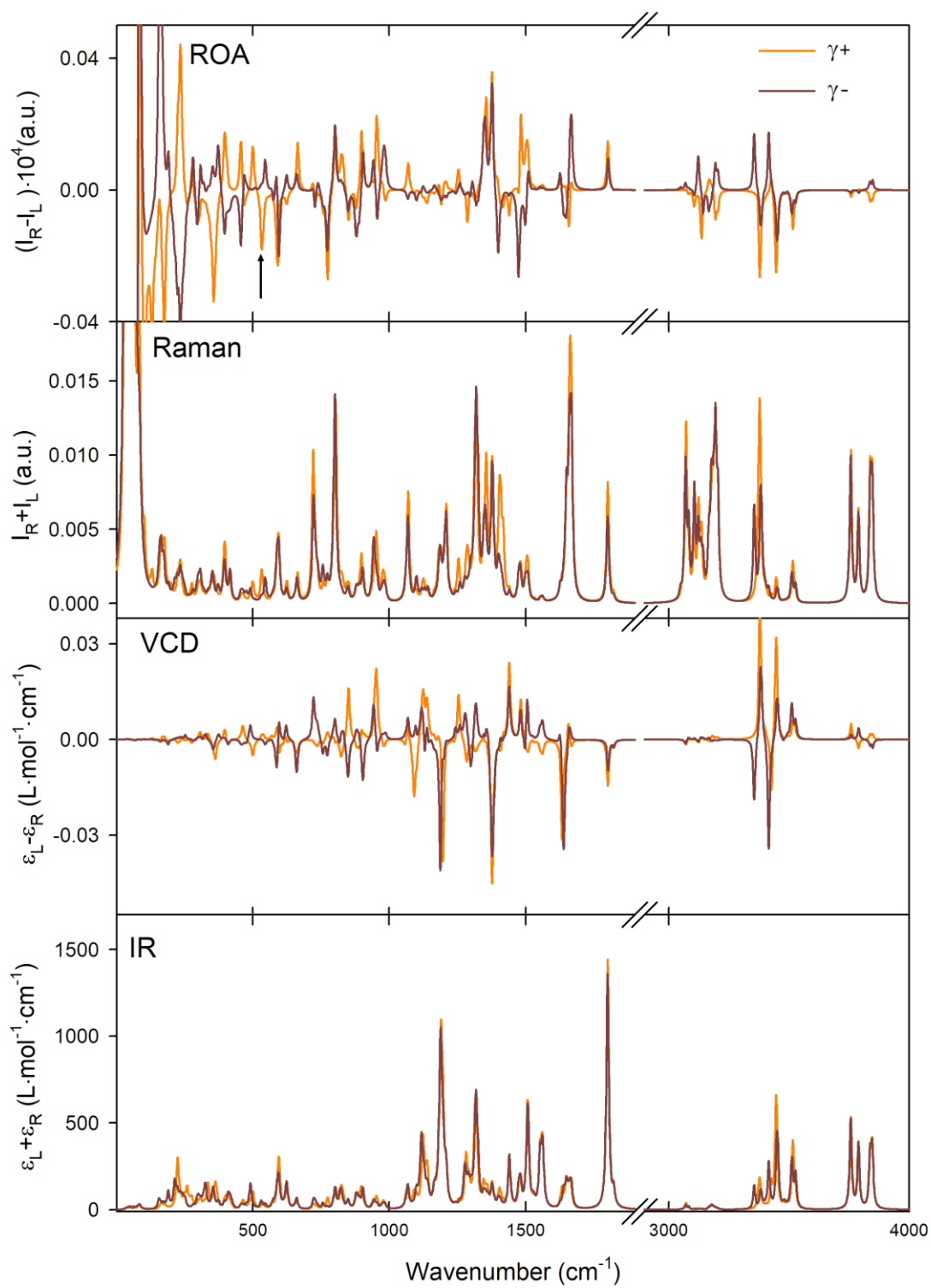


Figure 6.23: Boltzmann weighted average VOA spectra of L-DOPA for two different conformations of the angle  $\gamma$ .

Above, the probable percentage occurrences of the possible orientations of defined torsion angles were determined. Based on that we created a new modified weighting of conformers which satisfies those conditions: we adjusted the ratios of  $\alpha^+$  and  $\alpha^-$  to 2:3 and ct:cc:ct to 1:1:1. Computed ratios for  $\beta$  (t:(g-):(g+) = 73:25:2) and  $\delta$  ( $\gamma$ : ( $\gamma^+$ ):( $\gamma^-$ ) = 57:43) were not changed as they are in a good agreement with the experiment. Subsequently, BA VOA spectra with modified weighting were created. The comparison of this modified BA spectra (blue lines) to the original BA spectra (black lines) is shown in the picture Figure 6.24. The spectra differ marginally, however the slight differences in ROA spectra work in favour of the modified spectrum: the intensity of the couplet around  $1470\text{ cm}^{-1}$  is higher in the modified spectrum, the difference in the intensities of the two peaks around  $1350\text{ cm}^{-1}$  is bigger which corresponds better to the experiment, the negative band around at  $775\text{ cm}^{-1}$  is the strongest one (without taking into account the strong band in the lowest part of the spectrum), and there are positive peaks at  $569$  and  $720\text{ cm}^{-1}$  (see Figure 6.25). All these factors in which modified ROA spectrum differs from the non-modified are in a better agreement with the experimental ROA spectrum.

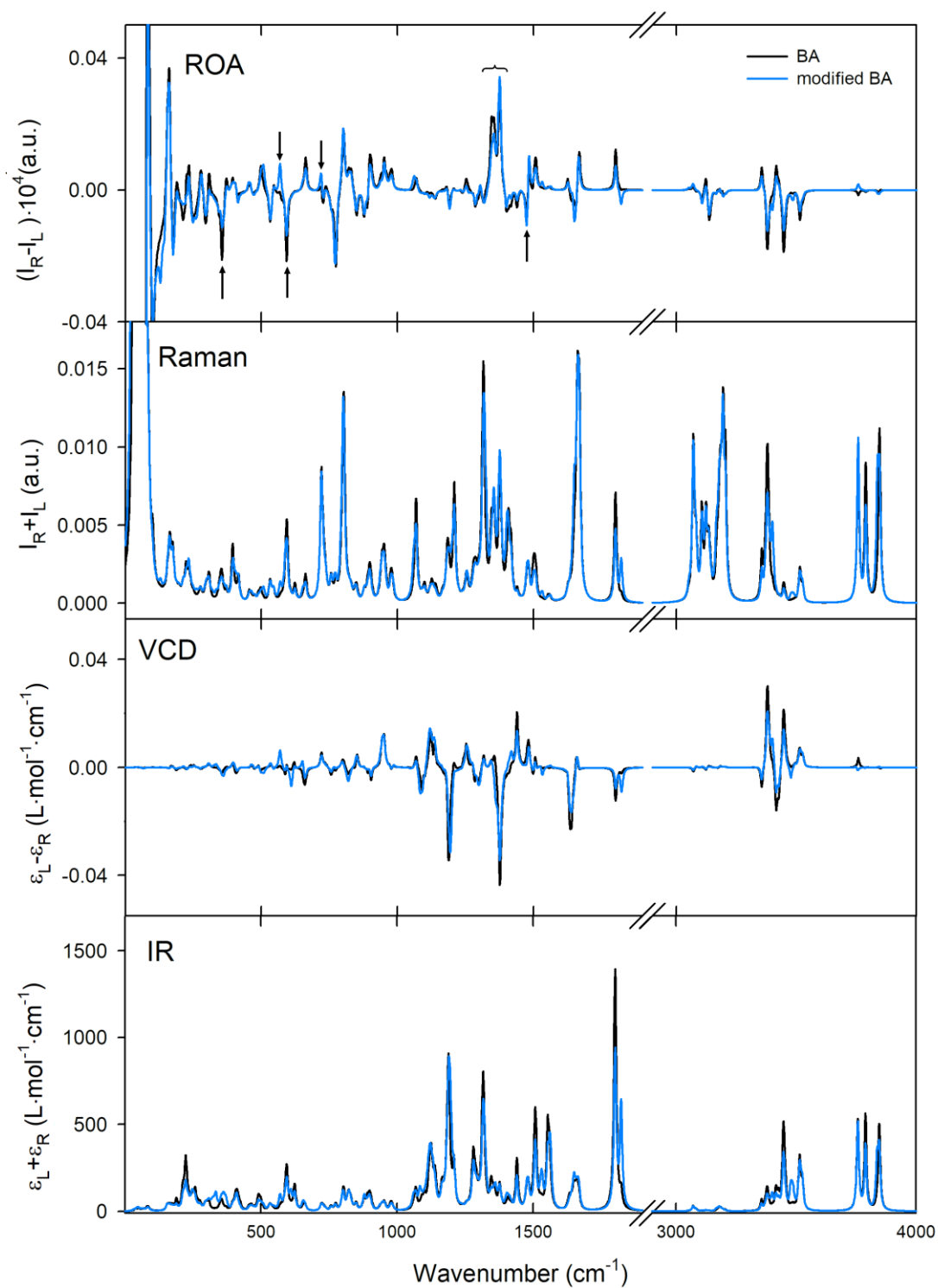


Figure 6.24: Boltzmann average VOA spectra of L-DOPA weighted based on the computed ratios of the conformer groups (black line) and the modified computed ratios (blue lines).

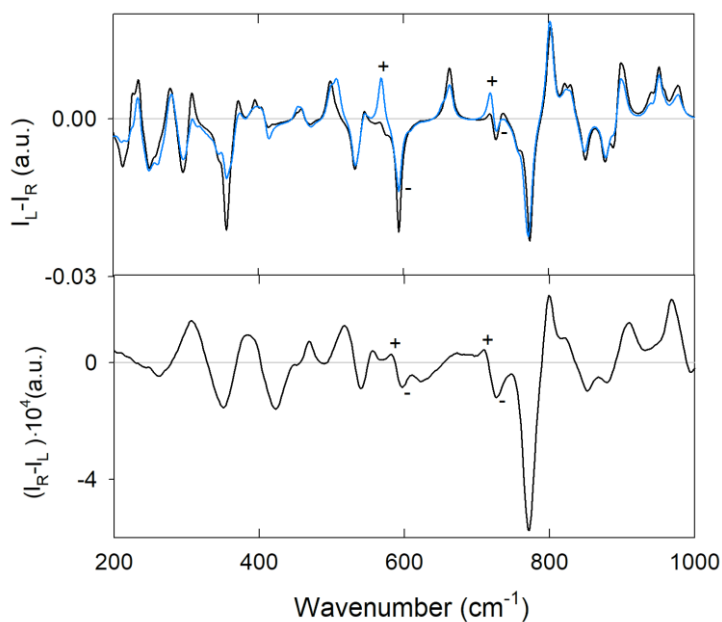


Figure 6.25: Computed (top) and experimental (bottom) ROA spectra which correspond better to the BA spectra weighted by the modified computed ratios (blue line).

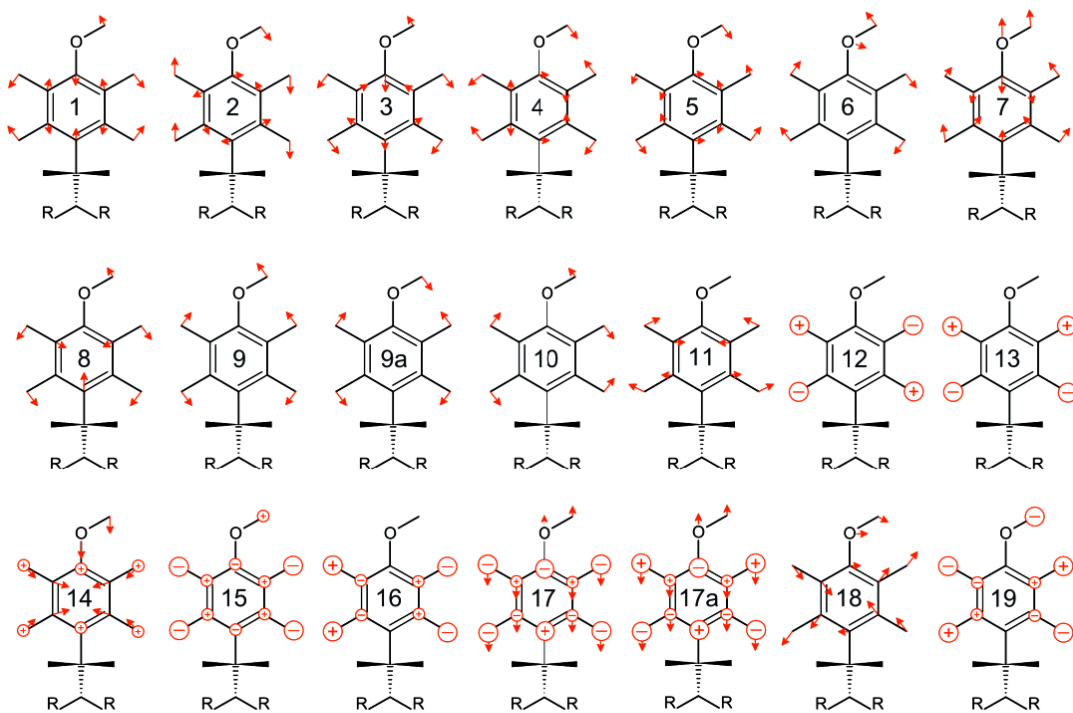
### 6.6.3 Vibrational assignment of L-DOPA spectra

As thoroughly discussed in the previous sections, L-DOPA in solution occurs in a dynamic equilibrium between many different conformations. Although all these conformations contribute to the measured signal (regardless of which of the VS method we use), their contribution depends on their relative occurrence. Therefore, we used the spectrum of the conformer with the highest relative occurrence, DOPAH\_11tc (Table 6.5) for actual assignment of the vibrational modes. The vibrational assignment is shown in Table 6.6 along with the frequencies and intensities of corresponding experimental Raman, IR, ROA and VCD bands measured in 1M HCl.

For the description of the vibrations we used the commonly used designation by Greek letters along with the designation of the tyrosine vibrations ( $Y_x$ ) introduced in (Profantová, 2013) and the Wilson's nomenclature of benzene ring modes ( $\nu_x$ ; Wilson, 1934), both are shown in the Figure 6.26.

Due to the used approximations (namely the harmonic approximation) and a limited level of theory used for spectral simulation (B3PW91/6-311++G\*\*/cpcm (water)), the simulated intensities are lightly upshifted in the lower spectral region and downshifted in the middle and higher regions; the turn occurs around  $900\text{ cm}^{-1}$ . The comparison of the experimental and simulated (modified BA of all conformers, see previous subsection 0) spectra is shown in the Figure 6.28.

### a) Tyrosine (Y)



### b) Benzene ( $\nu$ )

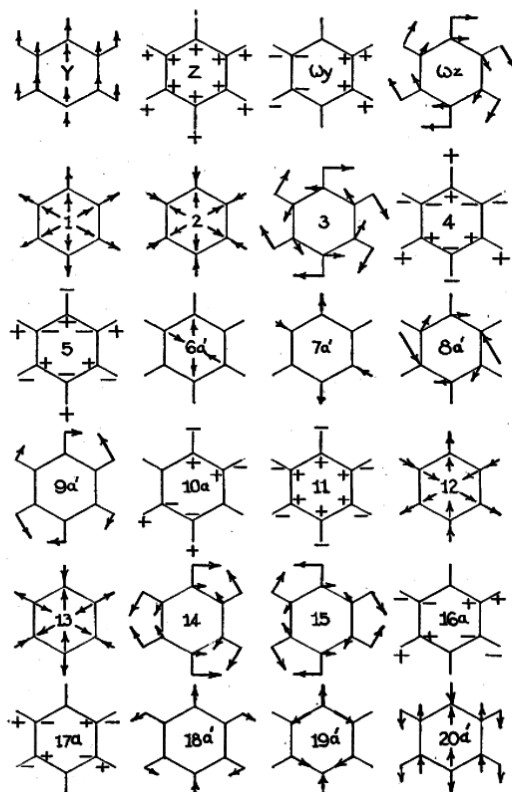


Figure 6.26: Tyrosine (a) and benzene (b) vibrational modes. Pictures are adopted from (Profantová, 2013) and (Wilson, 1934), respectively.

Table 6.6: Vibrational assignment of L-DOPA spectra

Mode	DFT* v(cm <sup>-1</sup> )	Raman v(cm <sup>-1</sup> )	IR v(cm <sup>-1</sup> )	ROA v(cm <sup>-1</sup> )	VCD v(cm <sup>-1</sup> )	Assignment
1	39	-	-	-	-	whole structure twist
2	51	-	-	-	-	whole structure twist
3	64	75 sh	-	-	-	whole structure bending
4	79	-	-	96 s-	-	δ(CCC) aliphatic twist
5	162	-	-	-	-	δ(CCC) C <sub>1</sub> -C <sub>2</sub> -(C <sub>3</sub> Phe)
6	175	166 m	-	-	-	δ(CCC) (Phe)-C <sub>3</sub> -C <sub>2</sub>
7	184	-	-	169 s+	-	δ(NH <sub>3</sub> ) τ
8	227	222 w 246 sh	-	207 m+ 263 w-	-	γ(CO-H) C <sub>3</sub> , C <sub>4</sub> ip, δ(NCCC) N C <sub>2</sub> C <sub>3</sub> C <sub>1</sub>
9	259	-	-	-	-	γ(CO-H) C <sub>3</sub> , C <sub>4</sub> ip
10	276	-	-	-	-	δ(C-CN) C <sub>2</sub> -(COOH)(NH <sub>3</sub> )(CH <sub>2</sub> Phe), γ(CO-H) C <sub>3</sub> , C <sub>4</sub> ip
11	299	314 sh	-	312 m+	-	δ(OCCO) C <sub>3</sub> , C <sub>4</sub>
12	311	-	-	-	-	δ(CCCN) C <sub>1</sub> , C <sub>3</sub> C <sub>2</sub> N, δ(OCCO) C <sub>3</sub> , C <sub>4</sub>
13	357	364 m	-	351/377 m-/vw-	-	δ(CCCN) C <sub>1</sub> , C <sub>3</sub> C <sub>2</sub> N
14	396	392 sh	-	394 vw-	-	γ(CCCC) C <sub>1</sub> C <sub>2</sub> C <sub>3</sub> C <sub>1</sub> , γ(CO-H) C <sub>3</sub> , C <sub>4</sub> op,
15	413	424 m	-	423 m-	-	γ(CCC) v <sub>16b</sub>
16	455	457 w	-	468 m+	-	γ(CO-H) C <sub>3</sub> , C <sub>4</sub> op
17	463	479 vw	-	-	-	γ(CCC) v <sub>16a</sub>
18	498	509 sh 520 w	-	517 m+	-	γ(CCC) v <sub>16a</sub>
19	532	547 w	-	540/557 m-/w+	-	δ(CCC) Y18 v <sub>6b</sub> , δ(CCCC) C <sub>1</sub> C <sub>2</sub> C <sub>3</sub> C <sub>1</sub>
20	592	593 s	-	580/596 vw+/m-	-	γ(CO-H) C <sub>1</sub> , δ(CCC) Y18 v <sub>6b</sub>
21	596	-	-	-	-	γ(CO-H) C <sub>1</sub>
22	623	623 sh	-	626 m-	-	δ(CCN) C <sub>1</sub> C <sub>2</sub> N
23	660	643 vw 663 vw	-	642 sh 665 w+	-	δ(CCCC) C <sub>1</sub> C <sub>2</sub> C <sub>3</sub> C <sub>4</sub> , γ(CCC) Y17a v <sub>4</sub>
24	716	719 s	-	708 m+	-	γ(CCC) Y17a v <sub>4</sub> , γ(OCO)
25	725	-	-	727 m-	-	γ(CCC) Y17a v <sub>4</sub>
26	772	755 sh	-	-	-	δ(CCC) v1 ring breathing δ(C-C) C <sub>3</sub> -C <sub>2</sub> -COO
27	806	773 sh 785 sh 798 s	-	771 s- - 799 s+	-	δ(CCC) v1 ring breathing
28	820	820 sh	-	825 m+	-	γ(C-H) Y15 v <sub>17b</sub>
29	852	852 m	-	851 m-	-	γ(C-H) Y16 v <sub>10a</sub> , δ(C-H2) ρ C <sub>3</sub> , v(C-N)
30	893	880 w	-	877 m-	-	γ(C-H) Y13 v <sub>10b</sub>
31	900	910 w	-	907 m+	-	v(C-C) C <sub>1</sub> C <sub>2</sub> , δ(C-H2) ρ C <sub>3</sub>
32	947	-	-	-	-	γ(C-H) Y12 v <sub>17a</sub>
33	958	942 m	940 w	951 sh+	-	δ(C-C) C <sub>2</sub> C <sub>3</sub> , δ(C-H2) ρ C <sub>3</sub>
34	978	969 m 990 sh	970 w 989 sh	967 s+ 993 w-	-	δ(C-H) Y11 v <sub>18a</sub>
35	1072	1054 sh	1055 sh	1057 w-	-	v(C-N)
36	1090	1077 m	1077 sh	1080 m+	-	δ(N-H3) ω, δ(C-H2) τ C <sub>3</sub> , δ(C-H) C <sub>2</sub>
37	1128	1124 m	1123 m	1115 w+	-	δ(C-H) Y10 v <sub>15</sub> , δ(N-H3) ω, δ(C-H2) τ C <sub>3</sub> , δ(C-H) C <sub>2</sub> , δ(C-H) C <sub>2</sub> , δ(CO-H) C <sub>1</sub> C <sub>3</sub>
38	1143	-	-	1140 w-	-	δ(N-H3) ω, δ(C-H2) τ C <sub>3</sub> , δ(C-H) C <sub>2</sub> , δ(CO-H) C <sub>1</sub> C <sub>3</sub>
39	1170	1159 m	1158 sh	1156 w-	-	δ(C-H) Y10 v <sub>15</sub>
40	1187	1184 sh	1183 vw	1173 w+	-	δ(C-H) Y9a v <sub>9a</sub> , δ(CO-H) C <sub>3</sub>
41	1189	-	-	1187 w+	-	δ(CO-H) C <sub>1</sub> , δ(N-H3) ω
42	1209	1207 m	1208 sh	1205 w-	1209 w-	δ(C-H) Y9 v <sub>9a</sub> , δ(CO-H) C <sub>4</sub>
43	1253	1235 sh	1231 sh	1234 w+	1231 m+	δ(C-H2) τ C <sub>3</sub> , δ(C-H) C <sub>2</sub>
44	1287	1256 sh	1257 sh	-	1243 sh-	δ(C-H2) τ C <sub>3</sub> , δ(C-H) C <sub>2</sub>
45	1295	1270 sh	-	1268 m-	1250 s-	δ(C-H) Y7, δ(C-H) C <sub>2</sub>
46	1322	1295 s	1290 s	1298 m+	-	δ(C-H) Y8, δ(C-H2) Y8 τ C <sub>3</sub>
47	1346	-	-	-	1276 m+	δ(C-H) Y6 v <sub>3</sub> , δ(C-H2) ω C <sub>3</sub>
48	1361	1329 sh	-	-	1300 s-	δ(C-H2) ω C <sub>3</sub> , δ(C-H) C <sub>2</sub> , δ(C-H) Y6 v <sub>3</sub>
49	1380	-	-	-	1356 s-	δ(C-H) C <sub>2</sub> , δ(C-H2) ω C <sub>3</sub>
50	1416	1354 s	1342 sh	1348 s+	-	v(C=C) Y5 v <sub>14</sub> , δ(C-H2) C <sub>3</sub> τ
51	1447	1376 sh	1373 m	1378 w-	1377 w+	δ(C-H) C <sub>2</sub> , δ(C-O-H) C <sub>1</sub>
52	1482	1403 sh	1410 sh	-	-	δ(C-H2) σ C <sub>3</sub>
53	1505	1446 m	1449 m	1436/1456 m-/m+	1447 m+	v(C=C) Y4 v <sub>19b</sub> , δ(C-H2) σ C <sub>3</sub>
54	1513	1471 sh	1472 sh	-	-	δ(N-H3) ss
55	1559	1522 sh 1532 w	1521 sh 1533 s	-	-	

56	1635	-	-	-	$\delta(\text{N-H}_3)$ as
57	1654	1606 m	1607 s		$\nu(\text{C}=\text{C})$ Y2 $\nu_{8b}$ , $\delta(\text{N-H}_3)$ as
58	1664	-	-	1604 w-	$\delta(\text{N-H}_3)$ as
59	1676	1623 sh	1627 sh		$\nu(\text{C}=\text{C})$ Y1 $\nu_{8a}$
60	1807	1734 m	1735 s	-	$\nu(\text{C}=\text{O})$
61	3083	2870 m		-	$\nu(\text{C-H}_2)$ ss $\text{C}_3$ , $\nu(\text{C-H})$ $\text{C}_2$
62	3140	2941 s		2938 w+	$\nu(\text{C-H}_2)$ as $\text{C}_3$ , $\nu(\text{C-H})$ $\text{C}_2$
63	3151	2977 sh		2970 w-	$\nu(\text{C-H}_2)$ as $\text{C}_3$ , $\nu(\text{C-H})$ $\text{C}_2$
64	3199	3034 s		-	$\nu(\text{C-H})$ $\text{C}_2'$ , $\text{C}_5'$ , $\text{C}_6'$ op
65	3207	-		-	$\nu(\text{C-H})$ $\text{C}_2'$ , $\text{C}_5'$ , $\text{C}_6'$ op
66	3213	3081 s		-	$\nu(\text{C-H})$ $\text{C}_2'$ , $\text{C}_5'$ , $\text{C}_6'$ ip
67	3388	3214 w		-	$\nu(\text{N-H}_3)$ ss
68	3468	3245 sh		-	$\nu(\text{N-H}_3)$ as
69	3531	3275 sh		-	$\nu(\text{N-H}_3)$ as
70	3762	3464 sh		-	$\nu(\text{O-H})$ $\text{C}_1$
71	3791	3517 sh		-	$\nu(\text{O-H})$ $\text{C}_3'$
72	3846	3604 sh		-	$\nu(\text{O-H})$ $\text{C}_4'$

Intensity: s – strong (35 – 100%), m – medium (10 – 35%), w – weak (3 – 10%), vw – very weak (1 – 3%), sh – shoulder, – – undetected, +/- marks ROA and VCD band sign

$\gamma$  – out-of-plane deformation,  $\delta$  – in-plane deformation,  $\nu$  – stretching,  $\rho$  – rocking,  $\sigma$  – scissoring,  $\tau$  – twisting,  $\omega$  – wagging  
ip – in phase, op – out of phase, ss – symmetric, as – antisymmetric

Phe- phenyl ring

\* – B3PW91/6-311++G\*\*/cpcm(water) DOPAH\_11tc conformer

The overall agreement between the experimental and calculated spectral profiles is very good; whether we take into account the positions of the bands, their relative intensities, and, in the case of ROA and VCD also their signs. Despite that, in all spectra there is a common region where this agreement is slightly worse, particularly in the intensities. It is the 1000 – 1250  $\text{cm}^{-1}$  region, vibration modes 35 – 44 (according to the Table 6.6), where  $\delta(\text{C-OH})$  and  $\delta(\text{N-H}_3)$  vibrations are especially significant. However, this is not a surprise given the limitations of the implicit solvation model that was used. It is reasonable to assume that if we used the explicit solvation model (at least the directly bound water molecules), we would reach a better agreement.

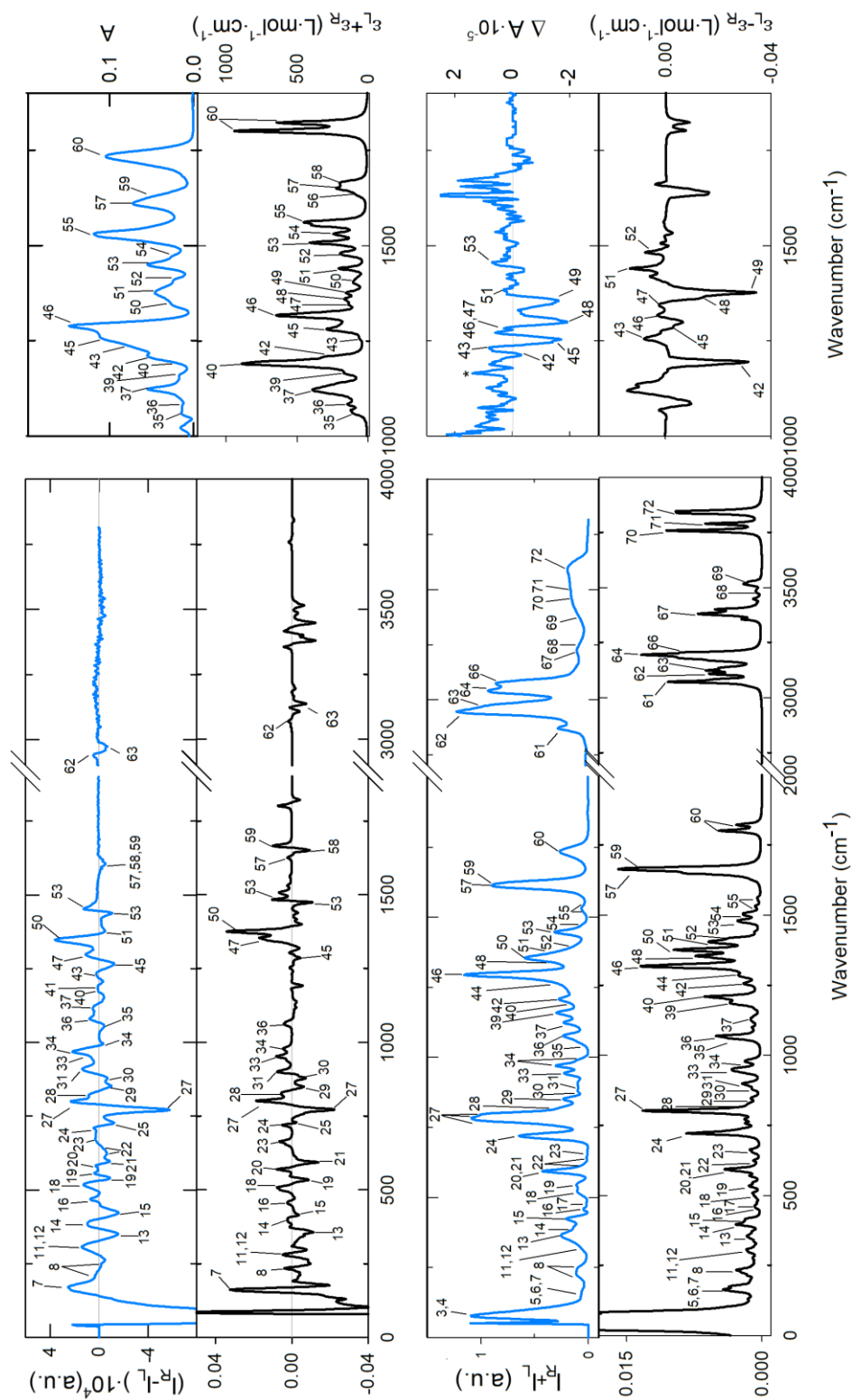


Figure 6.27: Comparison of experimental (blue lines) and computed (black lines) VOA spectra of L-DOPA with assigned vibrational modes. \* – artefact, \*\* – region with high noise signal due to the high absorbance of solvent (water) molecules



## 6.7 VOA of deuterated L-DOPA analogues

In this section we focus on the three deuterated derivatives of L-DOPA. We present the experimental Raman and ROA spectra of their 100 mg/ml solution in 1 M HCl and the simulated spectra of their cationic form. IR and VCD spectra of solid state samples are included in the Attachments as well as the liquid phase IR spectra. We were not able to obtain reliable VCD of liquid samples because only one enantiomer of each sample was available. In case of  $\alpha,\beta$ -D<sub>2</sub>-L-DOPA we focus also on the assignment of its absolute configuration. Simulated spectra were obtained as modified BA (see subsection 0) of 36 individual deuterated conformers. The spectra were simulated at B3PW91/6-311++G\*\*/cpcm(water) level of theory.

### 6.7.1 Triple deuterated 2',5',6'-D<sub>3</sub>-L-DOPA (VI)

Compared to other deuterated L-DOPA analogues, the isotopic exchange at phenyl hydrogen is rather distinct. The comparison of experimental and simulated spectra is shown in the Figure 6.28. The most pronounced changes when compared to the spectrum of non-deuterated L-DOPA (see Figure 6.11 or Figure 6.27) is the downshift of several bands corresponding to the phenyl vibrations in the fingerprint region and complete separation of the phenyl C–H stretching vibrations. All three modes associated with the stretches of phenyl hydrogens are shifted to 2200 – 2300 cm<sup>-1</sup>. These vibrations have very weak ROA signal which cannot be identified in the experimental spectrum. This is not too surprising, considering that the phenyl group is planar and the nearest chiral centre is C<sub>α</sub>. The recognizable ROA signal in C–H stretching region is formed by vibrations of C<sub>β</sub> and C<sub>α</sub> hydrogens and it is well reproduced in simulated spectra. Quite surprisingly, we are able to distinguish the O–H and even the N–H stretches in the experimental Raman spectrum. The overall correspondence of experimental and simulated spectra is very good and enables reliable band-to-band assignment of most of the spectral features, including the low-wavenumber (terahertz) region (down to ~75cm<sup>-1</sup>). In the Figure 6.28, the most specific bands are labelled in both experimental and simulated profiles.

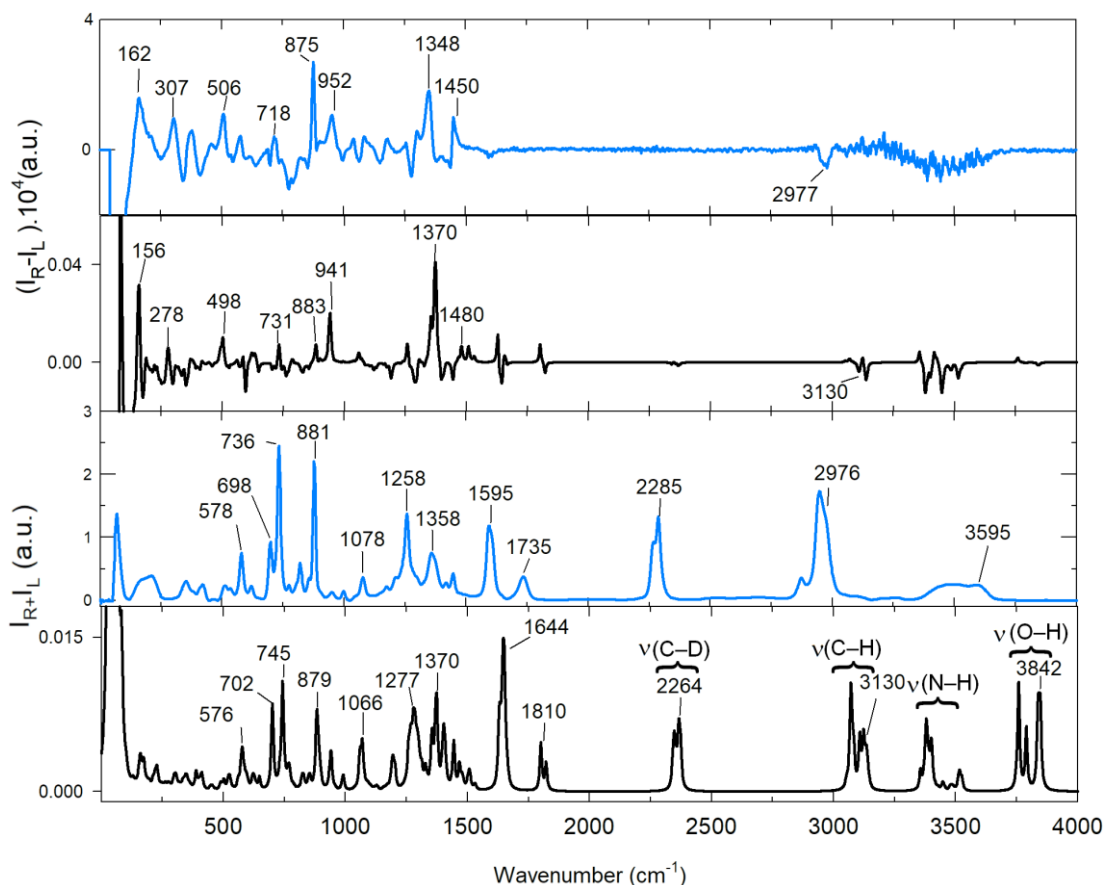


Figure 6.28: Comparison of experimental (blue lines) and computed (black lines) Raman and ROA spectra of 2',5',6'-D3-L-DOPA

### 6.7.2 Triple deuterated biologically active $\alpha,\beta,\beta$ -D3-L-DOPA (V)

If we focus only to the deuterations at the “hard” positions (carbon atoms), the molecule **V** represents a complement to the molecule **VI**, which was the object of interest in the previous subchapter 6.7.1. (Deuteration at the “soft” positions – amine, hydroxyl, and carboxyl groups was discussed in the section 6.4.) In this case, the chiral carbons  $C_\alpha$  and  $C_\beta$  on the alaninyl chain of L-DOPA are deuterated. The comparison of the experimental and simulated spectra is shown in Figure 6.29.

Similarly to the previous case, a clear separation of the C–H stretching modes is observable: phenyl CH vibrations with a negligible ROA signal remain unchanged and the rest of them ( $C_\alpha$ –H and  $C_\beta$ –H<sub>2</sub>) are shifted to 2100–2250 cm<sup>-1</sup> due to the isotopic exchange. Again, the experimental ROA signal of C–D stretches is quite well reproduced by the simulations. The changes in the rest of the spectrum are more subtle in comparison with the molecule **VI**, indicating that the vibrational modes of the phenyl group are more pronounced in both Raman scattering and ROA than the vibrational modes associated with  $C_\alpha$  and  $C_\beta$  atoms.

Also in this case, the overall agreement between the experimental and calculated spectra was at such good level that a reliable band-to-band assignment of most of the spectral features was enabled. In Figure 6.29, the most specific bands are labelled in the experimental as well as in the simulated spectra.

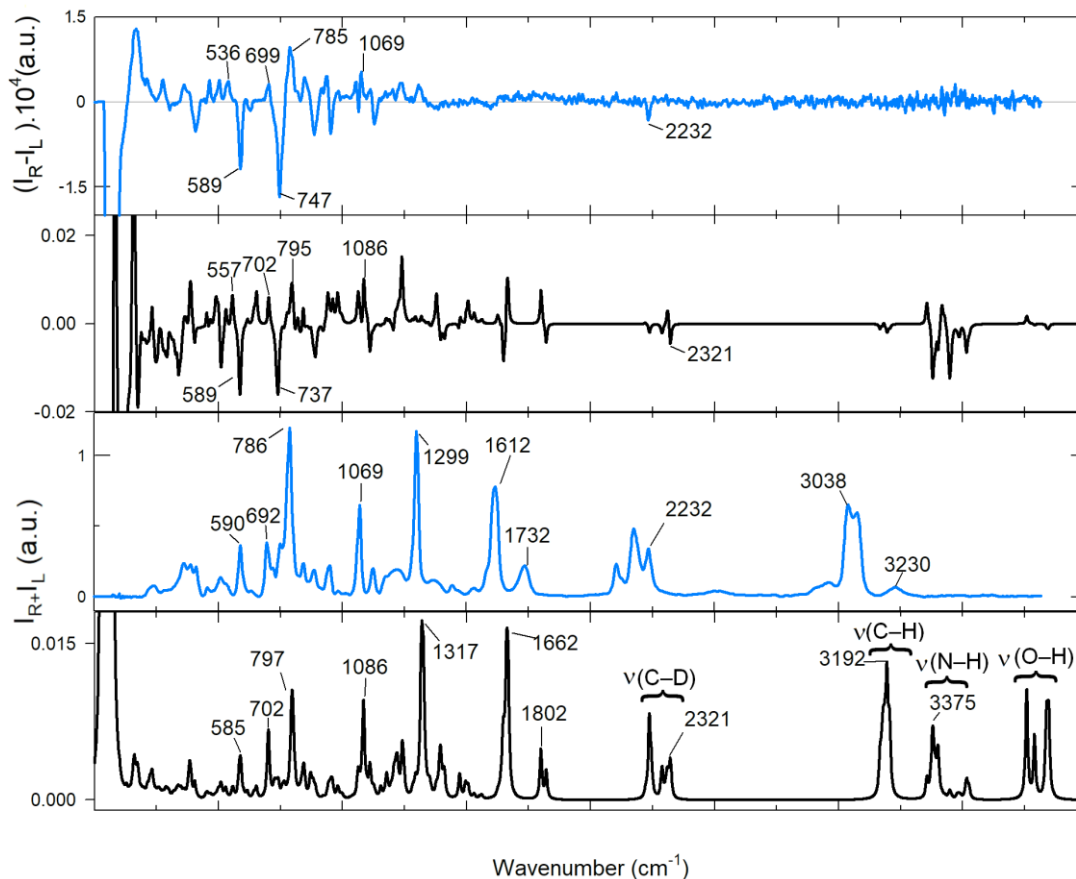


Figure 6.29: Comparison of experimental (blue lines) and computed (black lines) Raman and ROA spectra of  $\alpha,\beta,\beta$ -D<sub>3</sub>-L-DOPA

### 6.7.3 Double deuterated biologically active $\alpha,\beta$ -D2-L-DOPA (IV)

Partial deuteration at  $C_\beta$  creates an additional chiral centrum in the molecule of  $\alpha,\beta$ -D2-L-DOPA. While we know that non-deuterated L-DOPA occurs as a *S*-enantiomer, we do not know the chirality at the  $C_\beta$  of the  $\alpha,\beta$ -D2-L-DOPA sample. Therefore, the goal of this section is to determine the absolute configuration of  $\alpha,\beta$ -D2-L-DOPA based on the comparison of computed spectra for *S*- and *R*-enantiomers and at  $C_\beta$  their racemic mixture with the experimental spectra. The final experimental Raman and ROA spectra are shown in the Figure 6.30. IR spectra from 1M HCl solution as well as solid-phase IR and VCD spectra can be found in the Attachments.

In the Figure 6.31 we can see calculated VOA spectra of (*S*- $\alpha$ ,*S*- $\beta$ )-D2-L-DOPA, (*S*- $\alpha$ ,*R*- $\beta$ )-D2-L-DOPA and their racemic mixture. Figure 6.32 and Figure 6.33 show enlarged regions of ROA and Raman spectra, where the differences between both diastereomeric forms are most prominent. IR spectra appear insensitive to chirality at  $C_\beta$ . VCD seems to be more sensitive at least in the region of  $\delta(\text{CH}_2)$  wagging and twisting vibrations, and  $\delta(\text{CH})$  bending. However, the changes are so fine that a highly resolved experimental VCD would be needed to distinguish between *S*- and *R*- chirality at  $C_\beta$ . Unfortunately, the problem was getting a VCD spectrum of any quality, let alone high. Raman spectra of both diastereomers differ in both fingerprint and C–H/C–D stretching region. Nevertheless, these changes are limited to differences in intensity of several bands (see Figure 6.32 and Figure 6.33) which are practically impossible to trace in the experimental spectrum.

It is clear from what has been stated above that ROA is the only technique that is able to distinguish between different chirality on  $C_\beta$ . The main differences can be found in three narrow spectral regions: (i) 900 – 1050  $\text{cm}^{-1}$ , where we observe a -++ pattern in the experimental ROA spectrum. This pattern corresponds exclusively to the *S*-enantiomer at  $C_\beta$ . (The *R*-enantiomer shows a ++- pattern and the racemate has a +++ pattern.) (ii) 2100 – 2300  $\text{cm}^{-1}$  (C–D stretching vibrations), where we observe a -+ pattern in the experiment. This is also most credibly expressed in the calculated spectrum of the *S*-enantiomer. (While both the *R*-enantiomer and the racemate show a +- pattern.) And finally, (iii): 2900 – 3050  $\text{cm}^{-1}$  (C–H stretching region), where a +-- emerges in the experimental spectrum. The positive sign band corresponds to the symmetric C–H<sub>2</sub> stretching vibrations, while both negative bands refer to the coupled

C–H and antisymmetric C–H<sub>2</sub> stretches. Also in this case the calculated spectrum of *S*-enantiomer agrees best with the experiment. (The *R*-enantiomer shows a --- pattern and the racemate a +--- pattern.) The decisive factor in this case is the agreement of the sign of the symmetric C–H<sub>2</sub> stretching vibrations.

Thus, all three regions yield the same result. Namely, that the absolute configuration of sample **IV**, i.e.,  $\alpha,\beta$ -D<sub>2</sub>-L-DOPA, is (*S*- $\alpha,S$ - $\beta$ )-D<sub>2</sub>-L-DOPA. The possibility of racemic mixture with respect to the configuration on C <sub>$\beta$</sub>  is very unlikely. At most, it is a mixture of (*S*- $\alpha,S$ - $\beta$ )- and (*S*- $\alpha,R$ - $\beta$ )-enantiomers with a strongly predominant (*S*- $\alpha,S$ - $\beta$ )-enantiomer.

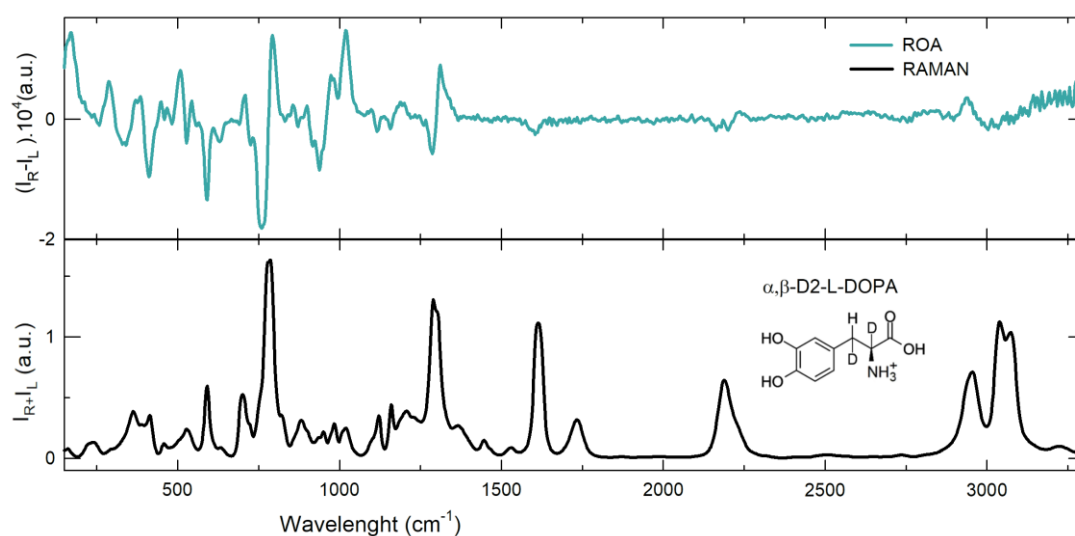


Figure 6.30: experimental VOA spectra of  $\alpha,\beta$ -D<sub>2</sub>-L-DOPA

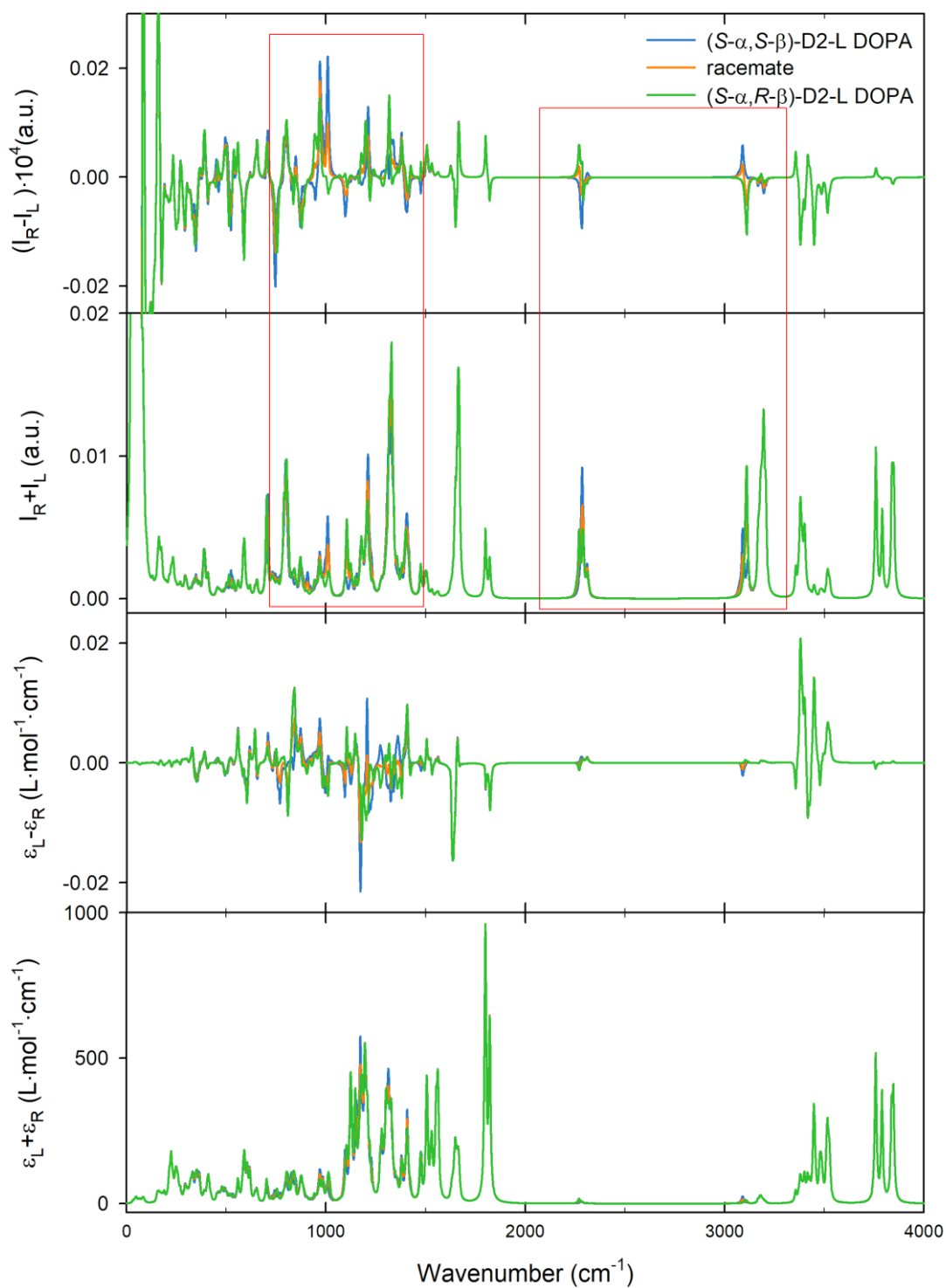


Figure 6.31: Theoretical VOA spectra of  $\alpha,\beta$ -D2-L-DOPA in (S- $\alpha$ ,S- $\beta$ ) and (S- $\alpha$ ,R- $\beta$ ) configurations and their racemic mixture.

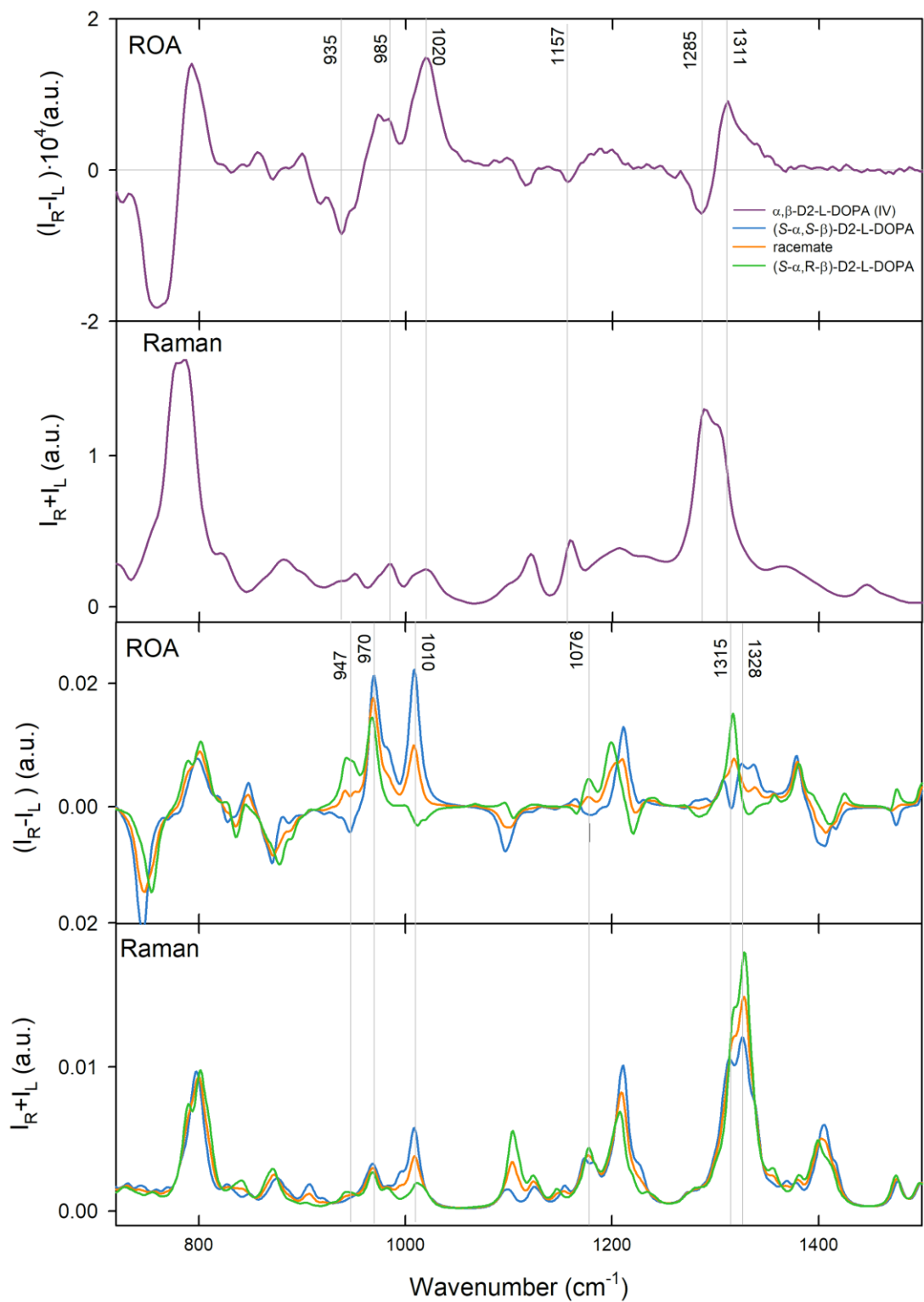


Figure 6.32: Comparison of computed and experimental ROA and Raman spectra of  $\alpha,\beta$ -D2-L-DOPA in the fingerprint spectral region.

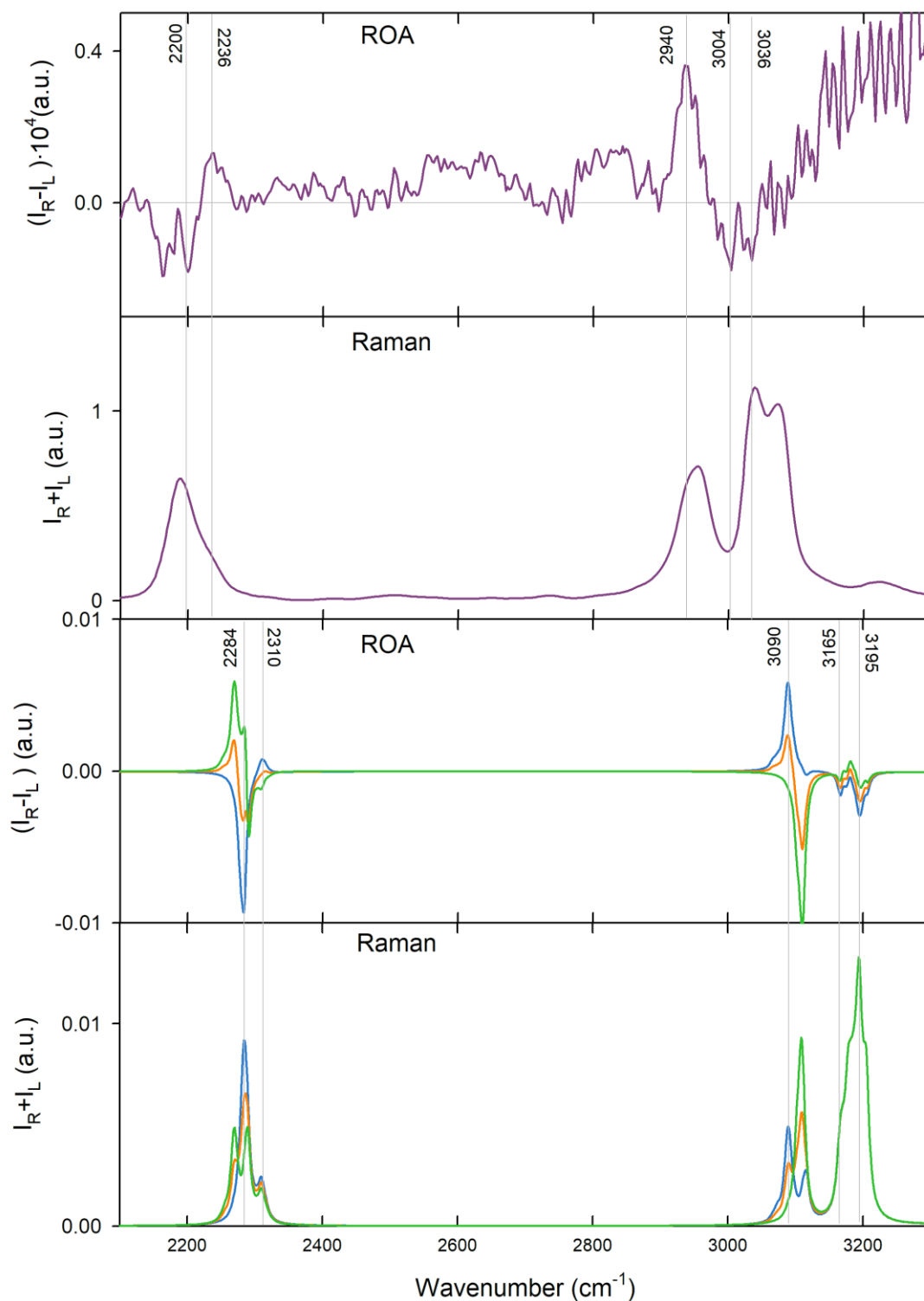


Figure 6.33: Comparison of computed and experimental ROA and Raman spectra of  $\alpha,\beta$ -D<sub>2</sub>-L-DOPA in the C-H and C-D spectral region.



## Conclusions

The main goal of this thesis was an overall characterization of L-DOPA and its deuterated analogues by the methods of vibrational spectroscopy. This intention was fulfilled in an exhaustive manner. Evaluation of individual goals is summarized in following paragraphs:

1. We elaborated a thorough review of Parkinson's disease treatment mechanism by L-DOPA with an inclusion of the studies concerning the employment of L-DOPA's deuterated derivatives.

Review of previous research on L-DOPA's vibrational analysis has revealed that such elaborate conformational analysis combined with vibrational assignment, as presented in this theses, has not been done before.

2. The author (me) has learned to operate several vibrational spectrometers located at the Institute of Physics of Charles University, including Raman micro-spectrometer Alpha 300 RSA, Raman spectrometer SPEX, and VCD spectrometer ChiralIR-2X<sup>TM</sup>. I gained valuable experience in preparing of the samples for spectroscopic measurements, learned to set the appropriate measurement parameters and mastered the post-processing of raw experimental data. I also learned the basic skills necessary for quantum-chemical simulations, including searching of the conformational space, averaging the spectra based on thermodynamics potential values, and performing vibrational analysis.
3. We successfully obtained the solid-phase Raman, IR, and even VCD spectra of both enantiomers of DOPA and also of its deuterated analogues. Comparing the spectra obtained from the liquid phase, we found that there is a high degree of similarity which suggests that L-DOPA samples in solid phase do not tend to form any supramolecular structures. Also the spectra of the same compound from different manufacturer showed a high degree of similarity.
4. We have found that the liquid phase Raman, ROA, IR, and VCD spectra of DOPA samples are best obtained when DOPA is in the form of a cation, i.e. at  $\text{pH} < 1$ , where sample concentrations of up to 100 mg/ml can be easily achieved. In the case of Raman scattering, we managed to obtain several spectra of neutral (zwitterionic) form of L-DOPA after a long effort. However, the differences in the

spectra between the cationic and zwitterionic forms were not very strong. Measurements in other solvents (DMSO, TFE, acetonitrile, and methanol) or at basic pH have not been proven appropriate.

5. Thanks to measurements on a state-of-art ROA spectrometer, we were able to obtain a high quality ROA and Raman spectra of L-DOPA and its deuterated analogues in the entire range of fundamental molecular vibrations (75 – 4000  $\text{cm}^{-1}$ ). We also obtained IR and VCD spectra but the measurement of the latter has been proven to be very difficult because the DOPA samples show a relatively low absorbance ( $\sim 0.2$  at a concentration of 100 mg/ml and use of 15  $\mu\text{m}$  spacer). Measurement of a reliable VCD signal therefore required a use of both enantiomers.

Nevertheless, we were able to describe in detail the spectral changes associated with deuteration at various carbon atoms as well as with the deuteration at easily exchangeable positions (amine, hydroxyl, and carboxyl groups).

6. We performed a detailed scan of the conformational space of cationic form of L-DOPA molecule, found its most probable conformers, and determined their relative ratios. However, these results have only a limited informative value, as the simulations were performed merely with an implicit solvent model, therefore, did not quite correctly described the intermolecular hydrogen bonds. Therefore we adjusted the ratio of individual conformers based on the comparison of experimental and simulated spectra.
7. After we included the dynamic aspect in the simulations (i.e. the balance between the individual conformations in which the molecule is found), we obtained a very good agreement of the experimental and simulated spectra of cationic form of L-DOPA and its variously deuterated analogues. Based on this, it was possible to perform a detailed vibrational analysis and an assignment of the individual bands.
8. Finally, based on the comparison of calculated and measured ROA spectra, we were able to determine the absolute configuration of sample **IV** ( $\alpha,\beta\text{-D}_2\text{-L-DOPA}$ ) which has an extra chiral centre at  $\text{C}_\beta$  due to the deuteration. We have found that its configuration is (*S*-  $\alpha,S\text{-}\beta$ ).

The latter result may also have practical application in the clinical research and in determination of the activity of new drugs for Parkinson's disease based on deuterated L-DOPA analogues. In previously published studies, there is no mention of creation

of a new chiral centre at C<sub>β</sub> of L-DOPA, but the chirality of this atom could have a significant effect on the stability and the biological efficiency of the produced dopamine. Using ROA we are able to relatively easily distinguish between the different epimers of DOPA samples.

In the future, we plan to focus primarily on further improving the calculations by including explicit solvation. We would also like to study other differently deuterated DOPA analogues.

## References

- ALKEN, R., et al. (2016). Less dyskinesia at motor-equivalent doses of triple-deuterated L-DOPA vs. L-DOPA after chronic administration in rats. *European Neuropsychopharmacology*, 26(26), pp.S253–S254.
- ANDERSSON, I., et al. (1975). Intestinal Decarboxylation of Orally Administered L-dopa. *Acta Medica Scandinavica*, 198(1–6), pp.415–420.
- ATKINS, P.W. and FRIEDMAN, R. (2011). *Molecular quantum mechanics*. Oxford: Oxford University Press.
- B&W Tek. (2019). *Theory of Raman Scattering* - B&W Tek. [online] Available at: <https://bwtek.com/raman-theory-of-raman-scattering/> [Accessed 4 Nov. 2019].
- BAAS, H., et al. (1997). Catechol-*O*-methyltransferase inhibition with tolcapone reduces the “wearing off” phenomenon and levodopa requirements in fluctuating parkinsonian patients. *Journal of Neurology, Neurosurgery & Psychiatry*, 63(4), pp.421–428.
- BAKER, J. (2017). Molecular Structure and Vibrational Spectra. Chapter 11 in: J. Leszczynski, et al. eds., *Handbook of Computational Chemistry*. [online] Springer, Cham, pp.423-496.
- BAKER, J., et al. (1996). The generation and use of delocalized internal coordinates in geometry optimization. *The Journal of Chemical Physics*, 105(1), pp.192–212.
- BARONE, V. and COSSI, M. (1998). Quantum Calculation of Molecular Energies and Energy Gradients in Solution by a Conductor Solvent Model. *The Journal of Physical Chemistry A*, 102(11), pp.1995–2001.
- BARTH, A. (2007). Infrared spectroscopy of proteins. *Biochimica et Biophysica Acta*, 1767 (9), pages 1073-1101.
- BERTOLDI, M. (2014). Mammalian dopa decarboxylase: Structure, catalytic activity and inhibition. *Archives of Biochemistry and Biophysics*.
- BIOTOOLS [online]. Available at: <https://www.biotoools.us/products.html#ir-2x>. Accessed 14 Apr. 2020.
- CHEMAXON (2019). *Chemicalize - Instant Cheminformatics Solutions*. [online] chemicalize.com. Available at: <https://chemicalize.com/app/calculation/levodopa> [Accessed 10 Dec. 2019].

- CHRISP, P., et al. (1991). Selegiline. *Drugs & Aging*, 1(3), pp.228–248.
- CONNOLLY, B.S., LANG, A.E. (2014). Pharmacological Treatment of Parkinson Disease. *JAMA*, 311(16), p.1670.
- COSSI, M., et al. (2003). Energies, structures, and electronic properties of molecules in solution with the C-PCM solvation model. *Journal of Computational Chemistry*, 24(6), pp.669–681.
- DELEU, D., et al. (2002). Clinical Pharmacokinetic and Pharmacodynamic Properties of Drugs Used in the Treatment of Parkinson's Disease. *Clinical Pharmacokinetics*, 41(4), pp.261–309.
- DEMEUSE, M. T. ed, (2011). *Biaxial Stretching of Film: Principles And Applications*. Elsevier. p. 48.
- DEVLIN, P.J. (2019). *Vcd Spectroscopy For Organic Chemists*. S.L.: Crc Press.
- EDWIN, B. and HUBERT J. I. (2013). Vibrational spectral analysis of anti-neurodegenerative drug Levodopa: A DFT study. *Journal of Molecular Structure*, 1034, pp.119–127.
- EL-AZAZY, M. (2018). *Introductory Chapter: Infrared Spectroscopy - A Synopsis of the Fundamentals and Applications, Infrared Spectroscopy - Principles, Advances, and Applications*. DOI: 10.5772/intechopen.82210.
- ELROBY, K., et al. (2012). Toward the Understanding of the Metabolism of Levodopa I. DFT Investigation of the Equilibrium Geometries, Acid-Base Properties and Levodopa-Water Complexes. *International Journal of Molecular Sciences*, [online] 13(4), pp.4321–4339.
- EXLINE, D. (2013). *Comparison of Raman and FTIR Spectroscopy: Advantages and Limitations*.
- FACTOR, S.A., et al. (2001). Long-Term Comparative Experience with Tolcapone and Entacapone in Advanced Parkinson's Disease. *Clinical Neuropharmacology*, 24(5), pp.295–299.
- FAHN, S. et al. (2004). Levodopa and the Progression of Parkinson's Disease. *New England Journal of Medicine*, 351(24), pp.2498–2508.
- FILIK, J. and STONE, N. (2007). Drop coating deposition Raman spectroscopy of protein mixtures. *The Analyst*, 132(6), p.544.

- FOGARASI, G., et al. (1992). The calculation of ab initio molecular geometries: efficient optimization by natural internal coordinates and empirical correction by offset forces. *Journal of the American Chemical Society*, 114(21), pp.8191–8201.
- FOX, S.H., et al. (2011). The Movement Disorder Society Evidence-Based Medicine Review Update: Treatments for the motor symptoms of Parkinson's disease. *Movement Disorders*, 26(S3), pp.S2–S41.
- FRISCH, M. J. et al. (2016). Gaussian 09, Revision A.02, Gaussian, Inc., Wallingford CT
- GERLACH, M., et al. (1996). Pharmacology of selegiline. *Neurology*, 47(Issue 6, Supplement 3), pp.137S-145S.
- GIARDINA, G., et al. (2011). Open conformation of human DOPA decarboxylase reveals the mechanism of PLP addition to Group II decarboxylases. *Proceedings of the National Academy of Sciences*, 108(51), pp.20514–20519.
- HAUSER, R.A. (2009). Levodopa: Past, Present, and Future. *European Neurology*, 62(1), pp.1–8.
- HORNYKIEWICZ, O. (2010). A brief history of levodopa. *Journal of Neurology*, 257(S2), 249–252.
- HUG, W. and HANGARTNER, G. (1999). A novel high-throughput Raman spectrometer for polarization difference measurements. *Journal of Raman Spectroscopy*, 30(9), pp.841–852.
- IVES, N.J., et al. (2004). Monoamine oxidase type B inhibitors in early Parkinson's disease: meta-analysis of 17 randomised trials involving 3525 patients. *BMJ*, 329(7466), p.593.
- KALIA, L. V., LANG, A. E. (2015). Parkinson's disease. *The Lancet*, 386(9996), 896–912.
- KIM, K. and JORDAN, K.D. (1994). Comparison of Density Functional and MP2 Calculations on the Water Monomer and Dimer. *The Journal of Physical Chemistry*, 98(40), pp.10089–10094.
- KLAMT, A. and SCHÜRMAN, G. (1993). COSMO: a new approach to dielectric screening in solvents with explicit expressions for the screening energy and its gradient. *J. Chem. Soc., Perkin Trans. 2*, (5), pp.799–805.
- KUIŽOVÁ, A. (2019). *Diplomová Práce*.

LARKIN, P. (2017). *Infrared and raman spectroscopy: principles and spectral interpretation*. 2nd ed. Elsevier. ISBN: 978-0-12-804162-8

LEE, E.-S.Y., et al. (2007). The Role of 3-*O*-Methyldopa in the Side Effects of l-dopa. *Neurochemical Research*, 33(3), pp.401–411.

LEWITT, P. A., FAHN, S. Levodopa therapy for Parkinson disease: a look backward and forward. *Neurology* 86, S3–S12 (2016)

MAGNASCO, V. (2013). *Elementary molecular quantum mechanics: mathematical methods and applications*. Amsterdam: Elsevier.

MALMLÖF, T., et al. (2008). Altered behavioural and neurochemical profile of l-DOPA following deuterium substitutions in the molecule. *Experimental Neurology*, 212(2), pp.538–542.

MALMLÖF, T., et al. (2010). Deuterium substitutions in the L-DOPA molecule improve its anti-akinetic potency without increasing dyskinesias. *Experimental Neurology*, 225(2), pp.408–415.

MALMLÖF, T., et al. (2014). Deuterium-substituted l-DOPA displays increased behavioral potency and dopamine output in an animal model of Parkinson's disease: comparison with the effects produced by l-DOPA and an MAO-B inhibitor. *Journal of Neural Transmission*, 122(2), pp.259–272.

MÄNNISTÖ, P.T., KAAKKOLA, S. (1989). New selective COMT inhibitors: useful adjuncts for Parkinson's disease? *Trends in Pharmacological Sciences*, 10(2), pp.54–56.

MARSDEN, C.D., PARKES, J.D. (1976). On-off" effects in patients with parkinson's disease on chronic levodopa therapy. *The Lancet*, 307(7954), pp.292–296.

MILLER, S.M. and KLINMAN, J.P. (1983). Magnitude of intrinsic isotope effects in the dopamine beta-monooxygenase reaction. *Biochemistry*, 22(13), pp.3091–3096

MONARD, G. AND RIVAIL, J.-L. (2017). Solvent Effects in Quantum Chemistry. Chapter 16 in: J. Leszczynski, et al. eds., *Handbook of Computational Chemistry*. [online] Springer, Cham, pp.727–739.

MOSTAD, A., et al. (1970). X-Ray Crystal Structure Determination of 3,4-Dihydroxyphenylalanine (L-DOPA). *Acta Chemica Scandinavica*, 24(5), pp.1864–1865.

- MOSTAD, A., et al. (1971). On the Structure of L-DOPA (2S-3-(3,4-Dihydroxyphenyl)alanine). *Acta Chemica Scandinavica*, 25(10), pp.3549–3560.
- NAFIE, L. A., et al. (2004). Dual Source Fourier Transform Polarization Modulation Spectroscopy: An Improved Method for the Measurement of Circular and Linear Dichroism. *Applied Spectroscopy*, 58(6), pp.647–654.
- NAFIE, L.A. (1995). Circular polarization spectroscopy of chiral molecules. *Journal of Molecular Structure*, 347, pp.83–100.
- NAFIE, L.A. (1996). Vibrational Optical Activity. *Applied Spectroscopy*, 50(5), pages14A-26A.
- NAFIE, L.A. (2011). *Vibrational optical activity: principles and applications*. Syracuse, N.Y.: Wiley.
- NUTT, J.G., FELLMAN, J.H. (1984). Pharmacokinetics of Levodopa. *Clinical Neuropharmacology*, 7(1), pp.35–50.
- PEERAN, M. (2005) Comparison of Raman and IR Spectroscopy. [online] Available at: <http://www.chemvista.org/ramanIR4.html>.
- PENG, C., et al. (1996). Using redundant internal coordinates to optimize equilibrium geometries and transition states. *Journal of Computational Chemistry*, 17(1), pp.49–56.
- PIELA, L. (2020). Chasing the Correlation Dragon: Density Functional Theory (DFT). In: *Ideas of Quantum Chemistry*.
- POEWE, W. et al. (2017). Parkinson disease. *Nat Rev Dis Primers* 3, 17013.
- PROFANTOVÁ, B., et al. (2013). Protonation Effect of Tyrosine in a Segment of the SRF Transcription Factor: A Combined Optical Spectroscopy, Molecular Dynamics, and Density Functional Theory Calculation Study. *The Journal of Physical Chemistry B*, 117(50), pp.16086–16095.
- PROSSER, V. et al. (1986) – *Experimentální metody biofyziky*, Praha: Academia. ISBN: 80-200-0059-3
- PULAY, P. and FOGARASI, G. (1992). Geometry optimization in redundant internal coordinates. *The Journal of Chemical Physics*, 96(4), pp.2856–2860.
- RAJPUT, A.H., et al. (2002). Clinical-Pathological study of levodopa complications. *Movement Disorders*, 17(2), pp.289–296.



- RAJPUT, A.H., et al. (2015). Normal substantia nigra patients treated with levodopa – Clinical, therapeutic and pathological observations. *Parkinsonism & Related Disorders*, 21(10), pp.1232–1237.
- RAJPUT, A.H., et al. (2004). Human brain dopamine metabolism in levodopa-induced dyskinesia and wearing-off. *Parkinsonism & Related Disorders*, 10(4), pp.221–226.
- RASCOL, O., et al. (2000). A Five-Year Study of the Incidence of Dyskinesia in Patients with Early Parkinson's Disease Who Were Treated with Ropinirole or Levodopa. *New England Journal of Medicine*, 342(20), pp.1484–1491.
- SCHLEGEL, H.B. (2011). Geometry optimization. *WIREs Computational Molecular Science*, 1(5), pp.790–809.
- SCHNEIDER, F., et al. (2018). Pharmacokinetics, metabolism and safety of deuterated L-DOPA (SD-1077)/carbidopa compared to L-DOPA/carbidopa following single oral dose administration in healthy subjects. *British Journal of Clinical Pharmacology*, 84(10), pp.2422–2432.
- SIDDIQUI, S., et al. (2010). Comparative conformational, structural and vibrational study on the molecular structure of tyrosine and L-DOPA using density functional theory. *J. Chem. Pharm. Res.*
- SKÁLA, L. (1995). *Kvantová teorie molekul*. 1st ed. Karolinum, p.232.
- SKYNER, R. E., et al. (2015). A review of methods for the calculation of solution free energies and the modelling of systems in solution. *Physical Chemistry Chemical Physics*, [online] 17(9), pp.6174–6191.
- SMITH, E. and DENT, G.(2004). *Modern Raman Spectroscopy: A Practical Approach*, HOBOKEN: J.Wiley & Sons, ISBN: 9780471496687
- SZABO A. AND N. OSTLUND, N.S. (1996). *Modern quantum chemistry : introduction to advanced electronic structure theory*. Mineola, N.Y.: Dover Publications.
- TOMASI, J., et al. (2005). Quantum Mechanical Continuum Solvation Models. *Chemical Reviews*, 105(8), pp.2999–3094.
- TOMASI, J., et al. (2007). Modern Theories of Continuum Models. Chapter 1 in: *Continuum Solvation Models in Chemical Physics*. B. Mennucci and R. Cammi, eds., John Wiley & Sons, Ltd, pp.1–123.

TOWNSEND, J., et al. (2019). Chapter 3 - Post-Hartree-Fock methods: configuration interaction, many-body perturbation theory, coupled-cluster theory. In *Developments in Physical & Theoretical Chemistry*, [online] 2, pp.63–117. ISBN 9780128136515

WALLER, D., SAMPSON, A.P. (2003). *Medical pharmacology & therapeutics*. Edinburgh: Elsevier, pp.1273–1278.

WATANABE, M., et al. (2003). Association between Catechol-*O*-Methyltransferase Gene Polymorphisms and Wearing-Off and Dyskinesia in Parkinson's Disease. *Neuropsychobiology*, 48(4), pp.190–193.

WILSON, E.B. (1934). The Normal Modes and Frequencies of Vibration of the Regular Plane Hexagon Model of the Benzene Molecule. *Physical Review*, 45(10), pp.706–714.

WISHART, D.S., et al. (2018). HMDB 4.0: the human metabolome database for 2018. *Nucleic Acids Research*, [online] 46(D1), pp.D608–D617.

YU, G.-S. and NAFIE L.A.(1994). Isolation of preresonance and out-of-phase dual circular polarization Raman optical activity. *Chemical Physics Letters*, **222**(4), pages.403–410.

YU, P.H. (1988). Three types of stereospecificity and the kinetic deuterium isotope effect in the oxidative deamination of dopamine as catalyzed by different amine oxidases. *Biochemistry and Cell Biology*, 66(8), pp.853–861.

YU, P.H., et al. (1986). Stereospecific deuterium substitution at the  $\alpha$ -carbon position of dopamine and its effect on oxidative deamination catalyzed by MAO-A and MAO-B from different tissues. *Biochemical Pharmacology*, 35(6), pp.1027–1036.

ZHANG, D., et al. (2003). Raman Detection of Proteomic Analytes. *Analytical Chemistry*, 75(21), pp.5703–5709.

## List of Figures

Figure 1.1: Mechanism of the dopamine synthesis. (PAH, phenylalanine hydroxylase; TH, tyrosine hydroxylase; DDC, DOPA decarboxylase) .....	5
Figure 1.2: Clinical symptoms and time course of Parkinson’s disease progression. Adopted from (Kalia and Lang, 2015).....	6
Figure 1.3: Metabolism of L-DOPA. Abbreviations include:3-O-MD, 3-O-methyldopa; ALDH, aldehyde dehydrogenase; COMT, catechol O-methyltransferase; DA, dopamine; DDC, DOPA decarboxylase; DOPAL,3,4-dihydroxyphenylacetaldehyde; DOPAC, 3,4-dihydroxyphenylacetic acid; HMPPA, 4-hydroxy-3-methoxyphenylpyruvic acid; HMPAL, 4-hydroxy-3-methoxyphenyl acetaldehyde; HVA, homovanillic acid; L-DOPA, L-3,4-dihydroxyphenylalanine; MAO, monoamine oxidase; TAT, tyrosine aminotransferase. Adopted from (Schneider et al. 2018) and edited. ....	8
Figure 1.4: Dopaminergic drug pathways in PD. Presynaptic targets include L-DOPA substitution combined with peripherally active inhibitors of aromatic amino acid decarboxylase (AADC) or catechol-O-methyltransferase (COMT). Monoamine oxidase type B (MAO-B) inhibitors enhance the synaptic availability of dopamine (both endogenous and exogenous), whereas dopamine agonists act postsynaptically. ....	10
Figure 1.5: Metabolism of $\alpha$ -D1-L-DOPA; DOPA decarboxylase (DDC) catalyses the decarboxylation to S- [D1]-L-DOPA, which is further oxidized by monoamine oxidase to $\alpha$ -D1-DOPAL proving that MAO removes the hydrogen in R-position. ...	11
Figure 1.6: Deuterated forms of L-DOPA studied in the 2008 Malmlof’s study.....	12
Figure 1.7: General $\alpha$ -amino acid (left) and its zwitterionic form (right). Hydrogen transfers from the acidic carboxylic group to the basic amine group. ....	13
Figure 1.8: Calculated dissociation constants and occurrences of different charge states of L-DOPA depending on the pH of the solvent. The figure is adopted and edited from (ChemAxon, 2019). (NC – net charge).....	15
Figure 1.9: Numbering of L-DOPA molecule (cationic form) adopted in this thesis. ....	17
Figure 3.1: Michelson interferometer: by changing the distance $d$ , only the wavelengths for which $d = k\lambda/2$ , where $k$ is an integer, are selected from continuous spectra. ....	26
Figure 3.2: Three possible transitions of molecular energy state after absorption of light: a) Rayleigh scattering, where the energy of emitted light is the same as of the incident light b) Stokes Raman scattering, where the energy of emitted light is lower than that of the incident light c) anti-Stokes Raman scattering where the energy of emitted light is higher than that of the incident light. $\nu_a$ and $\nu_e$ stand for the frequency of absorbed and emitted light, respectively. ....	27
Figure 3.3: Illustration of Raman spectrum. In the middle at $\nu_0$ (frequency of the incident radiation), is shown the Rayleigh line of elastic scattering, the left side of the spectrum is formed by anti-Stokes lines and the right side by Stokes lines. The value of frequency increases from right to left. Raman shift $\Delta\nu_i$ equals to energy difference between molecule’s initial and final state. ....	28
Figure 3.4: possible geometries of Raman spectrometer. a) forward-scattering geometry b) 90° geometry c) 180° geometry.....	30

Figure 3.5: Demonstration of left handed and right handed chiral molecule. Adapted from (Renstrom, 2018).....	31
Figure 3.6: Example of <i>S</i> - and <i>R</i> - enantiomers.....	31
Figure 3.7: Illustration of right- and left-circularly polarized light and (+)- and (-)-enantiomers of the same molecule. (Nafie, 1996).....	32
Figure 3.8: Process of absorption of right- (R) or left- (L) circularly polarized light. Adapted from (Nafie, 1995). .....	32
Figure 3.9: Different arrangements of ROA experiments. (Nafie, 1996) .....	34
Figure 4.1: Different approaches of modelling a solute in a solvent: a) the continuum approach – the molecule is closed in a cavity with the approximation of molecules charge distribution on the surface which interacts with the dielectric continuum representing the solvent; b)the fully solvated system – the solute is placed in a box filled with solvent molecules which are all modelled individually. (Monard and Rivail, 2017, edited).....	41
Figure 5.1: Spectrometer ChiralIR-2X <sup>TM</sup> used for the measurement of VCD and IR spectra. (VCD, vibrational circular dichroism; IR, infrared) .....	43
Figure 5.2: Beta Cell and a plastic cell holder from International Crystal Laboratories used for measurement on ChiralIR-2X .....	44
Figure 5.3: In WITec software Control FOUR, the user can select the desirable part of the image for scanning, that is marked by the red rectangle .....	49
Figure 5.4: WITec software Project FOUR used for spectral post-processing. The window with spectrum shows the selected spectral ranges (blue and green bands), the three windows on the top show the presence of particular characteristics in the scan and the window in the bottom right corner shows the pixels from which the final spectrum going to be composed. ....	49
Figure 5.5: Sample in a solid phase in Alpha300. PHR 1271 crystal selected for scanning.....	50
Figure 5.6: Demonstration of a DCDR sample. Typical “coffee-ring” of high sample concentration on the circumference is formed by dried microdroplet. Adopted from (Kuižová, 2019). .....	51
Figure 5.7: DCDR sample of 2',5',6'-D3-L-DOPA in HCl (left) and H <sub>2</sub> O (right). (DCDR, drop-coating deposition Raman).....	52
Figure 6.1: Comparison of L-DOPA Raman spectra in acidic and neutral pH. ....	55
Figure 6.2: Raman spectra of L-DOPA in tetrafluoroethylene (TFE) and dimethyl sulfoxide (DMSO) compared to the spectra of pure solvents. Parts of the spectra with strong residual signal of the solvents are left out. Asterisk (*) marks the artefacts caused by the background subtraction. ....	58
Figure 6.3: Comparison of L-DOPA ( <b>I</b> ) Raman spectra measured in different solvents. Asterisk (*) marks the artefacts caused by the background subtraction or other experimental artefacts. ....	58
Figure 6.4: Raman spectra of three non-deuterated DOPA samples as measured by different spectrometers: SPEX and Raman microscope Alpha 300. ....	61
Figure 6.5: Raman spectra of three differently deuterated DOPA samples as measured by different spectrometers: SPEX and Raman microscope Alpha 300.....	62
Figure 6.6: Comparison of the Raman spectra of 2',5',6'-D3-L-DOPA in acidic medium (top line) and pH neutral medium (bottom line). ....	63
Figure 6.7: Crystal-phase Raman and IR spectra of three non-deuterated samples ...	65
Figure 6.8: Liquid-phase Raman and IR spectra of three non-deuterated samples ....	65

Figure 6.9: Raman and IR spectra of all L-DOPA samples in 1M HCl and 1M DCl where the interchange of hydrogen atom for the deuterium atom is happening on the soft positions.....	67
Figure 6.10: Raman spectra of differently deuterated samples in 1M HCl. ....	68
Figure 6.11: VOA spectra of L-DOPA. Numbering of the vibrational modes corresponds to the Table 6.6. VCD spectra were acquired as a half of the difference between spectrum of L-DOPA and D-DOPA in order to lower the number of artefacts. ....	70
Figure 6.12: Solid phase VCD spectra of the two enantiomers of DOPA and their differential spectrum (top), overlapping IR spectra of both enantiomers (middle), and solid phase VCD spectra of DOPA enantiomers after artefact spectrum subtraction (bottom). * – artefact from KBr, ** – artefact of an unknown origin. ....	72
Figure 6.13: Liquid state VCD (top) and IR (bottom) spectra of the two enantiomers of DOPA in a 100 mg/ml solution in 1 M HCl. * – artefact from CaF <sub>2</sub> , ** – region of high water absorbance burdened with high noise signal.....	73
Figure 6.14: Definition of five torsion angles within L-DOPA structure characterising its conformation and the results of the 1D potential energy scans along the change of each of the angles with 10° step.....	75
Figure 6.15: 2D potential energy scans of L-DOPA molecule covering [α, β], [β, γ], and [δ, ε] pairs of dihedral angles together with the overview of the all located local energy minima. ....	76
Figure 6.16: Computed VOA spectra of all individual 36 conformers (black lines) and their Boltzmann-weighted average (orange line).....	81
Figure 6.17: Differently weighted averages of the computed spectra of all 36 conformers based on the division into 3 groups with different OH orientation. ....	82
Figure 6.18: Boltzmann-averaged spectra of the three groups of conformers with different orientation of OH groups. ....	83
Figure 6.19: Boltzmann weighted average VOA spectra of L-DOPA for two different conformations of the angle α.....	85
Figure 6.20: Computed (top) and experimental (bottom) ROA spectra. Determination of the occurrence of two different orientation of the angle α.....	86
Figure 6.21: Boltzmann weighted average VOA spectra of L-DOPA for three different conformations of the angle β.....	87
Figure 6.22: Computed (top) and experimental (bottom) ROA spectra. Determination of the occurrence of three different orientation of the angle β.....	88
Figure 6.23: Boltzmann weighted average VOA spectra of L-DOPA for two different conformations of the angle γ. ....	89
Figure 6.24: Boltzmann average VOA spectra of L-DOPA weighted based on the computed ratios of the conformer groups (black line) and the modified computed ratios (blue lines). ....	91
Figure 6.25: Computed (top) and experimental (bottom) ROA spectra which correspond better to the BA spectra weighted by the modified computed ratios (blue line). ....	92
Figure 6.26: Tyrosine (a) and benzene (b) vibrational modes. Pictures are adopted from (Profantová, 2013) and (Wilson, 1934), respectively. ....	93
Figure 6.27: Comparison of experimental (blue lines) and computed (black lines) VOA spectra of L-DOPA with assigned vibrational modes. * – artefact, ** – region with high noise signal due to the high absorbance of solvent (water) molecules ....	96
Figure 6.28: Comparison of experimental (blue lines) and computed (black lines) Raman and ROA spectra of 2',5',6'-D <sub>3</sub> -L-DOPA.....	98

Figure 6.29: Comparison of experimental (blue lines) and computed (black lines) Raman and ROA spectra of $\alpha,\beta,\beta$ -D3-L-DOPA.....	99
Figure 6.30: experimental VOA spectra of $\alpha,\beta$ -D2-L-DOPA.....	101
Figure 6.31: Theoretical VOA spectra of $\alpha,\beta$ -D2-L-DOPA in ( <i>S</i> - $\alpha$ , <i>S</i> - $\beta$ ) and ( <i>S</i> - $\alpha$ , <i>R</i> - $\beta$ ) configurations and their racemic mixture. ....	102
Figure 6.32: Comparison of computed and experimental ROA and Raman spectra of $\alpha,\beta$ -D2-L-DOPA in the fingerprint spectral region. ....	103
Figure 6.33: Comparison of computed and experimental ROA and Raman spectra of $\alpha,\beta$ -D2-L-DOPA in the C–H and C–D spectral region.....	104
Figure A.1: IR spectrum of sample <b>VI</b> in a 100 mg/ml solution in 1M HCl. ....	121
Figure A.2: IR spectrum of sample <b>V</b> in a 100 mg/ml solution in 1M HCl. ....	121
Figure A.3: IR spectrum of sample <b>IV</b> in a 100 mg/ml solution in 1M HCl. ....	121
Figure A.4: IR spectrum of sample <b>VI</b> in a solid state. ....	123
Figure A.5: IR spectrum of sample <b>V</b> in a solid state. ....	123
Figure A.6: IR spectrum of sample <b>VI</b> in a solid state. ....	123

## List of Tables

Table 1.1: Water solubility of different $\alpha$ -amino acids.....	14
Table 3.1: Comparison of Raman and infrared spectroscopy. Adopted from (Peeran, 2005) .....	35
Table 5.1: Available samples .....	42
Table 5.2: Parameters of the measurement of L-DOPA in different solvents .....	47
Table 5.3: Parameters of the measurement of L-DOPA in H <sub>2</sub> O and D <sub>2</sub> O .....	47
Table 5.4: Parameters of the measurement of all samples in HCl and DCISpectrometer SPEX; 532 nm; 400mW; 75-2300 cm <sup>-1</sup> .....	48
Table 5.5: Parameters of the scanned area for DCDR samples.....	52
Table 6.1: solubility of L-DOPA in various pH.....	54
Table 6.2: Testing of L-DOPA solubility in different solvents.....	57
Table 6.3: Empirical assignment of C–H and C–D vibrations.....	69
Table 6.4: Angle's values at the local energy minima of L-DOPA and their description. ....	74
Table 6.5: Most probable conformations of L-DOPA .....	78
Table 6.6: Vibrational assignment of L-DOPA spectra.....	94

## List of Abbreviations

<b>3-MT</b>	3-methoxytyramine
<b>3-OMD</b>	3- <i>O</i> -methyldopa
<b>AADC</b>	Amino acid decarboxylase
<b>AFM</b>	Atomic force microscope
<b>ALDH</b>	Aldehyde dehydrogenase
<b>BBB</b>	Blood-brain barrier
<b>CID</b>	Circular intensity difference
<b>COMT</b>	Catechol- <i>O</i> -methyltransferase
<b>COSMO</b>	Conductor-like screening model
<b>C-PCM</b>	Conductor-like polarizable continuum model
<b>DA</b>	Dopamine
<b>DCDR</b>	Drop-coating deposition Raman
<b>DCP</b>	Dual circular polarization
<b>DDC</b>	Dopa decarboxylase
<b>DFT</b>	Density functional theory
<b>DMSO</b>	Dimethyl sulfoxide
<b>DOPAC</b>	3,4-dihydroxyphenylacetic acid
<b>DOPAL</b>	3,4-dihydroxyphenylacetaldehyd
<b>HF</b>	Hartree-Fock theory
<b>HK</b>	Hohenberg-Kohn
<b>HVA</b>	Homovanillic acid
<b>ICL</b>	International Crystal Laboratories
<b>ICP</b>	Incident circular polarization
<b>IR</b>	Infrared
<b>KIE</b>	Kinetic isotope effect
<b>LCAO</b>	Linear combination of atomic orbitals
<b>MAO</b>	Monoamine oxidase
<b>PCM</b>	Polarizable continuum model
<b>PD</b>	Parkinson's disease
<b>PEM</b>	Photoelastic modulator
<b>PES</b>	Potential energy surface
<b>QM</b>	Quantum mechanical
<b>ROA</b>	Raman optical activity
<b>RS</b>	Raman spectroscopy
<b>SBD</b>	Solvation model based on density
<b>SCF</b>	Self-consistent field method
<b>SCP</b>	Scattered circular polarization
<b>SNOM</b>	Scanning near-field optical microscope
<b>TAT</b>	Tyrosine aminotransferase
<b>TFE</b>	Tetrafluoroethylene
<b>TH</b>	Tyrosine hydroxylase
<b>UHTS</b>	Ultra-high throughput spectrometer
<b>UV</b>	Ultraviolet
<b>VCD</b>	Vibrational circular dichroism
<b>VOA</b>	Vibrational optical activity
<b>VS</b>	Vibrational spectroscopy



## Attachments

### A.1. IR spectra of L-DOPA deuterated analogues in a liquid state

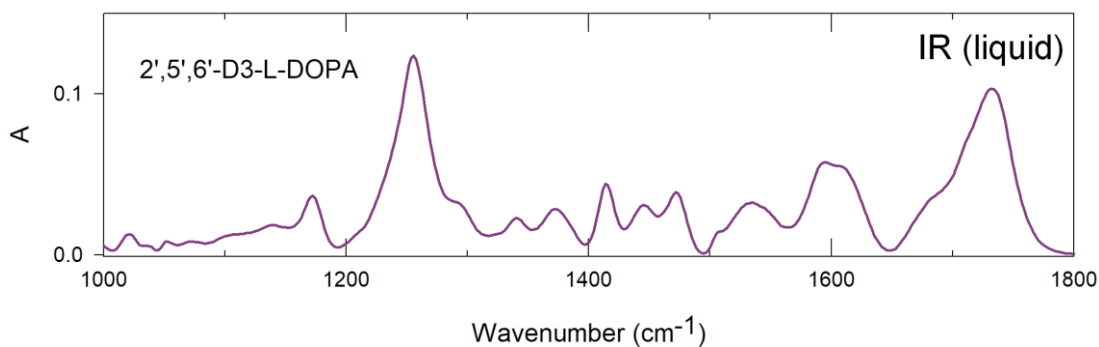


Figure A.1: IR spectrum of sample **VI** in a 100 mg/ml solution in 1M HCl.

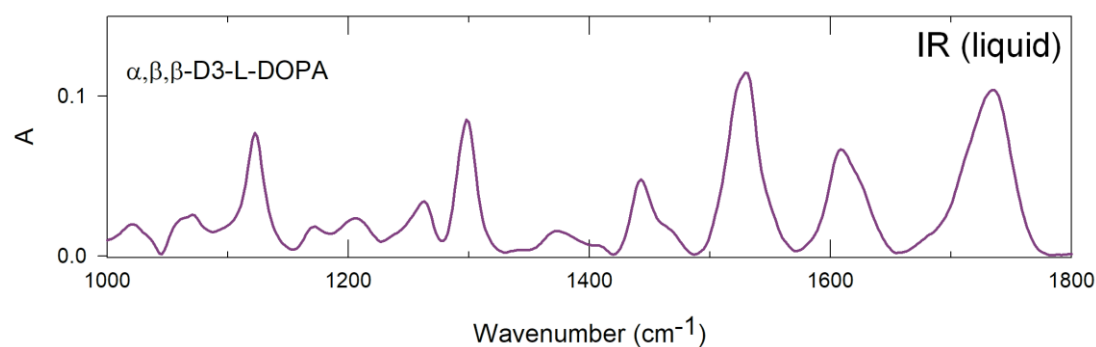


Figure A.2: IR spectrum of sample **V** in a 100 mg/ml solution in 1M HCl.

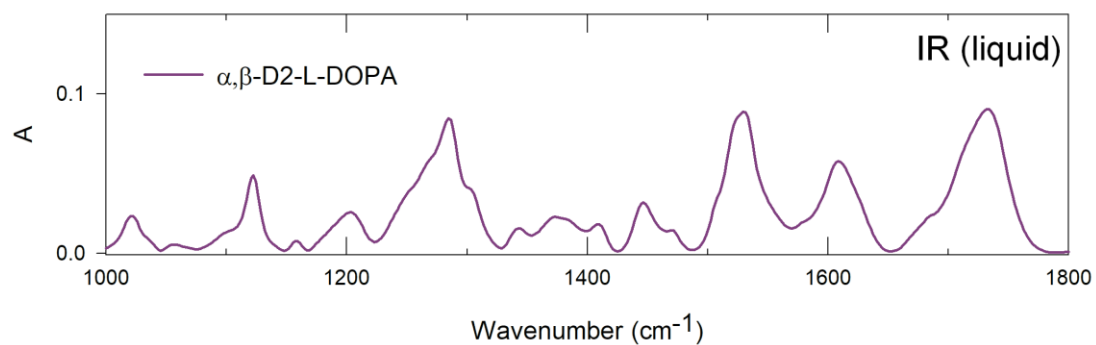


Figure A.3: IR spectrum of sample **IV** in a 100 mg/ml solution in 1M HCl.

## A.2. IR spectra of L-DOPA deuterated analogues in a solid state

In the figures presented below, \* marks the remaining artefact of KBr and \*\* an artefact of unknown region.

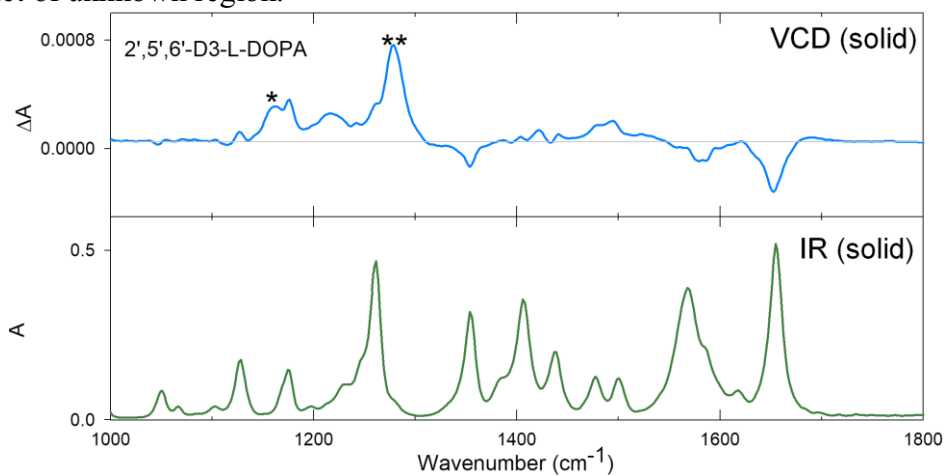


Figure A.4: IR spectrum of sample VI in a solid state.

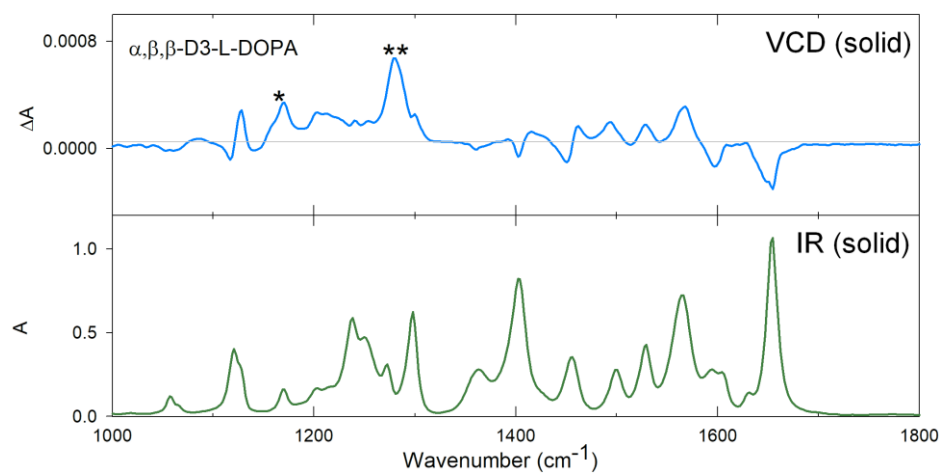


Figure A.5: IR spectrum of sample V in a solid state.

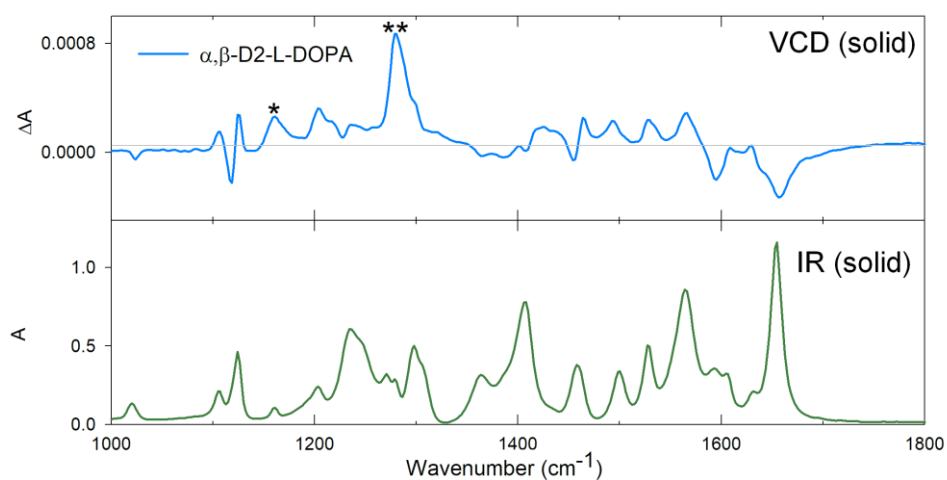


Figure A.6: IR spectrum of sample VI in a solid state.